Growth and Applications of Low Dimensional SnO_2

by

Binaya Kumar Sahu
Enrolment no: PHYS 02 2015 04 020

Indira Gandhi Centre for Atomic Research,
Kalpakkam, Tamil Nadu, India, 603102

A thesis

Submitted to

The Board of Studies in Physical Sciences

In partial fulfillment of requirements for the Degree of

DOCTOR OF PHILOSOPHY

of

HOMI BHABHA NATIONAL INSTITUTE

November 2020

Homi Bhabha National Institute

Recommendations of the Viva Voce Committee

As members of the Viva Voce Committee, we certify that we have read the dissertation prepared by **Binaya Kumar Sahu** entitled "Growth and applications of low dimensional SnO_2" and recommend that it may be accepted as fulfilling the thesis requirement for the award of Degree of Doctor of Philosophy.

Chairman: **Dr. M. Kamruddin**	Date: 01.04.2021
Guide/ Convener: **Dr. Arindam Das**	Date: 01.04.2021
External Examiner: **Dr. Karuna Kar Nanda**	Date: 01/04/2021
Member 1: **Dr. T.R. Ravindran**	Date: 1/04/2021
Member 2: **Dr. Arup Dasgupta**	Date: 01.04.2021

Final approval and acceptance of this thesis is contingent upon the candidate's submission of the final copies of the thesis to HBNI.

I hereby certify that I have read this thesis prepared under my direction and recommend that it may be accepted as fulfilling the thesis requirement.

Date: 01/04/2021

Place: Kalpakkam

Dr. Arindam Das

(Guide)

Homi Bhabha National Institute

Recommendations of the Viva Voce Committee

As members of the Viva Voce Committee, we certify that we have read the dissertation prepared by **Binaya Kumar Sahu** entitled "Growth and applications of low dimensional SnO_2" and recommend that it may be accepted as fulfilling the thesis requirement for the award of Degree of Doctor of Philosophy.

Chairman: **Dr. M. Kamruddin**	Date: 01.04.2021
Guide/ Convener: **Dr. Arindam Das**	Date: 01. 04. 2021
Arindam Das	
External Examiner: **Dr. Karuna Kar Nanda**	Date: 01/04/2021
KK Nanda	
Member 1: **Dr. T.R. Ravindran**	Date: 1/04/2021
TR Ravindran	
Member 2: **Dr. Arup Dasgupta**	Date: 01. 04. 2021

Final approval and acceptance of this thesis is contingent upon the candidate's submission of the final copies of the thesis to HBNI.

I hereby certify that I have read this thesis prepared under my direction and recommend that it may be accepted as fulfilling the thesis requirement.

Date: 01/04/2021

Place: Kalpakkam

Arindam Das

Dr. Arindam Das

(Guide)

Statement by Author

This dissertation has been submitted in the partial fulfilment of requirements for an advanced degree at Homi Bhabha National Institute (HBNI) and is deposited in the Library to be made available for borrowers under rules of the HBNI.

Brief quotation from this dissertation are allowable without special permission, provided that accurate acknowledgement of source is made. Requests for permission for extended quotation from or reproduction of this manuscript in whole or in part may be granted by the Competent Authority of HBNI when in his or her judgement the proposed use of the material is in the interests of the scholarship. In all other instances, however, permission must be obtained from the author.

Binaya Kumar Sahu

Binaya Kumar Sahu

Declaration

I, hereby declare that the investigation presented in the thesis has been carried out by me. The work is original and has not been submitted earlier as a whole or in part for a degree/diploma at any other Institute/University.

Binaya Kumar Sahu

Binaya Kumar Sahu

List of Publications

Journals

Published

1. Interface of GO with SnO_2 quantum dots as efficient visible-light photocatalyst.

   Binaya Kumar Sahu, Rabindranath Juine, Madhusmita Sahoo, Ravi Kumar, A. Das., Chemosphere, **276**, 130140-130149, 2021

2. Unraveling defect chemistry mechanism in SnO_2 QD for selective detection of NH_3 using blue emission luminescence sensor at room
   Binaya Kumar Sahu, Gurpreet Kaur, A. Das., ACS Appl. Mater. Interface. 43, 49227-49236, (2020)

3. Optimized Au NRs for efficient SERS and SERRS performances with molecular and longitudinal surface plasmon resonance
   Binaya Kumar Sahu, A. Dwivedi, K.K. Pal, R. Pandian, S. Dhara, A. Das, Appl. Surf. Sci.**537**,147615-147626, (2020).

4. Graphene oxide surface chemistry regulated growth of SnO_2 nanoparticles for electrochemical application
   Binaya Kumar Sahu, A. Das, J. Alloys Compd., **834**,154901-154909, (2020)

5. Sub-wavelength waveguide properties of 1D and surface-functionalized SnO_2 nanostructures of various morphologies,
   V. Bonu, **Binaya Kumar Sahu**, A. Das, S. Amirthapandian, S. Dhara, H.C. Barshilia, Beilstein J Nanotech., **10** ,379-388, (2019).

6. The role of in-plane oxygen vacancy defects in SnO_2 nanoparticles for CH_4 sensing
   Binaya Kumar Sahu, A. Das, A.K. Prasad, G. Mangamma, J Nanosci. Nanotech.,**19** ,7764-7770, (2019).

7. Significance of oxygen defects in SnO_2 quantum dots as hybrid electrochemical capacitors
   Binaya Kumar Sahu, A. Das, J. Phys. Chem. Solids, **127**, 293-297, (2019).

8. Significance of in-plane oxygen vacancy rich non-stoichiometric layer towards unusual high dielectric constant in nano-structured SnO_2
   Binaya Kumar Sahu, A. Das, Physica E **103**, 60-65, (2018).

Communicated/Under Preparation

1. Lifting up the mutual exclusion principle in SnO_2 nanoparticle for invoking forbidden vibrational mode by plasmon and high-pressure Raman studies,
   Binaya Kumar Sahu, A. Das.
2. Rapid dye degradation using SnO_2 QDs
   Binaya Kumar Sahu, A. Das

3. Dye degradation using SnO_2 NPs: correlation with defect, **Binaya Kumar Sahu,** A. Das

Conference Proceeding

1. Room temperature ammonia sensor using SnO_2 quantum dots: An approach toward the optical eye:

   Binaya Kumar Sahu, R. Juine, A. Das, AIP Conference Proceedings, AIP Publishing, 2019, pp. 030135.
2. Defect induced photoluminescence in SnO_2 nanostructures: Evaluation and Utilization for optical sensing and waveguide application

   Binaya Kumar Sahu, R. Juine, A. Das,Bulletin of the American Physical Society (2020)

Conference

1. Vibrational spectroscopy and dielectric study of finite sized SnO_2

   Binaya Kumar Sahu, V Bonu, A. Das, ICOPVS-2016, Lucknow, India. (Poster presentation).
2. Effective Control of Non stoichiometric Layer and Defects for High dielectrics and Sensor study.

   Binaya Kumar Sahu, A. Das, ICC-2017, Bikaner, India. (Poster presentation)
3. Controllable synthesis of SnO_2 nanostructures for optical and electrical applications

   Binaya Kumar Sahu, A. Das, RSM-2018, IGCAR, Kalpakkam,India. (Poster presentation)
4. Room temperature Ammonia Sensor using SnO_2 Quantum Dots:an Approach towards Optical Eye.

   Binaya Kumar Sahu, R. Juine, A. Das, 63rd DAE Solid State Physics Symposium,2018 Hissar, Haryana, India. (Oral presentation)
5. GO-SnO_2 Nano-composite for electrochemical and optical application.

   Binaya Kumar Sahu, A Das, ICONN-2019, Chennai, India. (Poster presentation)
6. Synthesis of 1-D SnO_2 micro and nano structures for optical application.

   Binaya Kumar Sahu, A. Das, LMIN-2019, IGCAR, Kalpakkam,India. (Poster presentation)
7. TERS study in understanding the observation of forbidden vibrational mode in SnO_2 nanoparticle

Binaya Kumar Sahu, A. Das, Santanu Parida, Sandip Dhara, A. Das, ICOPVS-2020, JNCASR, Bangalore, India. (Poster presentation)

8. Plasmonic of Ag network for trace detection and manipulation of metal oxide IR modes

   Binaya Kumar Sahu, Reshma T.S., A. Das., IEEE-ICEE-2020, IIT Delhi, India. (Oral Presentation)

Others: Not included in thesis

1. Recyclable ZnS QDs as an efficient photocatalyst for dye degradation under the UV and visible light.

   R.N. Juine, **Binaya Kumar Sahu**, A. Das, New Journal of Chemistry, 243 (2020) 118782.
2. Correlation with surface defects and maiden observation of disorder activated phonon in cubic ZnS QDs.

   R.N. Juine, **Binaya Kumar Sahu**, A. Das, Spectrochimica Acta Part A, 243 (2020) 118782
3. Invoking Obscured Surface Optical, Acoustic, and Anharmonic Phonon Modes and Their Modulation by Synthesis Conditions and Arrangement of the Surface in 0-D ZnS

   R.N. Juine, **Binaya Kumar Sahu**, S. Amirthapandian, A. Das, , J. Phys. Chem. C, 124 (2020) 17227-17236.
4. Synthesis and structural characterization of $Y_2Ti_2O_7$ using microwave hydrothermal route

   T. Gadipelly, A. Dasgupta, C. Ghosh, V. Krupa, D. Sornadurai, **Binaya Kumar Sahu**, S. Dhara, J. Alloys Compd, 814, 152273-152281, (2020).
5. Enhanced electrochemical performance of lithium-sulfur battery by negating polysulphide shuttling and interfacial resistance through aluminum nanolayer deposition on a polypropylene separator

   M.M.U. Din, **Binaya Kumar Sahu**, A. Das, R. Murugan, Ionics, 25,1645-1657, (2019)

Binaya Kumar Sahu

Dedicated to ~

My brain is only a receiver, in the Universe there is a core from which we obtain knowledge, strength and inspiration.

~ Nikola Tesla

……and for me that core is my Bou and Bapa.

Binaya Kumar Sahu

~ Binaya Kumar Sahu

Acknowledgements

First and foremost, I would like to express my heartful gratitude to my Ph.D. adviser Dr. Arindam Das, for his constant encouragement, caring, and insightful guidance all the way leading to the completion of my Ph.D. His deep intelligence, enthusiasm, experience, and friendliness have made my research life smooth and enjoyable. Especially, his skill of solving various critical problems in a simpler way persuade me a lot during my research.

I would like to express my sincere gratitude to Dr. Sandip Kumar Dhara for his support and motivation during my Ph.D. I am deeply thanking him for sharing his scientific and technical knowledge through discussion and insightful suggestions.

My sincere thanks to my doctoral committee, Dr. M. Kamruddin, Dr. T. R. Ravindran, and Dr. Arup Dasgupta, for their careful evaluation and insightful suggestions throughout these years.

I would like to express my gratitude to Dr. A. K. Bhaduri and Dr. S.A.V. Satya Murty, present and former Director, IGCAR, for permitting me to pursue Ph. D. at IGCAR. I am highly thankful to Dr. Shaju K. Albert and Dr. G. Amarendra, present and former Group Director, MSG, for providing a pleasant atmosphere for my smooth research. I thank Dr. Vidya Sundararajan, Dr. T. S. Lakshmi Narasimhan and Dr. M. Saibaba, present and former Dean SA, for the wonderful hospitality during my stay at JRF Enclave. I would like to thank Dr. R. Rajaraman, Dr. N. V. Chandra Shekar, and Dr. B. V. R. Tata, present and former Dean physical sciences, HBNI, IGCAR, for their support and being friendly during all the procedure throughout the tenure.

I would like to acknowledge the Dept. of Atomic Energy, Govt. of India for research fellowship. I am also thankful to all reviewers and the examiner for their time and careful evaluation.

I also take this opportunity to thanks Mr. Magudpati, Dr. S. Amrithapandian, Dr. Arun Kumar Prasad, Dr. Ramanathswamy Pandian, Dr. S. R. Polaki, Dr. Madhusmita Sahoo, Dr. Gurpreet Kaur for their help during various experiments. I am further thankful to Dr. S. N Jha, RRCAT, Indore, and Dr. Mukul Gupta, UGC, DAE, Indore, for providing synchrotron facility.

I deeply express my thanks to Dr. G. Mangama, Dr. Tom Mathews, and all NCSS and TFCS, IGCAR members for their valuable comments on various occasions. I felt lucky to have seniors like

Dr. Bonu Venkata Ramana, Dr. Kishore Madapu, Dr. Avinash Patsha, Dr. Sivadashan, Dr. Subroto Ghosh, Dr. Santanu Parida, Dr. Raktima Basu. I appreciate their constant endurance in teaching me many experiments and theories and always treating me as a younger brother. I also thank my juniors Reshma P.R, Sourav, Abinash, Reshma T.S., and Hrudya, for their help during various experiments and providing a cordial atmosphere in the lab.

I would like to thank Ravindra Nath Juine, HPU, BARC, Mir Meheraj Uddin, Pondicherry University, Malaya Ranjan Biswal, JNCSAR for keeping my research spirit up. I (Ironman) would like to introduce the Avengers team consists of Padmalochan(Nick Fury), Nilakantha(Thor), Dillip(Captain America), Alok(Hulk), Gopinath(Hawkeye), Sitakanta (Star Lords), and Prasanta (Spiderman). Our crazy expedition to different parts of India was always acting as fuel throughout the year. I also extend my gratitude to my inmates Bijaya, Anil, Vikash, Darpan, Pavan, Sourav Suvendu, Arpita, Alaka, Shradha, Akshaya, Ijee, Pragnya, Rajitha, Jagatha, Bala, and Dillipan. I am thanking my roommate Hari Mohan Jha for his mid-night loud song, which generally kept me up at night to finish my thesis. My special thanks to Akka, Anna from CC canteen, Nair Ji, and Gokul Ji for providing life-saving food and beverages.

On this occasion, I will express my heartiest gratitude and respect to my school teachers Mr. Dhruva Charana Das and Mr. Dinabandhu Barik, for introducing me to the mysterious universe of science.

This acknowledgment will be incomplete without revealing the real source of energy for me, my parents, sisters, brother and brothers-in-laws. They are always with me in every rise and fall to appreciate and encourage me.

Binaya Kumar Sahu

Binaya Kumar Sahu

Table of contents

List of Figures

List of tables

Chapter 7

Summary and scope for future work

7.1. Summary

The present thesis focuses broadly on two aspects of SnO_2 NSs.

1. Synthesis and understanding the defects in lower dimensions of SnO_2 NSs, such as NPs (0-D) and NWs and μB (1-D). Its beneficial properties are clubbed together with GO in the form of GO-SnO_2 nanocomposites.
2. Apart from detailed characterization and elucidation of prevalent defects in NSs, utilizations of these NSs for various applications like PL based selective ammonia sensing, electrochemical capacitor for energy harvest, photocatalysis for environmental remediation, resistive sensor at low temperature, waveguide utility of 1-D NSs, and unusually high dielectric value are explored.

A brief chapter wise summary of the thesis and the future scope of the present work is presented below:

A detailed description of the structural, optical, and vibrational properties of rutile SnO_2 is given in Chapter-1. Consequences arising from the formation of lower dimensions and composite materials are discussed with the literature review. Besides, the importance of defects presents in SnO_2 NSs, and their influences on physicochemical properties on this metal oxide are described in this chapter. Thus, open fields and contemporary issues related to SnO_2 NSs are highlighted, and subsequently, the motivation and objectives of the current thesis are developed in the chapter.

In Chapter-2, the detailed synthesis process of SnO_2 QDs along with other dimensions in the nanoscale are described. Additionally, synthesis of SnO_2 1-D NSs using both VLS and VS in three different morphologies, namely square-shaped NWs, cylindrical NWs, and μB, are demonstrated. Further, GO-SnO_2 composites are formed by both in-situ and ex-situ processes. The detailed structural and morphological characterizations of all these lower-dimensional SnO_2 NSs are performed by using XRD, TEM, FESEM, Raman, and IR spectroscopy. The growth temperature of 950 ^{o}C to 1000 ^{o}C during the VLS mechanism results in cylindrical and square-shaped NWs, respectively. Such variation of 1-D NSs is correlated and explained using Gibb's free energy of nucleation formation. Further, Chapter-2 sheds light on the impact of function groups from GO on the shape and size of SnO_2 during the in-situ synthesis of GO-SnO_2 composite. Bigger size with irregular shape found in the in-situ GO-SnO_2 composite compared to the ex-situ process. A non-trivial role of GO on the SnO_2 growth in the composite is demonstrated for the first time.

Chapter-3 describes the in-detail vibrational modes of SnO_2 NPs. Observation of the Raman forbidden but IR active mode is demonstrated using an optimized strong plasmon SERS substrate made up of Ag nanonets. This is explained using GFR theory for 25 nm SnO_2 NPs. The clear presence of a Raman active mode, instead of only a broad feature around 575 cm^{-1} in QD SnO_2 with the presence of SERS substrate, is an important first-time demonstration in chapter -3. Further, the existence of such Raman allowed peak is supported by a high-pressure Raman study of SnO_2 QDs.

PL based NH_3 sensing down to 32 ppm using SnO_2 QDs is discussed in the Chapter-4. This is achieved by showing the enhancement of the two obscured peaks in the blue emission region at 2.7 and 2.96 eV in the presence of NH_3. This chapter also provides an explanation of the origin of blue emission in SnO_2 NPs, which is a longstanding problem for this metal oxide. The origin of blue emission is supported by techniques such as low-temperature PL, EELS, and XAS. This chapter also offers experimental evidence for PL based sensing with a highlight on the Lewis acid-base interaction between the Sn^{4+} as an acid site and NH_3 as a base. This mechanistic aspect is resolved further using the DFT calculation. Apart from the optical sensor, the efficacy of PL arising from defects is also demonstrated in the form of the waveguide for the 1-D NSs in Chapter-4.

For the electrochemical supercapacitor, both pseudo-capacitance and EDLC are important aspects. The first section of Chapter-5 is dedicated to demonstrate the electrochemical utility of SnO_2 QDs and GO-SnO_2 NPs. The crucial role of O_V for better conductivity and hence improved electrochemical capacitance is established for SnO_2 QDs. Further, the chapter discusses an improved capacitance value by the addition of GO, a source of enhanced EDLC with SnO_2 QDs. Further, a comparative study reveals that GO-SnO_2 composite with ex-situ method offers a superior value to the in-situ composite. The ex-situ sample exhibits the presence of the functional group of GO along with uniform SnO_2 NPs. This chapter also explores another important aspect related to the aquatic environment. The utility of SnO_2 NPs for dye degradation under UV light irradiation is demonstrated. Most efficient degradation of MB in less than three minutes under UV C is achieved with SnO_2 QDs as a catalyst. Furthermore, GO-SnO_2 demonstrates brilliant performance by degrading MB within a record of 30 mins under the visible light. The chapter highlights the technical importance of both UV-Visible spectroscopy, PL, and EIS to support the excellent photocatalytic performance of SnO_2 and GO-SnO_2 composites.

The final working chapter-6 illuminates the influence of intrinsic defects in the dielectric property and low-temperature CH_4 sensor. Two types of SnO_2 NPs with similar dimensions but with different defect distributions are synthesized by varying the annealing conditions of SnO_2 QDs. The defect distribution is investigated by EELS and Raman spectroscopy. Anneal in oxygen-deficient conditions is found to be prone to the large formation of V_P type defects. The chapter discusses the pivotal role of such V_P defects in SnO_2 NPs to induce unusually high dielectric value. Furthermore, a low amount of CH_4 detection is clearly demonstrated in the chapter. Moreover, a comparative investigation reveals first-time the typical role of specific defects like V_P in sensing a trace amount of CH_4 at the lowest temperature.

7.2. Conclusion

The significant and new results presented in this thesis are:

1. The revelation of the crucial role of growth temperature to determine the shape of 1-D SnO_2 NSs during VLS technique by using Gibb's free energy minimization.
2. Invoking the Raman forbidden mode in SnO_2 NPs by plasmonic substrates acting as a giant electrical field. The Ag nanonets SERS substrate also allows measuring nearly a single-molecule of R6G with a strong enhancement factor.
3. Selective and wide range of detection of ammonia by simple PL based optical sensors with SnO_2 QDs is achieved and discussed. Clear evidence for the origin of doublet blue emissions from SnO_2 NPs and their role in sensor performance is established.
4. Utilization of 1-D SnO_2 NSs for PL based waveguide application is explained and demonstrated.
5. Exploiting the functional group of GO and superior conductivity of SnO_2 QDs, improved electrochemical hybrid capacitors are demonstrated.
6. Fastest MB degradation within three minutes by SnO_2 QDs as photocatalyst is achieved for the first time. Moreover, visible-light-induced MB degradation is also demonstrated in a record low time, within 30 mins using a GO-SnO_2 composite. The mechanism is also discussed.
7. The role of V_P and V_B in SnO_2 NPs for high dielectric value as well as and CH_4 sensor up to 50 ppm at near room temperature (50 ^oC) is established through a comparative study.

7.3. Future Directions

1. Evaluation and utilization of 1-D NSs for sensors, photocatalysis, and energy-related Li-ion battery and supercapacitor applications.
2. Localized defect study in SnO_2 NSs by more advanced studies like EXAFS, Mossbauer, electron paramagnetic resonance (EPR), and positron anhelation spectroscopy (PAS).
3. Localized sensing study from SnO_2 NSs using tip-enhanced Raman spectroscopy (TERS) and Kelvin probe force microscopy (KPFM).
4. Decoration of plasmonic material and/or doping on SnO_2 for efficient application in photocatalysis and energy application.
5. Inclusion of carbon material like GO, rGO, gC_3N_4 with SnO_2 NPs for enhancing the electrochemical capacitance for device application.
6. Building the theoretical understanding regarding the efficient catalysis activities from SnO_2 with special reference to defects.

Abstract

With excellent success as a resistive-based sensing material, tin oxide (SnO_2) is well-studied among other metal oxides for the last four decades. However, with the recent progress in theoretical understanding and advancement in experimental amenities, SnO_2 is again in the limelight of research. Thanks to the presence of various defects present in this metal oxide like oxygen vacancies (O_V) includes in-plane oxygen vacancy (V_P) and bridging oxygen vacancy (V_B), which influences *n*-type conductivity in SnO_2 and make it a technically important material. However, clear demarcation of such defects in SnO_2 and their influences in various optical, electrical, and vibrational properties need further attention. Additionally, the inclusion of lower dimensions and improved understanding in the synthesis process opens up prominent areas of applications. Hence bringing two important factors, (i) synthesis and understanding the defect in lower dimension SnO_2 and (ii) utilizing these for various applications like resistive and optical-based gas sensing, supercapacitor, waveguide, photocatalysis motivates the current dissertation.

Primarily, a simple chemical route is followed to synthesis SnO_2 QDs, which are further used to obtain different sizes of nanoparticles (NPs) and defects distributions by annealing process in air atmospheres at various temperatures. For morphological and structural characterization of NPs, X-ray diffraction (XRD), transmission electron microscopy (TEM), and field emission secondary electron microscopy (FESEM) are carried out. Further, various spectroscopic investigations such as Raman, photoluminescence (PL), Fourier transfer infrared (FTIR), X-ray absorption spectroscopy (XAS), and electron energy loss spectroscopy (EELS) are carried to elaborate the presence of various defects in SnO_2 NPs and provide explanations for critical properties. Similar techniques are also employed for 1-D SnO_2 nanostructures (NSs) grown by chemical vapor deposition (CVD) by both gold assisted vapor-liquid-solid (VLS) and self-catalytic vapor-solid (VS) process. VLS

technique-grown 1-D NSs is found to hold a strong correlation with the growth temperature and the final shape of the NSs, which is also theoretically established by Gibb's free energy minimization process. Further, for the very first time, the critical role of the functional group of GO in controlling the shape of metal oxide during the growth process is demonstrated and well supported from TEM, FTIR, and Raman spectra.

The current thesis further discusses the impact of a strong plasmonic field on the vibrational properties of low dimensional SnO_2. Optimized SERS substrate obtained by using Ag nanonet enables the first-time observation of Raman allowed A_{1g} mode, which is otherwise hidden underneath defect induced D peak in SnO_2 QDs. Prior to that, the efficiency of this Ag nanonet is proven by single-molecule detection of rhodamine6G (R6G) molecule. Further, "Not mutual exclusion principle," rather the "strong plasmon from Ag nanonet resulted in gradient field Raman (GFR) induced enhancement in infrared (IR) peak" is proposed to be the reason behind the observation of IR allowed E_u(TO) mode during Raman spectra acquisition from 25 nm SnO_2 NPs. Though such GFR effect is profoundly discussed for organic molecules, rarely reported for inorganic molecules like SnO_2.

To overcome the various shortcoming of the resistive-based sensor, an alternative optical-based PL sensor using SnO_2 QDs is proposed. This quest for PL based sensing also helps to solve a long-standing problem regarding the presence of blue emission in the PL spectra for low-dimensional SnO_2 NPs. A rise of two obscured PL peaks in the blue emission region at 2.77, and 2.96 eV is observed in the presence of NH_3. Using this observation SnO_2 QDs detect up to 32 ppm of NH_3 very selectively even at room temperature. The critical role of cationic defects in selective ammonia detection is highlighted experimentally and theoretically. Additionally, PL induced waveguide characteristics of 1-D NSs are also demonstrated. Temperature-dependent PL, along with XAS experiments, is carried out for drawing a suitable band diagram for SnO_2 NSs.

Owing to the surplus surface to volume ratio, the presence of multiple oxidation states (Sn^{2+} and Sn^{4+}) SnO_2 QDs are utilized for electrochemical capacitance application. A gel mediated method is operated for the decoration of QDs on a carbon paper to be utilized as a working electrode. After a successful demonstration of the experiment, graphene oxide and SnO_2 (GO-SnO_2) composite is utilized as electrochemical capacitance by exploiting both electric double-layer capacitor (EDLC) form GO and pseudocapacitance from SnO_2. Along with this, the participation of a functional group of GO for pseudocapacitance adds extra value to the capacitance value. Similarly, for environmental remediation, UV-light driven catalysis study is inspected using SnO_2 NPs. A rapid degradation (< 3 min) of methylene blue by QDs is one the finest result till now using UV-light. While for utilizing the visible light for catalytical dye degradation, GO-SnO_2 composite is adopted. The purpose behind choosing such a composite is also explained, such as exploitation of the higher work function of GO to ensure proper electron transfer. Crucial role defects in improving conductivity are examined by electrochemical impedance spectroscopy (EIS).

Two different types of SnO_2 NPs with different defect distributions but with similar dimensions (~25 nm) are synthesized by annealing the as-prepared QDs in Air and Ar atmospheres. Detailed investigations using Raman spectroscopy and temperature-dependent photoluminescence (PL) measurements propose a strong presence of the in-plane oxygen vacancy in the Ar annealed SnO_2 sample. Despite the similarity in dimensions, Ar annealed sample shows ten times higher dielectric than the air annealed sample. Furthermore, the role of such defects is effectively utilized for near room temperature (50 ^{o}C) CH_4 sensors in a restive way. A detailed explanation for low-temperature performance is presented.

Chapter 1

Introduction

Wide bandgap metal oxide semiconductor reserves a special position among technologically important materials because of the ease of processability and their utilizations in optical, chemical, and electronic applications[1-8]. In the last few decades, wide bandgap semiconductors like ZnO, TiO_2, SnO_2 etc. are explored meticulously[4, 5, 9-18]. Among them, SnO_2 with strong chemical stability and special coexistence of electrical conductivity and transparency in the visible light becomes a pioneering candidate in applications such as a gas sensor for detecting toxic gases, anode materials for lithium-ion batteries for energy harvest, transparent conducting electrodes for flat panel displays, and solar cell, photocatalyst for waste water management and so on.[1, 19-27].

Stoichiometry SnO_2, an IV-VI semiconductor, acts as an insulating material with a large bandgap value of 3.67 eV at room temperature[9, 28-32]. However, low formation energies of defects such as tin interstitials (Sn_i) and oxygen vacancies (O_V) lead to a non-stochiometric form (SnO_x), and these defects introduce an *n*-type character along with a high carrier density of ~ 10^{20} cm^3[27, 33, 34]. This high carrier density is possible because of the generation of electrons in the conduction band (CB) from the donor defect levels in SnO_2 [32, 33, 35, 36]. As the wide bandgap SnO_2 offers transparency in the visible range and a reduction of the luminescent quenching, it has evolved as a material for optical application[37, 38]. SnO_2 has a high excitonic binding energy (130 meV) compared to other wide bandgap materials such as ZnO (60 meV) and GaN (25 meV)[1, 39, 40]. This property makes SnO_2 a worthy candidate for photodetectors, waveguides, and UV light-emitting diodes. Notably, SnO_2 with an inversion centre of symmetry does not show band to band transition because of the dipole forbidden rule[30, 41, 42]. This is because of the long-range symmetry found in bulk SnO_2 leads to the conduction band minimum (CBM) and the valance band maximum (VBM) to occur at Γ (0,0,0) point of the Brillouin zone for an even parity symmetry [43-45]. Thus, the bandgap related optical transition is not allowed. On the other hand, sub-band levels associated with Sn_i and O_V defects inside the forbidden bandgap allows transitions to occur, especially in the visible range[8, 41, 46]. Thus, such defects further open up utilities of SnO_2 in optoelectronic applications. In fact, these defects induced trap states are reported to facilitate photocatalysis activities by delaying the recombination of charge carriers[20, 30, 47]. Moreover, the transition from bulk to nanostructures (NSs) can contribute plenty of defects at surfaces as well as cause a breakdown of the local symmetry, which may lead to breaking of the forbidden band-to-band transition[48]. Apart from that, the multiple oxidation states (Sn^{2+} and Sn^{4+}) and superior conductivity of SnO_2 NSs are found to be beneficial properties for lithium-ion batteries and electrochemical supercapacitor applications[49-52]. Nanostructured SnO_2 with different morphologies such as nanocrystal, core-shell, nanorods (NRs), nanosheet, and nanowires (NWs), with novel properties compared to the bulk, are explored for many applications[23, 53-56]. Hence the controlled synthesis and in-depth understanding of NSs with optimum defects is a necessary step for their effective applications in the many emerging fields.

1.1. Crystal structure

Under the ambient condition, stannic oxide (SnO_2) is the most thermodynamically stable and abundant form of tin oxide[57, 58]. It has a rutile tetragonal structure with a space group *P4₂/mnm* (D^{14}_{4h})[59, 60] and contains four Sn atoms and two O atoms per unit cell, as depicted in Fig.1.1.

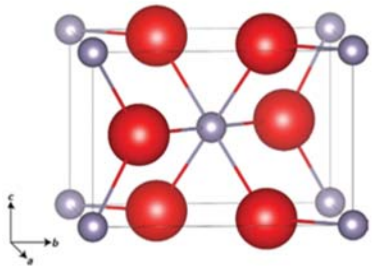

Figure 1.1 SnO_2 unit cell with Sn (IV) state in grey and O in solid.

The atomic position is determined by the c/a ratio and internal parameters. The positions of Sn atoms are defined as (0,0,0) and (0.5,0.5,0.5). Whereas, O atoms are referred to at (0.5, 0.5,0), (-0.5, - 0.5,0), (-u+0.5, u+0.5, 0.5), (u+0.5,-u+0.5, 0.5)[43, 59, 61]. In SnO_2 crystal, Sn is surrounded by six oxygen atoms situated at vertices of a distorted octahedron in which four equatorial oxygen lie in the same plane with a shorter Sn-O bond than the similar bond with the other two oxygen placed at apical site[43, 62].

Various parameters of SnO_2 deduced from experimental and many theoretical approaches are tabulated in Table-1.1[58, 63, 64].The experimental structure gives a= 4.738 Å and c = 3.187 Å with u=0.307 and the c/a ratio of 0.67 and c/a-2u of 0.058 indicate a small distortion of the octahedral.

Table 1.1 Experimental and calculated lattice parameter of SnO_2 [65]

	Exp.	$^{\$}$PBE	*PBE+D3	#PBE0+D3
a (Å)	4.740	4.828 (1.90)	4.808 (1.49)	4.737(-0.02)
c (Å)	3.188	3.243 (1.74)	3.233 (1.43)	3.184 (-0.10)
V (Å^3)	71.63	75.58	74.74 (4.47)	71.45 (-0.13)
c/a	0.673	0.671(-0.15)	0.672 (-0.06)	0.672 (-0.09)
u	0.307	0.307	0.306	0.306
c/a-2u	0.058	0.059	0.060	0.061
Sn-O (2No.) (Å)	2.052	2.091(1.91)	2.085 (1.62)	2.056 (0.20)
Sn-O (2No.) (Å)	2.058	2.093 (1.69)	2.081 (1.13)	2.048 (-0.47)

$^{\$}$PBE: Perdew, Burke, and Ernzerhof (PBE) exchange function

*PBE+D3: Perdew, Burke, and Ernzerhof with Grimme "D3" additive dispersion correction.

#PBE0+D3: PBE0 with D3

1.2. Surface of SnO_2

The optical, electronics, and chemical properties of SnO_2 are reported to be strongly correlated with its low index planes (110), (100), (101), and (001)[43, 64]. It leads to a truncation of the octahedral structure of SnO_2 with dangling bonds and gives rise to different co-ordinations to the outermost cations at surfaces[36]. The stability and material properties of these low index surfaces were found to correspond with the density of dangling bonds present[43]. Out of the above planes, (110) surface, as shown in Fig.1.2, is the most stable surface with the lowest density of dangling bonds. The outermost atomic plane of the stochiometric SnO_2 (110) surface is characterized by the row of oxygen atoms at bridging sites between a pair of Sn atoms, and such oxygen atoms are referred to as bridging oxygen (O_B). The atomic plane lying just below is made up of an alternative row of oxygen and tin atoms[43, 44, 66]. These oxygen atoms are known as in-plane oxygen (O_P). The next plane made up of only oxygen atoms is arranged along a row and is referred to as sub-bridging oxygen (O_{SB}). Removal of an oxygen atom from the respective position creates a bridging oxygen vacancy (V_B), an in-plane oxygen vacancy (V_P), and a sub-bridging oxygen vacancy (V_{SB})[30, 67, 68]. Formation of these oxygen vacancies drastically alters the electrical and optical properties of the metal oxide[69-71]. The effects of these vacancies on various properties are discussed in the subsequent section.

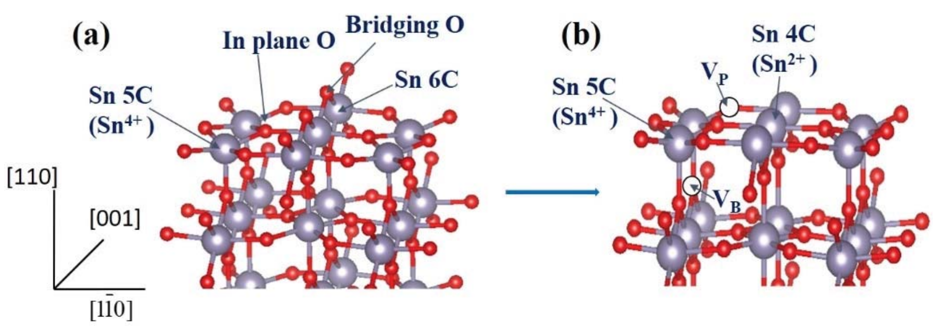

Figure 1.2 Side view of the SnO_2 (110) stoichiometric surfaces. The large (small) spheres represent tin (oxygen) atoms. Oxygen atoms are labelled according to the convention discussed in the text.

With a very high surface to volume ratio and defects states, the metal oxide NS influences applications, and so, the synthesis process is a decisive step to maintain the desirable and pristine characters of NSs. Furthermore, nanocomposite with SnO_2 NSs is an important step to access the beneficial property of it for effective utilization.

1.3. Synthesis of nanomaterials and nanocomposites

Manipulation of shape and size of metal oxides, especially in the nano regime, helps tailoring the mechanical, chemical, magnetic, and electronic properties. In general, metal oxide NSs can be classified as 0-2 Dimensions (0-2D), which are:

(i) Nanoparticles (NPs), Nanosphere, Core-shell structure (0-D).
(ii) Nanorods (NRs), Nanowires (NWs), Nanobelts (NBs), and Nanotube (1-D),
(iii) Nanosheet and Nanoflakes (2-D)

There is good utilization of nanomaterials as nanocomposites to enhance the material properties for efficient applications[72-74]. In that context, carbon materials are highly used for making nanocomposite with various metal oxides. Among the carbon-based materials, 2D graphene has emerged appreciably because of its superior properties such as charge carrier mobility, high specific surface area, excellent optical transparency[75-77]. Reduced graphene oxide (rGO) and graphene oxide (GO) are also popular choices as a graphene precursor material due to ease of processability over the graphene[78, 79]. GO is better considered as a graphene sheet with different functional groups like hydroxyl (-OH) and epoxy (C-O-C) in the basal planes and carbonyl (=CO) and carboxylic (-COOH) at the edges of the graphene flakes. These groups are advantageously utilized for different applications[80, 81]. Unlike graphene, GO opens up an electron energy gap, and the polar oxygen functional groups render it hydrophilic[81, 82]. Further, derivatives with chemical moieties can make the GO dispersible in solvents as well as processable for a series of cheap technological applications such as spraying, drop-cast, or spin-coating. Functional groups in GO serve as sites for binding to metal, metal oxide, and polymers, and thus, GO is used as a starting material for Li-ion battery, supercapacitor, gas sensors, and catalyst applications[78, 81, 83]. The incorporation of metal oxide NSs with novel property and large surfaces to make composites with GO reveals further scope of improvement in performance, such as electrochemical and photocatalysis applications[16, 84].

The techniques to obtain nanostructures with a variety of sizes and shapes are categorized mainly, as bottom-up and top-down. In the bottom-up approach, the NSs are grown from their smallest element by carefully adding unit blocks, such as atoms, ions, or molecules, in order to obtain larger structures[85, 86]. NSs and nanocomposites are obtained routinely by different methods and a brief discussion is given below.

1.3.1. Wet chemistry for NPs synthesis

Wet chemistry is a term used to refer to liquid phase chemistry and the term includes a group of methods, such as liquid phase sol-gel, hydrothermal, spray dry, aerosol spray pyrolysis, cytochemical synthesis[87]. The main advantages of the wet chemistry products compared to solid-phase synthesis for similar products are smaller grains, lower temperature, and shorter duration of phase formation[85, 88]. NPs have been identified as major compounds for many applications such as medicine, optics, electronics, energy, sensing, and catalysis[49, 67, 89]. So, there is a lot of interest in the facile synthetic routes for NPs with controllable size and narrow size distribution. There are many methods for the production of SnO_2 NPs and QDs. Lee *et al.*[41] have reported the synthesis of SnO_2 QDs (1-3 nm) via hydrolysis of $SnCl_2.H_2O$ in ethanol solution, while Castillo *et al.* have reported the preparation of SnO_2 QDs (2-5 nm) by the sol-gel method[90]. A stable and reproducible method is required for the synthesis of these NPs. The growth has to be a sustainable process to yield homogeneous NPs, which may be used as a starting material for the growth of other dimensions and applications.

1.3.2. Vapor-liquid-solid growth

Among many methods of synthesis, 1-D nanostructure is grown by the catalyst assisted vapor-liquid-solid (VLS) process. The mechanism of metal catalysis assisted VLS growth of NWs was proposed by Wagner and Ellis for the growth of silicon whiskers in 1964[91]. During the process, a metal catalyst forms a liquid alloy droplet at higher temperatures, which absorbs the vapor component. The supersaturated alloy droplets drive the precipitation of the vapor component at the liquid-solid interface. Thus, in VLS, a vapor phase precursor is used to supersaturate a liquid catalyst from which a solid phase one-dimensional structure can be achieved by tuning the size of metal particles that act as growth templates for the observed one-dimensional morphology. Most of the semiconductor NWs grown by the VLS mechanism typically show preferential growth in a particular direction in order to minimize the surface energy[85]. However, there are many other kinetic factors, which control the growth and orientation of 1-D nanostructure.

For the growth of 1-D SnO_2 NSs, VLS has been adopted. For instance, Wang *et al.* have demonstrated the importance of substrate used for the growth of NWs by varying A-, M-and R-plane sapphire substrates[92]. With the proper understanding, they obtained NWs of length ~100 μm and used it efficiently for the field-effect transistors (FET) and sensor applications. Zhu *et al.* have successfully co-related the vapor flux with the growth temperature of the VLS process[93]. These studies suggested that in terms of growth kinetics, the temperature is also an important factor for the NWs growth.

1.3.3. Vapor-solid growth

The vapor solid (VS) process relies on the direct crystallization of a solid from the vapor phase or via a self-catalytic process[86]. Though the exact mechanism of it is not clear, there are few reports on the successful growth of 1-D nanostructures through this process. Zhou *et al.* have synthesized SnO_2 nanoribbons on the Si substrate by the thermal evaporation of SnO powder in a horizontal alumina tube at 1000 ^{o}C for 8 h[31]. A similar result was also obtained by McGuire[94] *et al.,* where the NB like morphology was obtained by the thermal evaporation of oxide powder in an alumina tube. The VS growth is explained with the help of Sears's model, where atoms are impinged onto a surface by evaporation and condensation[95]. These fine particles act as nucleation centers. In a VS growth, the preferential growth direction is determined by the surface energy, whereas the morphology is determined by the growth kinetics. The surface with lower energy tends to grow larger and flat, forming the enclosure of nanostructures. The second driving force for VS growth is spontaneous polarization[95]. A polarized surface is a preferred site for newly arriving atoms or molecules. Unlike VLS, where the crystal growth always takes place at a solid/liquid interface, VS-governed growth proceeds at the vapor and solid crystal interface.

1.4. Defects in SnO_2

The presence of various intrinsic defects like oxygen vacancy (O_V), Sn interstitials (Sn_i), Sn antisemites (Sn_O), Sn vacancy (V_{Sn}), and oxygen interstitials control various electrical and chemical properties of SnO_2[30, 32, 36, 96]. For instance, coexistence of optical transparency with electrical conductivity found in SnO_2 is co-related with the presence of O_V. Contrary to this, it has been demonstrated that the presence of hydrogen as a potential source for the n-type conductivity in SnO_2[97]. However, the most expected theory refers to the presence of O_V and Sn_i as the primary donor defects in bulk. It is evident that bulk O_V creates two defect levels $Vo^{\bullet}/Vo^{\times}$ and $Vo^{\bullet\bullet}/Vo^{\bullet}$ at the shallow and deeper positions, respectively[35, 36, 98]. These two defect levels are identified at 0.03 and 0.15 eV below the CB, respectively[36, 98]. Here, $Vo^{\times}$,$Vo^{\bullet}$ and $Vo^{\bullet\bullet}$ are denoted as a neutral, singly charged, and doubly charged vacancy, respectively. As these states lie quite closer to the CBM, they will not affect the transparency but will contribute by improving the electrical conductivity with the injection of carrier electrons into the CB. SnO_2 with a resistivity of 10^4-10^6 Ω cm has considerably lower than other IV-VI semiconductors (10^3-10^9 Ω cm)[98, 99].Additionally, the un-dopped SnO_2 possesses a carrier density up to 10^{20} cm^{-3}, which is comparable with the value of semimetals (10^{20} -10^{20} cm^{-3})[100]. Such a high value is possible because of free electrons created after the ionization of donor states in the solid.

O_V can be regulated by various synthesis methods. For instance, in an oxygen-rich atmosphere, the temperature-dependent O_V reaction can be written as in Knoger-Vink notation[98, 101, 102]:

$$O_o^{\times} \rightarrow V_o^{\bullet} + e + 1/2O_2 \quad \textbf{1.1}$$

$$O_o^{\times} \rightarrow V_o^{\bullet\bullet} + 2e + 1/2O_2 \quad \textbf{1.2}$$

In contrast, in the oxygen-deficient atmosphere, due to lack of oxygen, the reaction follows the following path[102]:

$$V_o^{\times} \rightarrow V_o^{\bullet} + e \quad \textbf{1.3}$$

$$V_o^{\times} \rightarrow V_o^{\bullet\bullet} + 2e \quad \textbf{1.4}$$

These O_V can also be termed as V_P and V_B, as shown in Fig.1.2. Out of these, V_P is found to be a strong contributor to the donor levels that are created close to the CB, whereas the latter one, V_B forms a deep donor state[67]. In the subsequent chapter, the crucial role of these vacancies is further elaborated.

In the rutile tetragonal SnO_2, Sn is surrounded by six oxygen atoms and hence possess a coordination number of six. However, at lower dimensions, a large fraction of the under-coordinated Sn atoms resulting from oxygen vacancies and surface reconstruction process appear in the intrinsic surface states [Fig.1.2]. In this respect, the multivalence of Sn, i.e., Sn^{4+} and $Sn^{2+,}$ drives loss of oxygen from the surface, which creates a nonstoichiometric (110) surface[30, 44, 103]. The absence of O_B decreases the coordination number of Sn from six to four. Furthermore, the reduction of particle size guarantees a very high surface to volume area and thus, proportionately increases the availability of multivalent state and low coordination of Sn at surfaces. Moreover, Sn^{4+} and Sn^{2+} states act as lewis acid that turns out to be a crucial site to interact with a Lewis base. Such base-acid character is well exploited in various catalytic reactions[104, 105]. For instance, the acidic site acted as a decisive point for the oxidation of different analytes like toluene[106]. Further, being positively charged, these sites can act as a trap for the photo-excited electrons and control the optical property. However, a unified approach to exploit various kinds of defects and an understanding of their role in lower dimension metal oxide needs further exploration.

1.5. Electronic structure

The VB and CB is separated by a direct bandgap of 3.67 eV for bulk SnO_2[57]. The VB of SnO_2 can be divided into three different regions based on orbital characters. A simplified representation of the density of state of SnO_2 is depicted in Fig. 1.3.

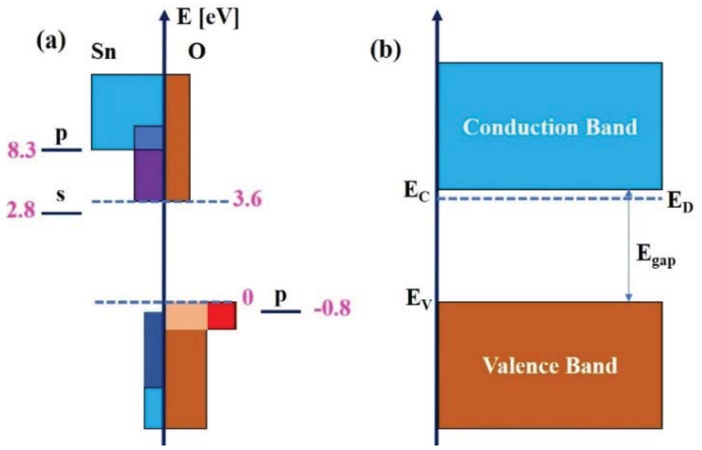

Figure 1.3 Schematic representation of the density of states for valence band and conduction band (b) simplified band diagram of SnO_2 with a donor state (Ed) close to the conduction band.

The valance band maximum (VBM 0 to -2 eV) has a dominant O 2*p* character, while the middle region (-2 to -5 eV) has hybridized Sn 5*p* and O 2*p* orbitals. The lower energy region of VB, -5 to -9 eV, possesses a hybridization of Sn 5*s* states with O 2*p* states, rather than with the Sn 5*p* states[107, 108]. The CB has a minimal contribution of O 2*p* orbitals, whereas its bottom from 3.6 to 8 eV has got a dominant Sn 5*s* character. Further range from 8 to 12 eV has a strong Sn 5*p* character[108].

In the case of the nonstoichiometric SnO_2, the electronic donor states (E_D) close to CB are created by the O_V to make it an *n*-type semiconductor [Fig.1.3(b)]. The removal of oxygen atoms from the surface provides a strong dispersion at the bandgap of SnO_2[43]. On the removal of the most exposed bridging oxygen of the surface, a dispersion band arises within the forbidden gap near the VB, and such states being away from the CB is not energetically favorable for the electrical conduction process easily. However, for an optical transition like luminescence, such states become an important aspect for consideration. In fact, technically important blue luminescence in SnO_2 was correlated to such states[46].

1.6. Vibrational property

The vibrational study offers the detail of bonding and structural information. Each unit cell of SnO_2 consists of six atoms together to have 18 vibrational modes in the first Brillouin zone. These vibrations are represented as[29]:

$$\Gamma = A_{1g} + A_{2g} + B_{1g} + B_{2g} + E_g + A_{2u} + B_{1u} + E_u \quad \textbf{(1.5)}$$

Fig.1.4 represents the schematic view of all vibrational modes[29, 109, 110]:

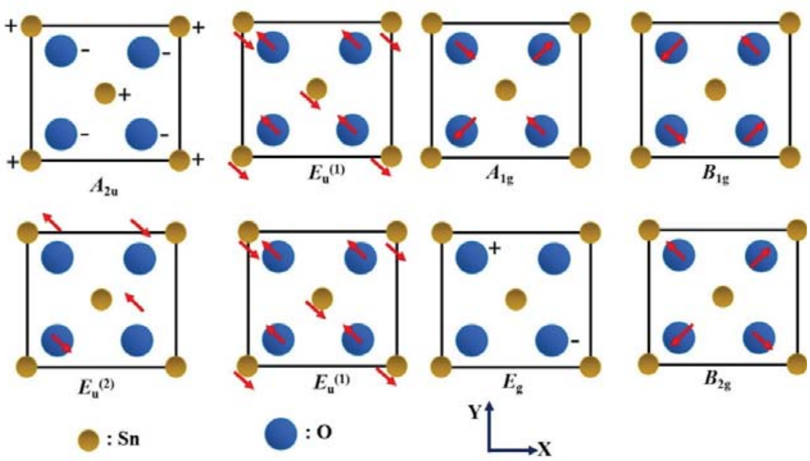

Figure 1.4 2-D representation of optical active vibrational modes along the c-axis of the unit cell and the movement of atoms in-plane is indicated by arrows, while (+) and (-) for movement along the c-axis.

Out of these, non-degenerate A_{2u} and triple-degenerate E_u mode are infrared (IR) active whereas, A_{2u} and two E_u are acoustic modes. Other A_{1g}, B_{1g}, B_{2g}, and E_g modes are Raman active where, first three vibrations are non-degenerate, and the fourth one is doubly degenerate.

All these Raman active vibrations arise due to movements of O atoms with respect to the Sn atom, as evident from the above diagram[29, 111]:

1. A_{1g} and B_{2g} vibrate in the plane perpendicular to the c-axis, while the B_{1g} is due to the rotation of O atoms around the c-axis.
2. E_g mode vibrates along the c-axis.
3. For the IR active A_{2g} mode, Sn and O atoms vibrate in the c-axis direction. The other IR active E_u mode arises due to the vibration of both Sn and O atoms in the plane perpendicular to the c-axis.
4. The vibration of Sn and O atoms in the direction parallel and perpendicular to the c-axis gives rise to the silent B_{1u} and A_{2g} modes, respectively.

However, Raman spectra collected from the SnO_2 NSs vary drastically because of an interaction with EM radiation and particle size, which strongly depends on the shape and state of aggregation[29].

In general, the variations in Raman spectra for NSs are described as follows[29, 109]:

1. Mostly, the Raman allowed peaks A_{1g}, $B_{2g,}$ and E_g centre at the positions ~ 633, 774, and 475 cm^{-1}, respectively. The mode A_{1g} shifts to a lower wavenumber as the size of NPs decreases. At the same time, B_{2g} and E_g move towards $A_{1g,}$ i.e., they shift towards lower and higher wavenumbers, respectively. However, the positional variation of E_g mode is limited, and the shift is found to accompany a broadening effect of the band. Further, B_{1g} mode is reported as a low-frequency band for the

smaller NPs. However, it has a very low intensity with respect to other modes [0.001I (A_{1g}) [29], where I stands for intensity of Raman peak.

2. The appearance of low-frequency bands (50-70 cm^{-1}) whose position and intensity varies with the size of nanoparticles. The band shifts towards a higher wavenumber. Moreover, it becomes a less intense and broad mode than other modes, while the average particle size decreases. For particles larger than ~ 7 nm, the band is not observed in general[112].
3. The Raman forbidden modes such as E_u (TO), A_{2u} (TO), B_{2u}, and A_{2u} (LO) occurring at 248, 502, 544, 694 cm^{-1}, respectively, and the other surface defect-related vibrations are also observed in the SnO_2 NSs due to breakdown of selection rule as a result of the finite size effect. Such Raman modes provide useful information about certain surface defects and disorders present in the NSs[109]. However, it is difficult to identify the presence of all these Raman forbidden modes and surface defect-related vibrational features by conventional Raman spectroscopy due to low intensity from the weak scatterings. The surface-enhanced Raman scattering spectroscopy (SERS), improving the Raman signal significantly, is a potential tool to employ for further details from the finite-size effects or surface defects of SnO_2 nanostructures[31, 113, 114].
4. Besides groups theoretically allowed modes, a broad feature centred at 573 cm^{-1} (*S*) is observed and most prominently in the case of the ultra-small NPs[29]. As the crystalline phase in SnO_2 improves, the feature slowly vanishes with the appearance of other Raman allowed peaks. The origin of the *S* peak is not clearly understood, however it was correlated primarily with O_V[29]. Liu *et al.* have correlated it with V_P [115]. Other studies have described SnO_2 NPs as a crystalline core surrounded by

an amorphous shell and the latter gives rise to the *S* peak in the Raman spectra[29, 116].

1.7. Optical property

The SnO_2 bandgap of 3.67 eV at room temperature (RT)[57] shows a blueshift at lower dimensions, especially when the dimension becomes comparable to its Bohr exciton radius of 2.7 nm. When SnO_2 NPs approaching closely to the Bohr's exciton radius are referred to as quantum dots (QDs)[49]. In a QD, the exciton is confined in all three dimensions. Bandgap energy of the semiconductor QDs is[19, 49]:

$$\boldsymbol{E_g^{eff} = E_g + \frac{h^2}{8\mu r^2} - \frac{1.8e^2}{\varepsilon_r} + \ldots\ldots} \qquad \mathbf{1.6}$$

In the above equation, r is the particle radius, and μ is the effectively reduced mass, and E_g is the bulk bandgap, and ε_r is the dielectric constant.

Though band-to-band emission cannot be seen in SnO_2 due to the dipole forbidden rule, the presence of various defects in low dimension SnO_2 regulates other optical properties[8, 37, 117]. For instance, this metal oxide possesses a broad luminescence peak around 2 eV. Lettieri *et al.* have correlated it to V_B[44]. In another study using the generalized gradient approximation (GGA) and density functional theory (DFT), PL peaks observed at 1.97 and 2.2 eV in SnO_2 NSs were shown to have a link with $V_{B,}$ while an appearance of a luminescent peak at 2.4 eV was assigned to V_P. Thus, the specificity of O_V related defects become a crucial aspect to control the optical properties[44]. Additionally, blue luminescence in SnO_2 in the region of 2.58 to 3.12 eV was reported, and it was found to involve the transitions between the localized states above the VBM and CBM[44, 103]. Zhou *et al.* have elaborated the possible origin of blue luminescence with the help of X-ray absorption near-edge spectroscopy (XANES) and X-ray photoemission spectroscopy (XPS). They have ascribed the observation to a possible transition of a very short lifetime electron from the CBM to an intrinsic surface state[46]. However, the clear distinction of these states with the one created near the CBM was not well demarked. Moreover, finding multiple peaks and their origin in the blue region remains as an open field to reveal and use it for intuitive applications.

1.8. Application of SnO_2 NSs

SnO_2 NSs have attracted immense interest in key technological applications, e.g., gas sensors, optical devices, catalysis, energy storage, biosensors, thanks to their biocompatibility, chemical stability, and environmentally friendly nature[57, 87]. Few applications are enlisted below.

1.8.1. Gas sensors

With the advancement of technology, the gas sensor is becoming one of the important modern electronic components. A resistive-based sensor with a reasonable change in the resistance after an exposure of gas is found to be a reliable way to make such gas sensors[23, 87, 118] in the last two decades for viable applications in public safety, food industry, automobiles, aerospace, and environment safety[87]. The metal oxides like ZnO, SnO_2, CuO have evolved strongly as sensor components[119, 120]. Out of them, SnO_2 is the best suited and oldest metal oxide candidate for commercial gas sensor applications. In recent times, with the introduction of the lower dimension, SnO_2 has also gained further popularity as an efficient sensing material because of its excellent chemical inertness, low cost, non-toxic nature, and, most importantly, large surface to volume ratio[121, 122].

The sensing property is regulated by the adsorption and desorption processes of oxygen at the surface of SnO_2. Oxygen, after adsorbing on the metal oxide, traps the electron and creates a electron depletion region [Fig.1.5 (a)][87, 123]. As a result, the resistance of a metal oxide increases. On reaction with reducing gases like CH_4, NH_3, CO, and H_2 with the adsorbed oxygen, it releases back the electron. Thus, the resistance of the system decreases.

A schematic representation is given in Fig. 1.5 (b) to demonstrate the interaction of CH_4 with SnO_2.

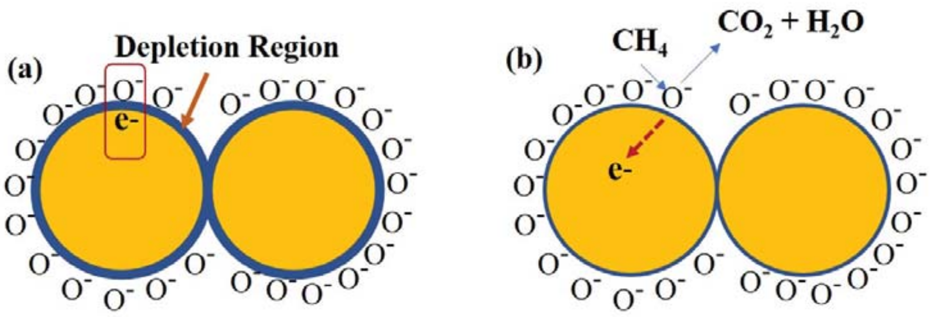

Figure 1.5 (a) Highlight of depletion region formation (b) after effect of an interaction with CH_4 with SnO_2.

For oxidizing gases like NO_2, O_2, and N_2, the resistance of the system increases due to the withdraw of electron from the system[87]. The presence of O_V intrinsic defects was shown to affect the sensing property of metal oxides like SnO_2. For instance, increased V_P in SnO_2 NPs was shown to be responsible for the low-temperature sensing operation[67]. Similarly, the critical role of V_B was correlated for NO_2 sensing by Epifani *et al.* They explained the interaction of NO_2 with the SnO_2 surfaces to occur through the V_B sites, which enhanced the charge transfer for NO_2 interaction[66]. In a different study, an excellent selectivity towards SO_2 at 200 ^oC was demonstrated after introducing O_V in SnO_2 NSs[124]. The presence of O_V was found to promote a reaction between the electron and the adsorbed oxygen. However, the typical role of a particular defect such as V_B or V_P for detection of a trace amount at low temperature remains to be evaluated and understood.

However, the resistive sensor has some serious drawbacks compared to optical sensors. In most of the cases, it needs a high working temperature (more than 200 ^oC) and suffers from slow response, drifts from the baseline resistance, and contact issues. At the same time, optical-based gas sensors with different operational mechanisms may offer an alternative option[14]. As the optical sensors deal with an interaction with the electromagnetic radiation, the sensor involves parameters like intensity, wavelength, polarization[103, 120]. However, there are limited attempts so far to use the optical properties of SnO_2 beneficially for PL based gas sensors[120]. Some studies, such as adsorption of NH_3 with SnO_2 NPs and NO_2 absorption on the SnO_2 NB[103], are reported, however, without details on the active role of specific defects and clear mechanism on the modulation of PL signals by gases. Thus, critical evaluation of various defects, especially blue emission-related deep-down defects, is an important milestone to achieve for a PL sensor.

1.8.2. Electrochemical applications

Electrochemical capacitor, also known as a supercapacitor, has emerged as an excellent energy storage device for the different portable electrical gadgets, electric vehicles, and so many other electrical appliances. High power density, long cyclability, and first charging-discharging response are the crucial parameters to define the effectiveness of an electrochemical capacitor[125-127]. In terms of the energy storage mechanism, a supercapacitor can be of two types, electrical double layer capacitance (EDLC) and pseudocapacitance[52, 125, 126, 128]. The energy storage mechanism in both the process is depicted in Fig.1.6.

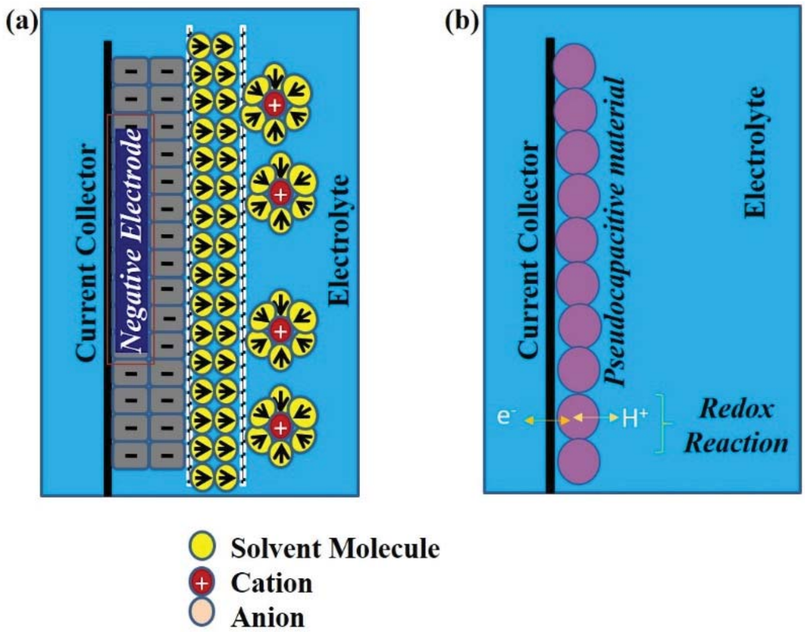

Figure 1.6 Charge storage mechanism in (a) electrical double-layer capacitance and (b) pseudocapacitance.

In the EDLC type process, along with better conductivity, a large surface area leading to the formation of a double layer with an electrolyte is a necessary step[129]. The double-layer formation happens due to the adsorption of positive ions of the electrolyte on the negatively charged electrode and vice-versa. Carbon-based materials such as porous carbon, carbon nanotube, activated carbon, and graphene are found to be the primary choices for EDLC[129-131]. But the limitation of the capacitance value of such materials has restricted their applications. On the other hand, the pseudocapacitance of different metal oxides or conductive polymers can offer a higher capacitance value than the EDLC value[126, 132, 133]. Such capacitive value arises because of the fast-faradic redox reaction. Among different metal oxides, RuO_2 and MnO_2 exhibit high theoretical specific capacitance of 1358 F/g and 1370 F/g, respectively[126, 134]. However, MnO_2 suffers from low conductivity, whereas RuO_2, with good electrical conductivity of (3×10^2 S cm^{-1}), is an expensive rare elemental oxide. In that context, SnO_2 with a theoretical specific capacitance of 760 F/g is the next choice as it is low cost, abundant and non-toxic metal oxide [134, 135]. As discussed before, removal of an oxygen atom from the bridging position contributes to deep trap levels, whereas the V_P causes the formation of an energy band close to the CB by an amount of 0.3 eV provides an improved conductivity[49]. Thus, the synthesis of SnO_2 NPs with large V_P will enhance conductivity. With better conductivity, SnO_2 NPs with high surface areas and defects thus become an appealing material for the supercapacitor application. Furthermore, multiple oxidation states (Sn^{2+} and Sn^{4+}) can offer faradic redox reaction as a pseudo-capacitive material. In addition, a nanostructured metal oxide is an excellent option to enhance the electrochemical performance by manipulation of diffusion length and an increase in the effective area for efficient interaction with an electrolyte. One of the shortcomings of pseudo-capacitive metal oxide is, however, low cyclic stability because of very high-volume change during the electrochemical process [136, 137]. Hence the hybrid capacitor, by combining both EDLC and pseudocapacitance, is an alternative route. In the context of nano-carbon based materials, 2D graphene has emerged strongly because of its superior charge carrier mobility, high specific surface area, and excellent optical transparency. Incorporation of NPs to make NP-graphene composites improve the electrochemical performance[84, 138]. It occurs due to an increase in the distance between the graphene sheets that prohibit stackings into graphitic forms. However, the scalable synthesis of graphene, as well as the incorporation of nanomaterial in graphene or graphene-like structure, remains a challenge for applications. For instance, He *et al.* have explained the growth procedure of Au and Ag NPs in GO and have shown that the ex-situ process can improve the dispersion of NPs in GO over the in-situ process[139]. However, the in-situ process resulted in a composite where the size of metal NPs was not uniform but random. Similarly, metal oxides like Fe_2O_3 and SnO_2NPs were successfully developed to decorate the GO sheets, followed by a thermal reduction[82]. Narrow size distribution with an average size of 10 nm of Fe_3O_4 was observed. Further, Sephra *et al.* demonstrated the usefulness of functionalization with 3-aminopropyl dimethoxy silane for the attachment of positive SnO_2 NPs with the negatively charged GO surfaces[131]. They controlled different sizes of SnO_2 NPs by the pH of the medium. However, they did not elaborate on the typical influence of various functional groups of GO on the growth kinetics. In other reports, rGO-SnO_2 composite was utilized for the Li-ion and supercapacitor applications where, the self-assembly process between the positively charged $Sn(OH)_4$ gel and negatively charged GO took place as an intermediate product, which finally yielded to a rGO-SnO_2 composite after an annealing process. However, any possible interaction between $Sn(OH)_4$ gel and GO during the growth was not discussed[140]. The sensor study using rGO-SnO_2 was reported where the addition of Sn^{4+} precursor to GO to decorate with 10 nm SnO_2 was carried out by hydrothermal process at 180 °C. Here, no pertinent discussion about the growth mechanism considering the possible effect of functional groups of GO was highlighted[141]. In separate work, the Sn^{2+} precursor and the subsequent high temperature (400 ºC) reduction of GO was also realized as an electromagnetic radiation shield [142]. In a more recent study, the functional groups of GO were shown to influence Fe^{2+} to Fe^{3+} conversion and, thus the magnetization of the system[82]. Again here, the growth, size, and morphology of metal oxide NPs were not inter-related to the observation. Importantly, such parameters like size, the role of functional groups influence strongly material properties and various applications. Obviously, there is ample scope to unravel the crucial role of graphene like material on the growth kinetics of SnO_2 NPs in respect to electrochemical or photocatalytic applications.

1.8.3. Utility as a dielectric material

The search for dielectric material continuously attracts the research community because of the demand for microelectronics, miniaturization of devices, and high energy storage material. Material like TiO_2, $BaTiO_3$, $CaCu_3TiO_4O_{12}$,NiO are used for their high dielectric constants[143]. To explain the underlying mechanism for the enhanced dielectric values a)

Internal Barrier Layer Capacitance, b) Structurally frustrated relaxor ferroelectric c) Nano-Order disorder d) Electron-pinned defect dipole are the most proposed mechanism. The dielectric constant of a material like $BaTiO_3$ is related to polarizability, in particular the dipole polarizability, which may find its origin from the structure that has a permanent electric dipole. But some of the materials like $CaCu_3Ti_4O_4$ (CCTO), $Li_xTi_yNi_{1-x-y}O$ are known for their colossal permittivity where the structural aspects play the least role[7, 143, 144]. Preliminarily, peculiar dielectric behavior in a system has been explained in terms of defects and inhomogeneities. Particularly with reference to defects, two proposed mechanisms, surface barrier layer capacitance (SBLC) and internal barrier layer capacitance (IBLC), have been profoundly used to explain the high dielectric value of different ceramic oxides like titanium oxide (TiO_2)[144]. SBLC comes into the picture while the formation of Schottky diodes at the electrode-dielectric interfaces is considered[145, 146]. At the same time, the IBLC reinforces the polarization effect at the insulation grain boundary between semiconducting grain or other internal barriers formed inside the grain. SnO_2, with a bulk dielectric constant ~ 14, has also been explored as a dielectric material for the last two decades. For example, Yongli *et al.* have shown grain boundary-driven IBLC as the key mechanism to describe the higher dielectric value in Al, Nb co-doped SnO_2[147]. Instead of external doping, a self-doping with O_V may be a potential choice to increase the dielectric value considering huge presence in the low-dimensional SnO_2. However, it is yet to be unfurled.

1.8.4. Waveguide application

Sub-wavelength waveguide is becoming a crucial step for the on-chip routing of optical signals[148, 149]. Understanding the morphology, including surface defects, becomes of utmost importance for the control and utility of waveguide propagation in the sub-wavelength waveguides. While the tapered waveguide helps in easy focusing of light, simple surface chemistry can allow selective light propagation by modifying the luminescence[89, 150]. In this direction, 1-D metal oxides like NBs and NWs are potential candidates. For this purpose, the growth of single-crystalline 1D semiconductor NSs with controlled chemical composition, diameter, length, and doping level is a prime requirement [31, 85].

Theoretical calculations on tapered Ag NW waveguide have suggested a slowing down of plasmon polaritons near the tip and subsequent accumulation of energy and giant local fields at the tip[89, 150]. InAsP quantum dot embedded on the axis of an InP tapered NW waveguide was reported for use as a single photon emitter[151, 152]. Davoyan et al. demonstrated using analytical calculations that the tapered dielectric waveguides in the metal block could compensate the mode attenuation as well as enhance the nonlinear interactions with a stable propagation of light[89]. Yang et al. demonstrated single living mammalian cell endoscopy with a high spatial resolution by detecting optical signals from the sub-cellular regions using SnO_2 waveguides. The authors attached SnO_2 NWs of size 100 to 250 nm to the tapered tip of an optical fiber as a probe for the endoscopy, which also showed no toxicity[149]. In most of these cases, an external source was utilized to send light through the 1-D waveguide. Apart from that one more type of waveguide was studied where PL played a very important role for guiding the light through the waveguide[153]. In similar line of application, there is sufficient scope to realize a PL based waveguide with the 1-D SnO_2 NSs.

1.8.5. Photocatalysis application

Synthetic dyes are widely used in various industries like textiles, leather, food, plastic, and cosmetics as a coloring agent, and most of them are toxic and non-biodegradable[154, 155]. Their disposals into natural water bodies impact the environment adversely and intoxicate bio-diversity by preventing the entrance of enough sunlight into an aquatic system. Thus, considerable research interests have been devoted to improving the aquatic environment by degrading the dyes in the water medium, mostly by photocatalytic processes. For a viable photocatalytic activity, nanostructured metal oxides like TiO_2, SnO_2, ZnO, V_2O_5, Fe_2O_3 are hugely investigated and utilized as well in the last two decades as frontier materials[72, 156-158]. Among them, direct bandgap semiconductor, SnO_2 with easy processability, and non-toxic characteristics have attracted enormous attention. Additionally, lowering the dimension from the bulk phase to the quantum confinement domain exhibits distinct properties along with a tremendous increase in specific surfaces[49]. Besides, inherent O_V in SnO_2 that modulates the electronic band structure may favorably be used to enhance the photocatalytic activity. The O_V gives rise to certain energy states inside the band structure. This development promotes better electron migration, an essential criterion for catalytic degradation. In addition, these states can trap the photoexcited electrons and make them available for the catalytic process by prolonging the recombination process. In consequence, the enhanced photocatalytic activity is anticipated due to the defects engineering of SnO_2 NPs. Moreover, nanostructured SnO_2 with an increased number of active reaction sites due to improved surface to volume ratio helps in the improvement of the reaction rate. However, being a wide bandgap material, generally, it needs to be exposed to a UV irradiation source for effective degradation of a dye. On a contrasting note, Liu *et al.* demonstrated using SnO_2 NPs prepared by the pH-regulated microwave synthesis technique a degradation up to 90 % of methylene blue (MB) by means of visible-light-driven photocatalysis[159]. Notably, the degradation took long 240 min. In another report, solar light-driven degradations of Rose Bengal and Eosin Y were demonstrated using microwave synthesized SnO_2 QDs, which also took around 60 min for the complete degradation[47]. The degradation process was explained based on the utilization of solar light that excited an electron from the valance band to the conduction band of the SnO_2 QDs. Towards the meeting of the challenging demand for the faster process under visible light, the various composite of SnO_2 with carbon-related material has been tested[16, 131]. In that regard, rGO is one of the most suitable components for the synthesis of the composite. In contrast, GO with structurally similar to graphene possesses both π-conjugated sp^2 domains and sp^3 character along with oxygenated functional groups present both in the basal and the edge linked through covalent type bonds with graphene carbon atoms. Obviously, the presence of graphene-like characteristics in GO provides a high surface area, and most importantly, it exhibits brilliant adsorption affinity to various dyes[81, 160]. Thus, higher hydrophilicity than the graphene can lead to an improved dispersion and catalytic efficiency through an adsorption mechanism in an aqueous medium. Hence the direct utilization of GO with SnO_2 as a composite for visible-light-driven photocatalysis is still an open challenge.

1.9. The objective of the thesis

The goal of the thesis is to adopt a simple technique to make ultra-small SnO_2, which offers the largest possible surfaces. Such surfaces with pristine defects can then allow novel reaction sites for various applications. Due to large surfaces and defects, the physicochemical properties are thus expected to vary from bulk. Thus, these properties are studied in detail. In addition, various sizes NPs providing different specific surfaces and defects are also compared to arrive at a better understanding of the effectiveness of size and role of defects. Considering possibility of better alignment of the work function of GO with SnO_2 and its improved surface activities, a composite is prepared for evaluation. Thus, the main objectives are built as follows:

1.9.1. Growth of different morphology of SnO_2 NSs and GO-SnO_2 nanocomposite

SnO_2 QDs are synthesized by a soft chemical route, and other dimensions are obtained by annealing it at various temperatures. For the synthesis of 1-D SnO_2 NSs, both

VLS and VS techniques are adopted using a CVD technique. A temperature-controlled morphology is observed for VLS grown 1-D NSs, and the possible growth mechanism is discussed. Nanocomposites with GO are made by ex-situ and in-situ synthesis techniques. The growth mechanism is highlighted along with applications as a hybrid capacitor and visible-light-driven photocatalysts.

1.9.2. Utilization of surface-enhanced Raman spectra to invoke vibrational mode of SnO_2

The important role of a strong plasmonic field to elucidate the Raman forbidden, but IR active mode in 25 nm SnO_2 NPs during the Raman measurement is described with the optimized SERS substrates made with Au NRs and Ag nanonets. Further, a pertinent discussion on how a strong plasmonic Ag nanonets has allowed first-time observation of a Raman allowed mode for the SnO_2 QDs is presented.

1.9.3. Investigation of luminescence from SnO_2 NPs for ammonia sensing and 1-D SnO_2 for waveguide application

Blue luminescence from SnO_2 NPs is probed and discussed in detail using various techniques such as electron energy loss spectroscopy (EELS) and X-ray absorption spectroscopy (XAS). The clear understanding provided a basis for the selective detection of ammonia at RT, for the first time using a blue emission of SnO_2 NPs. The waveguide application of 1-D SnO_2 NSs by using the PL property of a single nanowire is also described.

1.9.4. Efficient use of defects of SnO_2 NPs for supercapacitor and photocatalysis applications

Energy and the environment are two important issues for contemporary and modern research. The thesis emphasizes such important aspects using SnO_2 NPs and nanocomposites with GO e.g., electrochemical hybrid capacitor as a way for energy harvest and photocatalytic dye degradation for environmental application.

1.9.5. Role of the defect in controlling dielectric and CH_4 sensing properties of SnO_2 NPs

Two different SnO_2 NPs with similar dimensions but with different defect distribution are synthesized. The typical role of O_V related defects on enhancing dielectric values is discussed with a plausible mechanism. Furthermore, the role of O_V defects is highlighted for low temperature (50 °C) CH_4 sensing, especially with an explanation on the specific influence of V_P and V_B in sensor mechanism for detecting the lowest possible trace amount.

1.10. References

[1] E.N. Dattoli, Q. Wan, W. Guo, Y. Chen, X. Pan, W. Lu, Fully transparent thin-film transistor devices based on SnO_2 nanowires, Nano letters, 7 (2007) 2463-2469.
[2] Y.-J. Choi, I.-S. Hwang, J.-G. Park, K.J. Choi, J.-H. Park, J.-H. Lee, Novel fabrication of an SnO_2 nanowire gas sensor with high sensitivity, Nanotechnology, 19 (2008) 095508.
[3] Y. Ryu, T.-S. Lee, J.A. Lubguban, H.W. White, B.-J. Kim, Y.-S. Park, C.-J. Youn, Next generation of oxide photonic devices: ZnO-based ultraviolet light emitting diodes, Applied Physics Letters, 88 (2006) 241108.
[4] J. Jiang, J. Olsen, L. Gerward, D. Frost, D. Rubie, J. Peyronneau, Structural stability in nanocrystalline ZnO, EPL (Europhysics Letters), 50 (2000) 48.
[5] W. Zhao, W. Ma, C. Chen, J. Zhao, Z. Shuai, Efficient degradation of toxic organic pollutants with Ni_2O_3/TiO_2-x B x under visible irradiation, Journal of the American Chemical Society, 126 (2004) 4782-4783.
[6] Y. Wu, X. Zhao, J. Zhang, W. Su, J. Liu, Huge low-frequency dielectric response of (Nb, In)-doped TiO_2 ceramics, Applied Physics Letters, 107 (2015) 242904.
[7] W. Hu, K. Lau, Y. Liu, R.L. Withers, H. Chen, L. Fu, B. Gong, W. Hutchison, Colossal dielectric permittivity in (Nb+ Al) codoped rutile TiO_2 ceramics: compositional gradient and local structure, Chemistry of Materials, 27 (2015) 4934-4942.
[8] S. Luo, J. Fan, W. Liu, M. Zhang, Z. Song, C. Lin, X. Wu, P.K. Chu, Synthesis and low-temperature photoluminescence properties of SnO2 nanowires and nanobelts, Nanotechnology, 17 (2006) 1695.
[9] I. Manassidis, J. Goniakowski, L. Kantorovich, M. Gillan, The structure of the stoichiometric and reduced SnO_2 (110) surface, Surface Science, 339 (1995) 258-271.
[10] F. Jones, R. Dixon, J. Foord, R. Egdell, J. Pethica, The surface structure of SnO_2 (110)(4× 1) revealed by scanning tunneling microscopy, Surface science, 376 (1997) 367-373.
[11] J. Oviedo, M. Gillan, Energetics and structure of stoichiometric SnO_2 surfaces studied by first-principles calculations, Surface Science, 463 (2000) 93-101.
[12] G.A. Alanko, A. Thurber, C.B. Hanna, A. Punnoose, Size, surface structure, and doping effects on ferromagnetism in SnO_2, Journal of Applied Physics, 111 (2012) 07C321.
[13] L. Liu, T. Li, X. Wu, J. Shen, P. Chu, Identification of oxygen vacancy types from Raman spectra of SnO_2 nanocrystals, Journal of Raman Spectroscopy, 43 (2012) 1423-1426.
[14] S. Pati, S. Majumder, P. Banerji, Role of oxygen vacancy in optical and gas sensing characteristics of ZnO thin films, Journal of Alloys and Compounds, 541 (2012) 376-379.
[15] X. Li, Y. Chen, A. Kumar, A. Mahmoud, J.A. Nychka, H.-J. Chung, Sponge-templated macroporous graphene network for piezoelectric ZnO nanogenerator, ACS applied materials & interfaces, 7 (2015) 20753-20760.

[16] Y. Feng, N. Feng, Y. Wei, G. Zhang, An in situ gelatin-assisted hydrothermal synthesis of ZnO–reduced graphene oxide composites with enhanced photocatalytic performance under ultraviolet and visible light, RSC advances, 4 (2014) 7933-7943.
[17] J.S. Olsen, L. Gerward, J. Jiang, On the rutile/α-PbO2-type phase boundary of TiO_2, Journal of Physics and Chemistry of Solids, 60 (1999) 229-233.
[18] I. Felner, R. Herber, S. Acharya, V.P.S. Awana, The origin of ferromanetism in Ni-doped ZnO and SnO_2 Modern Physics Letters B, 24 (2010) 125-134.
[19] J. Du, R. Zhao, Y. Xie, J. Li, Size-controlled synthesis of SnO_2 quantum dots and their gas-sensing performance, Applied Surface Science, 346 (2015) 256-262.
[20] S.P. Kim, M.Y. Choi, H.C. Choi, Photocatalytic activity of SnO_2 nanoparticles in methylene blue degradation, Materials Research Bulletin, 74 (2016) 85-89.
[21] E.P. Stuckert, C.J. Miller, E.R. Fisher, The Effect of Ar/O_2 and H_2O Plasma Treatment of SnO2 Nanoparticles and Nanowires on Carbon Monoxide and Benzene Detection, ACS Applied Materials & Interfaces, 9 (2017) 15733-15743.
[22] G.-Z. Zang, X.-F. Wang, H.-H. Liu, F.-Z. Zhou, L.-B. Li, Varistor and giant permittivity properties of SnO_2–Zn_2SnO_4 ceramic matrix composites, Journal of Materials Science: Materials in Electronics, 27 (2016) 9836-9841.
[23] S.S. Kim, H.G. Na, H.W. Kim, V. Kulish, P. Wu, Promotion of acceptor formation in SnO_2 nanowires by e-beam bombardment and impacts to sensor application, Scientific reports, 5 (2015) 10723.
[24] J. Gong, Q. Chen, M.-R. Lian, N.-C. Liu, R.G. Stevenson, F. Adami, Micromachined nanocrystalline silver doped SnO_2 for H_2S sensor, Sensors and Actuators B: Chemical, 114 (2006) 32-39.
[25] J. Pan, L. Wang, C.Y. Jimmy, G. Liu, H.-M. Cheng, A nonstoichiometric $SnO_{2-\delta}$ nanocrystal-based counter electrode for remarkably improving the performance of dye-sensitized solar cells, Chemical Communications, 50 (2014) 7020-7023.
[26] I. Kim, J. Ko, D. Kim, K. Lee, T. Lee, J.-H. Jeong, B. Cheong, Y.-J. Baik, W. Kim, Scattering mechanism of transparent conducting tin oxide films prepared by magnetron sputtering, Thin Solid Films, 515 (2006) 2475-2480.
[27] Ç. Kılıç, A. Zunger, Origins of Coexistence of Conductivity and Transparency in SnO_2, Physical Review Letters, 88 (2002).
[28] J.D. Prades García, First-principles study of NO_x and SO_2 adsorption onto SnO_2 (110) and SnO_2 nanoparticles, (2007).
[29] A. Dieguez, A. Romano-Rodrıguez, A. Vila, J. Morante, The complete Raman spectrum of nanometric SnO_2 particles, Journal of Applied Physics, 90 (2001) 1550-1557.
[30] S. Ghosh, K. Das, K. Chakrabarti, S.K. De, Effect of oleic acid ligand on photophysical, photoconductive and magnetic properties of monodisperse SnO_2 quantum dots, Dalton Trans, 42 (2013) 3434-3446.
[31] W. Zhou, R. Liu, Q. Wan, Q. Zhang, A. Pan, L. Guo, B. Zou, Bound exciton and optical properties of SnO2 one-dimensional nanostructures, The Journal of Physical Chemistry C, 113 (2009) 1719-1726.
[32] Z. Jarzebski, J. Marton, Physical properties of SnO_2 materials: I. preparation and defect structure, Journal of the electrochemical Society, 123 (1976) 199C.
[33] Y. Porte, R. Maller, H. Faber, H.N. AlShareef, T.D. Anthopoulos, M.A. McLachlan, Exploring and controlling intrinsic defect formation in SnO_2 thin films, Journal of Materials Chemistry C, 4 (2016) 758-765.
[34] A.K. Singh, A. Janotti, M. Scheffler, C.G. Van de Walle, Sources of electrical conductivity in SnO_2, Physical review letters, 101 (2008) 055502.
[35] S. Samson, C. Fonstad, Defect structure and electronic donor levels in stannic oxide crystals, Journal of Applied Physics, 44 (1973) 4618-4621.
[36] K.G. Godinho, A. Walsh, G.W. Watson, Energetic and electronic structure analysis of intrinsic defects in SnO_2, The Journal of Physical Chemistry C, 113 (2008) 439-448.
[37] F. Gu, S.F. Wang, M.K. Lü, G.J. Zhou, D. Xu, D.R. Yuan, Photoluminescence properties of SnO_2 nanoparticles synthesized by sol-gel method, The Journal of Physical Chemistry B, 108 (2004) 8119-8123.

[38] A. Schleife, J. Varley, F. Fuchs, C. Rödl, F. Bechstedt, P. Rinke, A. Janotti, C. Van de Walle, Tin dioxide from first principles: Quasiparticle electronic states and optical properties, Physical Review B, 83 (2011) 035116.
[39] S. Sheng Pan, S. Fung Yu, Y. Xia Zhang, Y. Yuan Luo, S. Wang, J. Min Xu, G. Hai Li, Crystallite size-modulated exciton emission in SnO_2 nanocrystalline films grown by sputtering, Journal of applied physics, 113 (2013) 143104.
[40] S. Brovelli, N. Chiodini, R. Lorenzi, A. Lauria, M. Romagnoli, A. Paleari, Fully inorganic oxide-in-oxide ultraviolet nanocrystal light emitting devices, Nature communications, 3 (2012) 1-9.
[41] E.J. Lee, C. Ribeiro, T. Giraldi, E. Longo, E. Leite, J.A. Varela, Photoluminescence in quantum-confined SnO_2 nanocrystals: evidence of free exciton decay, Applied Physics Letters, 84 (2004) 1745-1747.
[42] N.S. Pesika, K.J. Stebe, P.C. Searson, Determination of the particle size distribution of quantum nanocrystals from absorbance spectra, Advanced Materials, 15 (2003) 1289-1291.
[43] F. Trani, M. Causà, D. Ninno, G. Cantele, V. Barone, Density functional study of oxygen vacancies at the SnO_2 surface and subsurface sites, Physical Review B, 77 (2008) 245410.
[44] S. Lettieri, M. Causà, A. Setaro, F. Trani, V. Barone, D. Ninno, P. Maddalena, Direct role of surface oxygen vacancies in visible light emission of tin dioxide nanowires, The Journal of chemical physics, 129 (2008) 244710.
[45] Y. Duan, Electronic properties and stabilities of bulk and low-index surfaces of SnO in comparison with Sn O_2: A first-principles density functional approach with an empirical correction of van der Waals interactions, Physical Review B, 77 (2008) 045332.
[46] X. Zhou, F. Heigl, M. Murphy, T. Sham, T. Regier, I. Coulthard, R. Blyth, Time-resolved x-ray excited optical luminescence from SnO_2 nanoribbons: Direct evidence for the origin of the blue luminescence and the role of surface states, Applied physics letters, 89 (2006) 213109.
[47] A. Bhattacharjee, M. Ahmaruzzaman, A novel and green process for the production of tin oxide quantum dots and its application as a photocatalyst for the degradation of dyes from aqueous phase, Journal of colloid and interface science, 448 (2015) 130-139.
[48] S.S. Pan, S.F. Yu, W.F. Zhang, H. Zhu, W. Lu, L.M. Jin, Low threshold amplified spontaneous emission from tin oxide quantum dots: a instantiation of dipole transition silence semiconductors, Nanoscale, 5 (2013) 11561-11567.
[49] V. Bonu, B. Gupta, S. Chandra, A. Das, S. Dhara, A. Tyagi, Electrochemical supercapacitor performance of SnO_2 quantum dots, Electrochimica Acta, 203 (2016) 230-237.
[50] W.-H. Qu, F. Han, A.-H. Lu, C. Xing, M. Qiao, W.-C. Li, Combination of a SnO_2–C hybrid anode and a tubular mesoporous carbon cathode in a high energy density non-aqueous lithium ion capacitor: preparation and characterisation, Journal of Materials Chemistry A, 2 (2014) 6549-6557.
[51] W. Wang, P. Li, Y. Fu, X. Ma, The preparation of double-void-space SnO_2/carbon composite as high-capacity anode materials for lithium-ion batteries, Journal of Power Sources, 238 (2013) 464-468.
[52] Z. Yu, L. Tetard, L. Zhai, J. Thomas, Supercapacitor electrode materials: nanostructures from 0 to 3 dimensions, Energy & Environmental Science, 8 (2015) 702-730.
[53] Y. Dai, S. Tang, J. Peng, H. Chen, Z. Ba, Y. Ma, X. Meng, MnO_2@ SnO_2 core–shell heterostructured nanorods for supercapacitors, Materials Letters, 130 (2014) 107-110.
[54] S. Luo, P.K. Chu, W. Liu, M. Zhang, C. Lin, Origin of low-temperature photoluminescence from SnO_2 nanowires fabricated by thermal evaporation and annealed in different ambients, Applied Physics Letters, 88 (2006) 183112.
[55] J. Prades, R. Jimenez-Diaz, F. Hernandez-Ramirez, S. Barth, A. Cirera, A. Romano-Rodriguez, S. Mathur, J. Morante, Ultralow power consumption gas sensors based on self-heated individual nanowires, Applied Physics Letters, 93 (2008) 123110.
[56] M. Sun, Q. Zhao, X. Liu, C. Du, Z. Liu, Comparative study on sandwich-structured SiO_2@ Ag@ SnO_2 and inverse SiO_2@ SnO_2@ Ag: key roles of shell ordering and interfacial contact in modulating the photocatalytic properties, RSC Advances, 5 (2015) 81059-81068.
[57] M. Batzill, U. Diebold, The surface and materials science of tin oxide, Progress in Surface Science, 79 (2005) 47-154.

[58] W.H. Baur, A.A. Khan, Rutile-type compounds. IV. SiO_2, GeO_2 and a comparison with other rutile-type structures, Acta Crystallographica Section B: Structural Crystallography and Crystal Chemistry, 27 (1971) 2133-2139.
[59] T. Yamanaka, R. Kurashima, J. Mimaki, X-ray diffraction study of bond character of rutile-type SiO_2, GeO_2 and SnO_2, Zeitschrift für Kristallographie-Crystalline Materials, 215 (2000) 424-428.
[60] Y. He, J. Liu, W. Chen, Y. Wang, H. Wang, Y. Zeng, G. Zhang, L. Wang, J. Liu, T. Hu, High-pressure behavior of SnO_2 nanocrystals, Physical Review B, 72 (2005) 212102.
[61] H. Hellwig, A.F. Goncharov, E. Gregoryanz, H.-k. Mao, R.J. Hemley, Brillouin and Raman spectroscopy of the ferroelastic rutile-to-$CaCl_2$ transition in SnO_2 at high pressure, Physical Review B, 67 (2003) 174110.
[62] S. Ghosh, G. Sahoo, S. Polaki, N.G. Krishna, M. Kamruddin, T. Mathews, Enhanced supercapacitance of activated vertical graphene nanosheets in hybrid electrolyte, Journal of Applied Physics, 122 (2017) 214902.
[63] D.O. Scanlon, G.W. Watson, On the possibility of p-type SnO_2, Journal of Materials Chemistry, 22 (2012) 25236-25245.
[64] P. Ágoston, K. Albe, R.M. Nieminen, M.J. Puska, Intrinsic n-type behavior in transparent conducting oxides: A comparative hybrid-functional study of In_2O_3, SnO_2, and ZnO, Physical review letters, 103 (2009) 245501.
[65] G. Korotcenkov, Tin Oxide Materials: Synthesis, Properties, and Applications, Elsevier, 2019.
[66] M. Epifani, J.D. Prades, E. Comini, E. Pellicer, M. Avella, P. Siciliano, G. Faglia, A. Cirera, R. Scotti, F. Morazzoni, The role of surface oxygen vacancies in the NO_2 sensing properties of SnO_2 nanocrystals, The Journal of Physical Chemistry C, 112 (2008) 19540-19546.
[67] V. Bonu, A. Das, A.K. Prasad, N.G. Krishna, S. Dhara, A. Tyagi, Influence of in-plane and bridging oxygen vacancies of SnO_2 nanostructures on CH_4 sensing at low operating temperatures, Applied Physics Letters, 105 (2014) 243102.
[68] G. Santarossa, K. Hahn, A. Baiker, Free Energy and Electronic Properties of Water Adsorption on the SnO_2(110) Surface, Langmuir : the ACS journal of surfaces and colloids, 29 (2013) 5487-5499.
[69] S. Mehraj, M.S. Ansari, A.A. Al-Ghamdi, Annealing dependent oxygen vacancies in SnO_2 nanoparticles: Structural, electrical and their ferromagnetic behavior, Materials Chemistry and Physics, 171 (2016) 109-118.
[70] V. Bonu, A. Das, S. Amirthapandian, S. Dhara, A.K. Tyagi, Photoluminescence of oxygen vacancies and hydroxyl group surface functionalized SnO_2 nanoparticles, Physical Chemistry Chemical Physics, 17 (2015) 9794-9801.
[71] N. Li, K. Du, G. Liu, Y. Xie, G. Zhou, J. Zhu, F. Li, H.-M. Cheng, Effects of oxygen vacancies on the electrochemical performance of tin oxide, Journal of Materials Chemistry A, 1 (2013) 1536-1539.
[72] S.P. Vattikuti, P.A.K. Reddy, J. Shim, C. Byon, Visible-Light-Driven Photocatalytic Activity of SnO_2–ZnO Quantum Dots Anchored on g-C_3N_4 Nanosheets for Photocatalytic Pollutant Degradation and H_2 Production, ACS Omega, 3 (2018) 7587-7602.
[73] K.C. Lam, B. Huang, S.-Q. Shi, Room-temperature methane gas sensing properties based on in situ reduced graphene oxide incorporated with tin dioxide, Journal of Materials Chemistry A, 5 (2017) 11131-11142.
[74] X. Chu, J. Wang, J. Zhang, Y. Dong, W. Sun, W. Zhang, L. Bai, Preparation and gas-sensing properties of SnO_2/graphene quantum dots composites via solvothermal method, Journal of Materials Science, 52 (2017) 9441-9451.
[75] K.P. Loh, Q. Bao, G. Eda, M. Chhowalla, Graphene oxide as a chemically tunable platform for optical applications, Nature chemistry, 2 (2010) 1015.
[76] S. Stankovich, D.A. Dikin, R.D. Piner, K.A. Kohlhaas, A. Kleinhammes, Y. Jia, Y. Wu, S.T. Nguyen, R.S. Ruoff, Synthesis of graphene-based nanosheets via chemical reduction of exfoliated graphite oxide, carbon, 45 (2007) 1558-1565.
[77] A.C. Ferrari, D.M. Basko, Raman spectroscopy as a versatile tool for studying the properties of graphene, Nature nanotechnology, 8 (2013) 235.

[78] S. Víctor-Román, E. García-Bordejé, J. Hernández-Ferrer, J.M. González-Domínguez, A. Ansón-Casaos, A.M. Silva, W.K. Maser, A.M. Benito, Controlling the surface chemistry of graphene oxide: key towards efficient ZnO-GO photocatalysts, Catalysis Today, (2019).
[79] P.V. Kumar, M. Bernardi, J.C. Grossman, The impact of functionalization on the stability, work function, and photoluminescence of reduced graphene oxide, ACS nano, 7 (2013) 1638-1645.
[80] Y.J. Oh, J.J. Yoo, Y.I. Kim, J.K. Yoon, H.N. Yoon, J.-H. Kim, S.B. Park, Oxygen functional groups and electrochemical capacitive behavior of incompletely reduced graphene oxides as a thin-film electrode of supercapacitor, Electrochimica Acta, 116 (2014) 118-128.
[81] S. Song, Y. Ma, H. Shen, M. Zhang, Z. Zhang, Removal and recycling of ppm levels of methylene blue from an aqueous solution with graphene oxide, RSC Advances, 5 (2015) 27922-27932.
[82] S. Majumder, M. Sardar, B. Satpati, S. Kumar, S. Banerjee, Magnetization Enhancement of Fe3O4 by Attaching onto Graphene Oxide: An Interfacial Effect, The Journal of Physical Chemistry C, 122 (2018) 21356-21365.
[83] B. Bhangare, N.S. Ramgir, S. Jagtap, A. Debnath, K. Muthe, C. Terashima, D.K. Aswal, S.W. Gosavi, A. Fujishima, XPS and Kelvin probe studies of SnO_2/RGO nanohybrids based NO_2 sensors, Applied Surface Science, 487 (2019) 918-929.
[84] K. Zhao, L. Zhang, R. Xia, Y. Dong, W. Xu, C. Niu, L. He, M. Yan, L. Qu, L. Mai, SnO_2 Quantum Dots@ Graphene Oxide as a High-Rate and Long-Life Anode Material for Lithium-Ion Batteries, Small, 12 (2016) 588-594.
[85] B. Wang, Y. Yang, N. Xu, G. Yang, Mechanisms of size-dependent shape evolution of one-dimensional nanostructure growth, Physical Review B, 74 (2006) 235305.
[86] B. Wang, Y. Yang, C. Wang, G. Yang, Nanostructures and self-catalyzed growth of SnO_2, Journal of Applied Physics, 98 (2005) 073520.
[87] S. Das, V. Jayaraman, SnO_2: a comprehensive review on structures and gas sensors, Progress in Materials Science, 66 (2014) 112-255.
[88] D. Chandra, N. Mukherjee, A. Mondal, A. Bhaumik, Design and synthesis of nanostructured porous SnO_2 with high surface areas and their optical and dielectric properties, The Journal of Physical Chemistry C, 112 (2008) 8668-8674.
[89] A.R. Davoyan, I.V. Shadrivov, A.A. Zharov, D.K. Gramotnev, Y.S. Kivshar, Nonlinear nanofocusing in tapered plasmonic waveguides, Physical review letters, 105 (2010) 116804.
[90] J. Del-Castillo, A. Yanes, J. Méndez-Ramos, V. Rodríguez, Luminescence of Nanostructured SnO_2-SiO_2 Glass-Ceramics Prepared Sol–Gel Method, Journal of Nanoscience and Nanotechnology, 8 (2008) 2143-2146.
[91] R. Wagner, W. Ellis, Vapor-liquid-solid mechanism of single crystal growth, Applied physics letters, 4 (1964) 89-90.
[92] X. Wang, N. Aroonyadet, Y. Zhang, M. Mecklenburg, X. Fang, H. Chen, E. Goo, C. Zhou, Aligned epitaxial SnO_2 nanowires on sapphire: growth and device applications, Nano letters, 14 (2014) 3014-3022.
[93] Z. Zhu, M. Suzuki, K. Nagashima, H. Yoshida, M. Kanai, G. Meng, H. Anzai, F. Zhuge, Y. He, M.l. Boudot, Rational Concept for Reducing Growth Temperature in Vapor–Liquid–Solid Process of Metal Oxide Nanowires, Nano letters, 16 (2016) 7495-7502.
[94] K. Mcguire, Z. Pan, Z. Wang, D. Milkie, J. Menendez, A. Rao, Raman studies of semiconducting oxide nanobelts, Journal of nanoscience and nanotechnology, 2 (2002) 499-502.
[95] X. Fang, L. Zhang, Controlled growth of one-dimensional oxide nanomaterials, Cailiao Kexue Yu Jishu(Journal of Materials Science & Technology), 22 (2006) 1-18.
[96] D.F. Cox, T.B. Fryberger, S. Semancik, Oxygen vacancies and defect electronic states on the SnO 2 (110)-1× 1 surface, Physical Review B, 38 (1988) 2072.
[97] W.H. Oo, S. Tabatabaei, M. McCluskey, J. Varley, A. Janotti, C. Van de Walle, Hydrogen donors in SnO_2 studied by infrared spectroscopy and first-principles calculations, Physical Review B, 82 (2010) 193201.
[98] G. Zhang, C. Xie, S. Zhang, L. Yang, Y. Xiong, D. Zeng, Temperature-and Atmosphere-Dependent Defect Chemistry Model of SnO_2 Nanocrystalline Film, Journal of the American Ceramic Society, 97 (2014) 2091-2098.

[99] W. Izydorczyk, Numerical analysis of an influence of oxygen adsorption at a SnO2 surface on the electronic parameters of the induced depletion layer, physica status solidi (b), 248 (2011) 694-699.
[100] G. Gasparro, J. Pütz, D. Ganz, M.A. Aegerter, Parameters affecting the electrical conductivity of SnO_2: Sb sol–gel Coatings, Solar energy materials and solar cells, 54 (1998) 287-296.
[101] J.N. Zemel, Theoretical description of gas-film interaction on SnO_x, Thin Solid Films, 163 (1988) 189-202.
[102] A. Gurlo, R. Riedel, In situ and operando spectroscopy for assessing mechanisms of gas sensing, Angewandte Chemie International Edition, 46 (2007) 3826-3848.
[103] S. Lettieri, A. Setaro, C. Baratto, E. Comini, G. Faglia, G. Sberveglieri, P. Maddalena, On the mechanism of photoluminescence quenching in tin dioxide nanowires by NO_2 adsorption, New Journal of Physics, 10 (2008) 043013.
[104] A. Marikutsa, M. Rumyantseva, A. Gaskov, A. Samoylov, Nanocrystalline tin dioxide: Basics in relation with gas sensing phenomena part II. Active centers and sensor behavior, Inorganic Materials, 52 (2016) 1311-1338.
[105] A.V. Marikutsa, M.N. Rumyantseva, E.A. Konstantinova, T.B. Shatalova, A.M. Gaskov, Active sites on nanocrystalline tin dioxide surface: Effect of palladium and ruthenium oxides clusters, The Journal of Physical Chemistry C, 118 (2014) 21541-21549.
[106] Y. Liu, Y. Liu, Y. Guo, J. Xu, X. Xu, X. Fang, J. Liu, W. Chen, H. Arandiyan, X. Wang, Tuning SnO_2 surface area for catalytic toluene deep oxidation: on the inherent factors determining the reactivity, Industrial & Engineering Chemistry Research, 57 (2018) 14052-14063.
[107] S. Munnix, M. Schmeits, Electronic structure of tin dioxide surfaces, Physical Review B, 27 (1983) 7624.
[108] J.M. Themlin, R. Sporken, J. Darville, R. Caudano, J. Gilles, R. Johnson, Resonant-photoemission study of SnO_2: cationic origin of the defect band-gap states, Physical Review B, 42 (1990) 11914.
[109] V. Bonu, A. Das, A. Sivadasan, A. Tyagi, S. Dhara, Invoking forbidden modes in SnO_2 nanoparticles using tip enhanced Raman spectroscopy, Journal of Raman Spectroscopy, 46 (2015) 1037-1040.
[110] T. Livneh, Y. Lilach, I. Popov, A. Kolmakov, M. Moskovits, Polarized raman scattering from a single, segmented SnO_2 wire, The Journal of Physical Chemistry C, 115 (2011) 17270-17277.
[111] P. Peercy, B. Morosin, Pressure and temperature dependences of the Raman-active phonons in SnO_2, Physical Review B, 7 (1973) 2779.
[112] L. Ying-Kai, D. Yi, W. Guang-Hou, Low-frequency and abnormal Raman spectrum in SnO_2 nanorods, Chinese Physics Letters, 21 (2004) 156.
[113] E. Fazio, F. Neri, S. Savasta, S. Spadaro, S. Trusso, Surface-enhanced Raman scattering of SnO_2 bulk material and colloidal solutions, Physical Review B, 85 (2012) 195423.
[114] H. Wei, A. McCarthy, J. Song, W. Zhou, P.J. Vikesland, Quantitative SERS by hot spot normalization–surface enhanced Rayleigh band intensity as an alternative evaluation parameter for SERS substrate performance, Faraday discussions, 205 (2017) 491-504.
[115] L.Z. Liu, J.Q. Xu, X.L. Wu, T.H. Li, J.C. Shen, P.K. Chu, Optical identification of oxygen vacancy types in SnO_2 nanocrystals, Applied Physics Letters, 102 (2013) 031916.
[116] L.P. Ravaro, L.V. Scalvi, A.S. Tabata, F.M. Pontes, J.B. Oliveira, Nanoparticle characterization of Er-doped SnO_2 pellets obtained with different pH of colloidal suspension, Journal of Applied Physics, 114 (2013) 084304.
[117] B.K. Sahu, G. Kaur, A. Das, Revealing Interplay of Defects in SnO_2 quantum dots for blue luminescence and selective trace ammonia detection at room temperature, ACS Applied Materials & Interfaces, (2020).
[118] P. Sun, Y. Cai, S. Du, X. Xu, L. You, J. Ma, F. Liu, X. Liang, Y. Sun, G. Lu, Hierarchical α-Fe_2O_3/SnO_2 semiconductor composites: Hydrothermal synthesis and gas sensing properties, Sensors and Actuators B: Chemical, 182 (2013) 336-343.
[119] X. Liu, B. Du, Y. Sun, M. Yu, Y. Yin, W. Tang, C. Chen, L. Sun, B. Yang, W. Cao, Sensitive room temperature photoluminescence-based sensing of H_2S with novel CuO–ZnO nanorods, ACS applied materials & interfaces, 8 (2016) 16379-16385.

[120] N. Singh, V. Pandey, N. Singh, M. Malik, F.Z. Haque, Application of TiO_2/SnO_2 nanoparticles in photoluminescence based fast ammonia gas sensing, Journal of Optics, 46 (2017) 199-203.
[121] H.C. Su, M. Zhang, W. Bosze, N.V. Myung, Tin dioxide functionalized single-walled carbon nanotube (SnO_2/SWNT)-based ammonia gas sensors and their sensing mechanism, Journal of The Electrochemical Society, 161 (2014) B283-B290.
[122] A. Biaggi-Labiosa, F. Sola, M. Lebrón-Colón, L. Evans, J. Xu, G. Hunter, G. Berger, J. Gonzalez, A novel methane sensor based on porous SnO_2 nanorods: room temperature to high temperature detection, Nanotechnology, 23 (2012) 455501.
[123] A. Das, V. Bonu, A.K. Prasad, D. Panda, S. Dhara, A.K. Tyagi, The role of SnO_2 quantum dots in improved CH_4 sensing at low temperature, Journal of Materials Chemistry C, 2 (2014) 164-171.
[124] L. Liu, S. Liu, Oxygen vacancies as an efficient strategy for promotion of low concentration SO_2 gas sensing: the case of Au-modified SnO_2, ACS Sustainable Chemistry & Engineering, 6 (2018) 13427-13434.
[125] P. Simon, Y. Gogotsi, Materials for electrochemical capacitors, Nature materials, 7 (2008) 845.
[126] B. Conway, Electrochemical Supercapacitors: Sci-entific Fundamentals and Technological Applications. Kluwer-Plenum, (1999).
[127] J. Huang, B.G. Sumpter, V. Meunier, Theoretical model for nanoporous carbon supercapacitors, Angewandte Chemie International Edition, 47 (2008) 520-524.
[128] J.R. Miller, P. Simon, Electrochemical capacitors for energy management, Science Magazine, 321 (2008) 651-652.
[129] Z.-S. Wu, G. Zhou, L.-C. Yin, W. Ren, F. Li, H.-M. Cheng, Graphene/metal oxide composite electrode materials for energy storage, Nano Energy, 1 (2012) 107-131.
[130] A. Singh, A. Chandra, Significant performance enhancement in asymmetric supercapacitors based on metal oxides, carbon nanotubes and neutral aqueous electrolyte, Scientific reports, 5 (2015) 15551.
[131] P.J. Sephra, P. Baraneedharan, M. Sivakumar, T.D. Thangadurai, K. Nehru, Size controlled synthesis of SnO_2 and its electrostatic self-assembly over reduced graphene oxide for photocatalyst and supercapacitor application, Materials Research Bulletin, 106 (2018) 103-112.
[132] T. Brousse, D. Bélanger, J.W. Long, To be or not to be pseudocapacitive?, Journal of The Electrochemical Society, 162 (2015) A5185-A5189.
[133] C. Costentin, T.R. Porter, J.-M. Savéant, How do pseudocapacitors store energy? Theoretical analysis and experimental illustration, ACS applied materials & interfaces, 9 (2017) 8649-8658.
[134] Y. Dai, S. Tang, J. Peng, H. Chen, Z. Ba, Y. Ma, X. Meng, MnO_2@ SnO_2 core–shell heterostructured nanorods for supercapacitors, Materials Letters, 130 (2014) 107-110.
[135] B.K. Sahu, A. Das, Significance of oxygen defects in SnO_2 quantum dots as hybrid electrochemical capacitors, Journal of Physics and Chemistry of Solids, (2019).
[136] B. Wang, D. Guan, Z. Gao, J. Wang, Z. Li, W. Yang, L. Liu, Preparation of graphene nanosheets/SnO_2 composites by pre-reduction followed by in-situ reduction and their electrochemical performances, Materials Chemistry and Physics, 141 (2013) 1-8.
[137] R. Liang, H. Cao, D. Qian, J. Zhang, M. Qu, Designed synthesis of SnO_2-polyaniline-reduced graphene oxide nanocomposites as an anode material for lithium-ion batteries, Journal of Materials Chemistry, 21 (2011) 17654-17657.
[138] Y.G. Zhu, Y. Wang, J. Xie, G.-S. Cao, T.-J. Zhu, X. Zhao, H.Y. Yang, Effects of graphene oxide function groups on SnO_2/graphene nanocomposites for lithium storage application, Electrochimica Acta, 154 (2015) 338-344.
[139] F.-A. He, J.-T. Fan, F. Song, L.-M. Zhang, H.L.-W. Chan, Fabrication of hybrids based on graphene and metal nanoparticles by in situ and self-assembled methods, Nanoscale, 3 (2011) 1182-1188.
[140] Y. Wang, J. Ding, Y. Liu, Y. Liu, Q. Cai, J. Zhang, SnO_2@ reduced graphene oxide composite for high performance lithium-ion battery, Ceramics International, 41 (2015) 15145-15152.
[141] Z. Wang, T. Zhang, T. Han, T. Fei, S. Liu, G. Lu, Oxygen vacancy engineering for enhanced sensing performances: A case of SnO_2 nanoparticles-reduced graphene oxide hybrids for

ultrasensitive ppb-level room-temperature NO_2 sensing, Sensors and Actuators B: Chemical, 266 (2018) 812-822.
[142] M. Mishra, A.P. Singh, B.P. Singh, S. Dhawan, Performance of a nanoarchitectured tin oxide@ reduced graphene oxide composite as a shield against electromagnetic polluting radiation, RSC Advances, 4 (2014) 25904-25911.
[143] P. Lunkenheimer, V. Bobnar, A. Pronin, A. Ritus, A. Volkov, A. Loidl, Origin of apparent colossal dielectric constants, Physical Review B, 66 (2002) 052105.
[144] S. Sarkar, P.K. Jana, B. Chaudhuri, Colossal internal barrier layer capacitance effect in polycrystalline copper (II) oxide, Applied Physics Letters, 92 (2008) 022905.
[145] P. Bueno, E. Leite, M. Oliveira, M. Orlandi, E. Longo, Role of oxygen at the grain boundary of metal oxide varistors: A potential barrier formation mechanism, Applied Physics Letters, 79 (2001) 48-50.
[146] Y. Song, X. Wang, Y. Sui, Z. Liu, Y. Zhang, H. Zhan, B. Song, Z. Liu, Z. Lv, L. Tao, Origin of colossal dielectric permittivity of rutile $Ti_{0.9}In_{0.05}Nb_{0.05}O_2$: single crystal and polycrystalline, Scientific reports, 6 (2016).
[147] Y. Song, X. Wang, X. Zhang, X. Qi, Z. Liu, L. Zhang, Y. Zhang, Y. Wang, Y. Sui, B. Song, Colossal dielectric permittivity in (Al+ Nb) co-doped rutile SnO_2 ceramics with low loss at room temperature, Applied Physics Letters, 109 (2016) 142903.
[148] M.H. Huang, S. Mao, H. Feick, H. Yan, Y. Wu, H. Kind, E. Weber, R. Russo, P. Yang, Room-temperature ultraviolet nanowire nanolasers, science, 292 (2001) 1897-1899.
[149] R. Yan, J.-H. Park, Y. Choi, C.-J. Heo, S.-M. Yang, L.P. Lee, P. Yang, Nanowire-based single-cell endoscopy, Nature nanotechnology, 7 (2012) 191-196.
[150] M.I. Stockman, Nanofocusing of optical energy in tapered plasmonic waveguides, Physical review letters, 93 (2004) 137404.
[151] M.A. Versteegh, M.E. Reimer, K.D. Jöns, D. Dalacu, P.J. Poole, A. Gulinatti, A. Giudice, V. Zwiller, Observation of strongly entangled photon pairs from a nanowire quantum dot, Nature communications, 5 (2014).
[152] M.E. Reimer, G. Bulgarini, N. Akopian, M. Hocevar, M.B. Bavinck, M.A. Verheijen, E.P. Bakkers, L.P. Kouwenhoven, V. Zwiller, Bright single-photon sources in bottom-up tailored nanowires, Nature communications, 3 (2012) 737.
[153] L. Zhang, G. Wu, F. Gu, H. Zeng, Single MoO_3 nanoribbon waveguides: good building blocks as elements and interconnects for nanophotonic applications, Scientific reports, 5 (2015).
[154] C.A. Martínez-Huitle, E. Brillas, Decontamination of wastewaters containing synthetic organic dyes by electrochemical methods: a general review, Applied Catalysis B: Environmental, 87 (2009) 105-145.
[155] A.M. Al-Hamdi, U. Rinner, M. Sillanpää, Tin dioxide as a photocatalyst for water treatment: a review, Process Safety and Environmental Protection, 107 (2017) 190-205.
[156] S.P. Vattikuti, C. Byon, C.V. Reddy, R. Ravikumar, Improved photocatalytic activity of MoS 2 nanosheets decorated with SnO 2 nanoparticles, RSC Advances, 5 (2015) 86675-86684.
[157] S.J. Moniz, S.A. Shevlin, D.J. Martin, Z.-X. Guo, J. Tang, Visible-light driven heterojunction photocatalysts for water splitting–a critical review, Energy & Environmental Science, 8 (2015) 731-759.
[158] J. Ding, B. Li, Y. Liu, X. Yan, S. Zeng, X. Zhang, L. Hou, Q. Cai, J. Zhang, Fabrication of Fe_3O_4@ reduced graphene oxide composite via novel colloid electrostatic self-assembly process for removal of contaminants from water, Journal of Materials Chemistry A, 3 (2015) 832-839.
[159] X. Liu, L. Pan, T. Chen, J. Li, K. Yu, Z. Sun, C. Sun, Visible light photocatalytic degradation of methylene blue by SnO_2 quantum dots prepared via microwave-assisted method, Catalysis Science & Technology, 3 (2013) 1805-1809.
[160] S. Ma, S. Zhan, Y. Jia, Q. Zhou, Highly efficient antibacterial and Pb (II) removal effects of Ag-$CoFe_2O_4$-GO nanocomposite, ACS applied materials & interfaces, 7 (2015) 10576-10586.

Chapter 2

Growth and characterization of SnO_2 NSs and GO-SnO_2 composite

In the current chapter, the synthesis of SnO_2 NPs of different dimensions (0-D and 1-D) is elaborated. A soft chemical method is employed for the synthesis of SnO_2 QDs, which are further annealed at various temperatures to obtain different sizes of 0-D NPs. Further, the synthesis of 1-D SnO_2 NSs, including NWs and micro belts (μBs), using the CVD technique is carried out. The synthesis of 1-D NSs follows both catalytic controlled VLS and self-catalytic controlled VS mechanism. The crucial role of the growth temperature in regulating the shape and size of 1-D NSs is discussed in detail. Besides the 0-D and 1-D NSs, this chapter also discusses synthesis and characterization of GO-SnO_2 composites, prepared by the ex-situ and the in-situ methods. Characterizations of these NSs are carried out using FESEM, TEM, and XRD. Additionally, different spectroscopic techniques like Raman and FTIR are used for the understanding of structural and optical properties of SnO_2 NSs and composites.

2.1. Synthesis and characterization of SnO_2 NPs

A soft chemical route is employed for the synthesis of SnO_2 QDs, followed by annealing at different temperatures[1]. In detail, 0.05 mol/L ammonia solution (NH_4OH; Merck) is added dropwise to an aqueous 1 M stannic chloride ($SnCl_4$). DI water (MilliQ, 18 MΩ) is used throughout the procedure. After the addition of the NH_4OH solution, the obtained white colloidal liquid is kept in a hot bath for 45 min at a temperature of 80 ^oC. The resultant white precipitate is washed repeatedly with DI water and alcohol to remove the chlorine ion. The collected gel is dried at 100 ^oC temperature overnight and is referred to as A (100 ^oC) or the as-prepared sample[1]. The sample is further annealed isothermally in a horizontal tube in the air atmosphere at 300, 500, and 800 ^oC to acquire different particle sizes. These annealed samples at different temperatures are termed as B (300 ^{o}C), C (500 ^{o}C), and D (800 ^{o}C), respectively.

2.1.1. X-Ray diffraction analysis of NPs

For structural analysis of SnO_2 NPs, X-ray diffraction (XRD) spectra using a Cu-Kα1 radiation (λ=0.15406 nm) are recorded in the 2θ range from 20 to 80^{o}. The obtained diffraction peaks are depicted in Fig. 2.1. All of the samples illustrate peaks at 2θ value of 26.5^{o}, 33.8^{o}, 51.7^{o}, 64.7^{o} which match to the planes (110), (101), (211), and (112) of the rutile tetragonal of SnO_2 crystal, respectively (ICDD 00-041-1445)[1, 2]. These peaks are quite broad for samples A and B. The broadening of diffraction peaks is ascribed to the presence of short-range order in a very small crystallite like QDs and the non-uniform strain in NPs. In contrast, an improved crystalline phase due to heat treatment is obtained with sharper peaks for samples C and D than the samples, A and B.

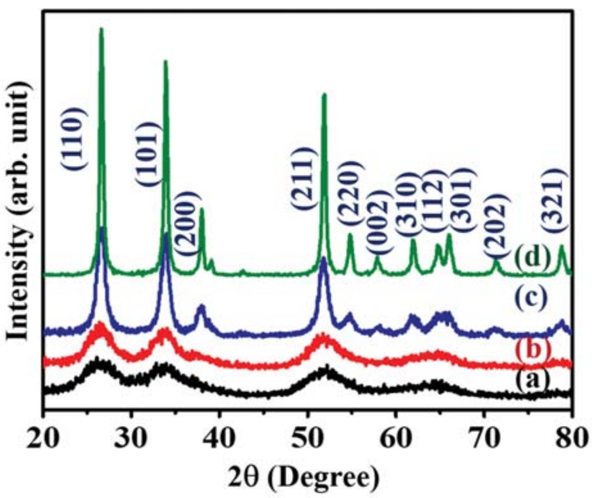

Figure 2.1 XRD of samples (a) A (100 ^{o}C), (b) B (300 ^{o}C), (c) C (500 ^{o}C), and (d) D (800 ^{o}C)

Further, diffraction peaks of sample A are fitted with a gaussian peak and shown in Fig. 2.2 to obtain full width half maximum (FWHM) of corresponding peaks.

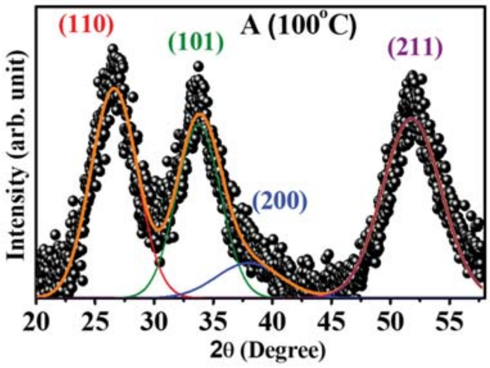

Figure 2.2 Gaussian fitting of XRD patterns of A (100 °C)

The Scherrer equation[3], R= 0.89λ/βcosθ, where R= mean crystallite size, β= FWHM is used for all samples to calculate the mean crystallite size. Thus, average sizes of NPs are found to be 1.9±0.1, 3.9±0.2, 8.3±0.5, and 25±0.3 nm for A, B, C, and D, respectively.

2.1.2. Transmission electron microscopy studies

The structural properties of synthesized NPs are validated by the TEM study. Fig.2.3 (a) represents the TEM image of sample A, whereas, Fig.2.3 (b) depicts particle size distribution. The spherical particle of size 2 to 2.8 nm is well distributed and a Gaussian distribution with peaks at 2.4 nm. These particles are less than the Bohr exciton radius of SnO_2 (2.7 nm) and are therefore referred to as QDs[4].

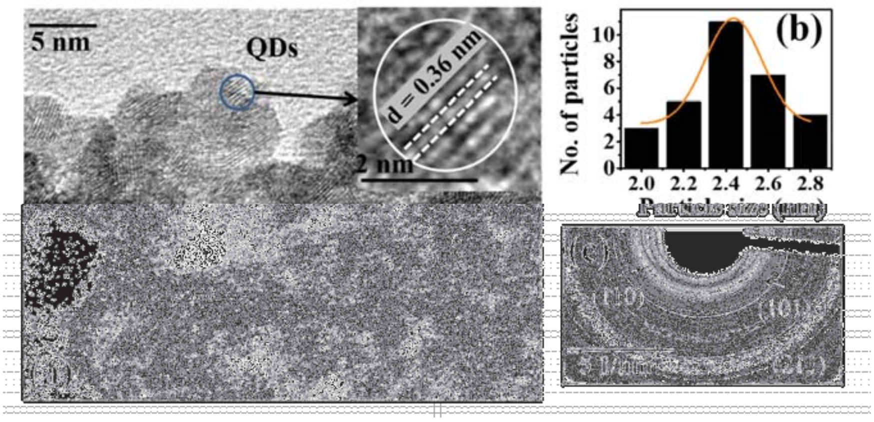

Figure 2.3 (a) HRTEM image of SnO_2 QDs with an inter-planar spacing value as inset, (b) Particle size distribution with a Gaussian fitting and (c) the SAED pattern of sample A(100 °C)

Further Fig. 2.3 (a) inset shows an HRTEM image of SnO_2 with an interplanar d. spacing value equal to 0.36 nm, which closely matches with the (110) rutile structure of SnO_2. The ring-like selected area electron diffraction (SAED) patterns shown in Fig. 2.3 (c) can be indexed to (110), (101), and (211) planes, which again correspond to the rutile SnO_2 phase. The blurring SAED rings suggest the presence of short-range order for the SnO_2 QDs.

The TEM images collected from sample B (300 ^oC) are shown in Fig 2.4 (a). The inset shows the interplanar *d* spacing of the (110) plane of SnO_2. The mean diameter of this sample is found to be around 4.1 nm from the Gaussian distribution fitting, as depicted in Fig. 2.4 (b). Further, the SAED patterns in Fig. 2.4 (c) depict the (110), (101), and (211) planes of the rutile SnO_2 phase.

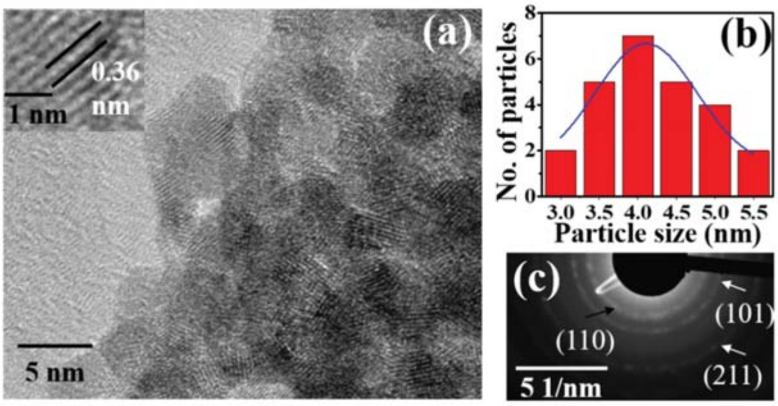

Figure 2.4 (a) HRTEM image of the sample B (300 ^oC) with interplanar spacing as inset, (b) Particle size distribution with Gaussian fitting and (c) SAED patterns

Fig.2.5 (a) shows the TEM images of sample C (500 ^oC), and the inset shows an interplanar spacing corresponding to the (110) plane of SnO_2. From Fig. 2.5 (b), the average particle size is found to be ~9.3 nm. The SAED pattern shown in Fig. 2.5 (c) confirms the (110), (101), and (211) planes for the rutile SnO_2 crystal. An improved crystallinity is suggested from the spotty ring pattern feature of the SAED pattern [Fig. 2.5 (c)] compared to samples A and B.

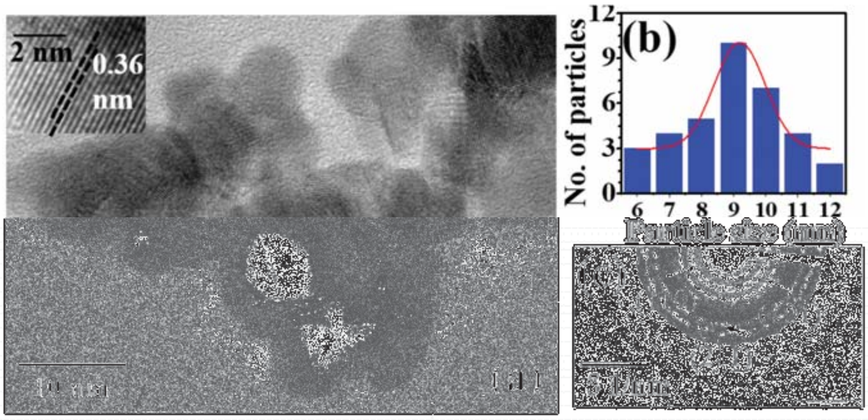

Figure 2.5 (a) HRTEM image of the sample C (500 °C) with interplanar spacing as inset, (b) Particle size distribution with Gaussian fitting and (c) SAED patterns

The TEM image of the annealed sample at 800 °C is shown in Fig. 2.6 (a). The interplanar spacing equal to 0.36 nm for the (110) plane of SnO_2 is also shown as an inset. The mean diameter is observed to be ~ 24 nm after the Gaussian fitting of the particle size distribution [Fig. 2.6 (b)]. The spotty ring pattern in SAED indicates an enhanced crystalline structure. They are indexed as (110), (101), and (211) planes for the rutile SnO_2 structure.

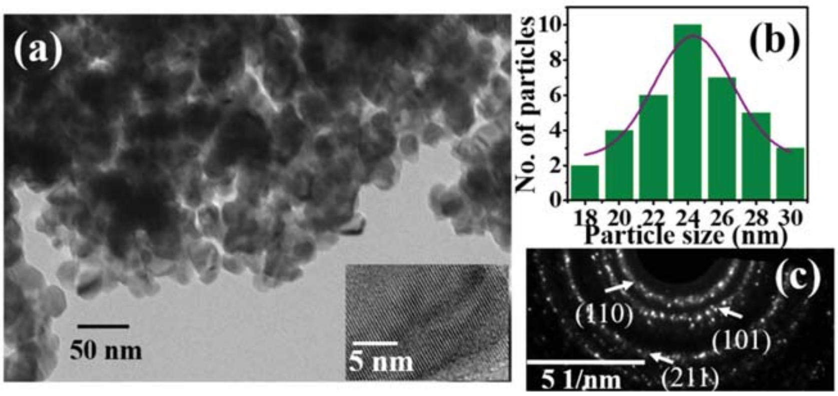

Figure 2.6 (a) HRTEM image (inset) interplanar spacing, (b) Particle size distribution with Gaussian fitting, and (c) SAED pattern of sample D (800 °C)

2.1.3. Vibrational spectroscopy of SnO_2 NPs

Raman scattering is sensitive to the local structure and crystal surface area. It is a powerful tool for the characterization of nanomaterials and provides a qualitative probe for the lattice defects in solids. [5]. Micro-Raman spectroscopy (InVia; Renishaw) using 514.5 nm excitation from the Ar^+ laser with 1800 gr. mm^{-1} grating and thermoelectric cooled CCD detector is employed to collect Raman signal from all the samples in the backscattering configuration and the spectra are shown in Fig. 2.7.

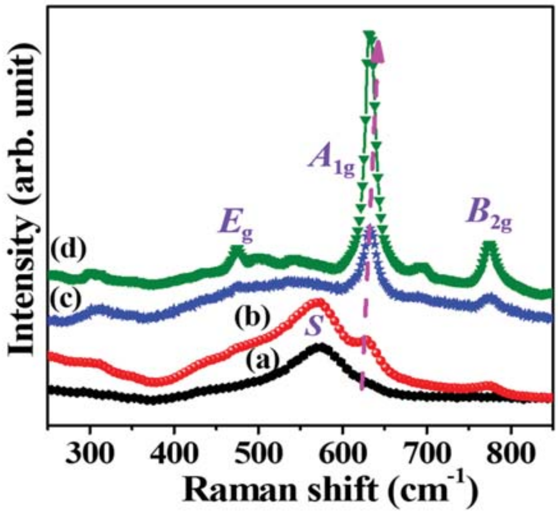

Figure 2.7 Raman spectra of SnO_2 NPs (a) A (100 ^oC), (b) B (200 ^oC), (c) C (500 ^oC) and (d) D (800 ^oC).

Raman spectra of SnO_2 NPs indicate structural evolution depending on the annealing temperature. Instead of allowed Raman modes, a broad feature at 573 cm^{-1} is recorded for sample A. This peak is still observable for sample B with a particle size of ~ 4 nm. Comparatively, a sharp Raman peak at 633 cm^{-1}, along with a peak at 774 cm^{-1} of sample D, is observed. A systematic blue shift of those peaks is observed with the increase in annealing temperature. Furthermore, E_g mode is found to shift to a lower value while the B_{2g} mode to a higher value in the Raman spectra for NPs with the increased annealing temperature. The broad feature in sample A (*S* peak) originates due to surface defects such as oxygen vacancies and the non-stoichiometric composition of SnO_2 NPs. The intensity of the peak reduces with increasing particle size[5-7]. Details about this defect induced *S* peak is discussed in Chapter-3 and 6.

Further vibrational properties of SnO_2 NPs are elaborated by the FTIR study, and the result is depicted in Fig. 2.8 in the following figure.

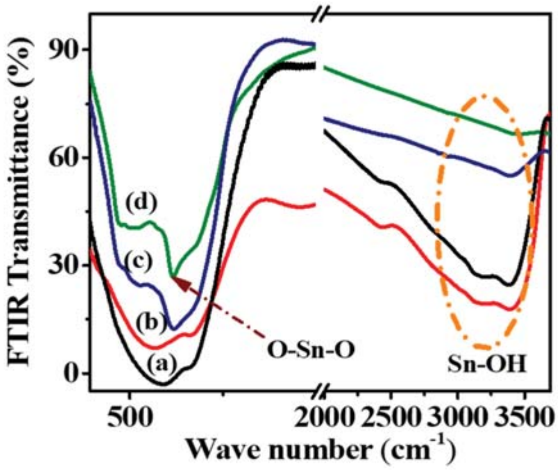

Figure 2.8 FTIR spectra of (a) A (100 ºC), (b) B (200 ºC), (c) C (500 ºC) and (d) D (800 ºC)

A peak at 624 cm^{-1} assigned to O-Sn-O vibrational mode is found to be strongest for the biggest particle of sample D. The peak is not clearly seen for smaller particles, like samples A and B. Apart from this peak, a peak is observed at 3400 cm^{-1}, which corresponds to the Sn-OH vibration mode[8, 9]. Notably, the mode is quite strong for smaller particles with large surfaces and indicates the presence of a high amount of -OH in samples A and B.

2.2. Synthesis and characterization of 1-D SnO_2 NSs

The present section describes the growth of 1-D SnO_2 NSs by the atmospheric chemical vapor deposition (APCVD) technique[10]. Two different growth mechanisms: (1) Vapor Liquid Solid (VLS) and (2) Vapor Solid (VS) technique, are discussed[10].

2.2.1. Atmospheric pressure chemical vapor deposition

The fundamental steps in chemical vapor deposition (CVD) techniques are as follows [11, 12]:

(1) Convective and diffusive transport of single of multiple reactant species to the suitable substrate kept in the reaction zone.

(2) The heterogeneous reaction of these species on the substrate surface by means of adsorption, diffusion, and desorption process leading to the nucleation.

(3) Rational attachment of the reactant's species leading to the growth of nuclei and transport of volatile substances and the reaction by-products from the reaction zone.

For the growth of 1-D SnO_2 NSs, a custom lab-made CVD set up is utilized (Fig. 2.9).

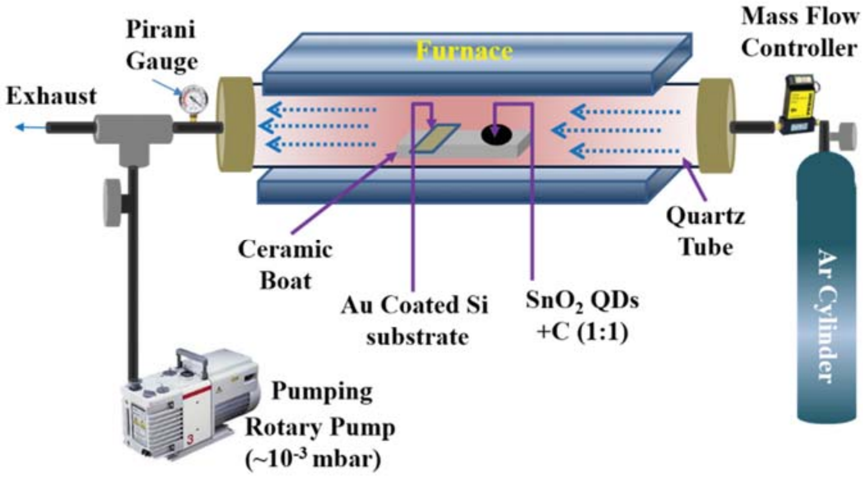

Figure 2.9 Schematic representation of the CVD system used for the growth of various forms of SnO_2 nanostructures.

The important components of the system are listed below:

1. High temperature vacuum tube (1300 °C) furnace (GSL-1300X, MTI Corporation, USA). The furnace temperature profile is set up by using 51 segments with the automatic run by 708p type advanced PID controller. The furnace consists a) heating element: SiC rod, b). Temperature zone: 20 cm, c) Thermocouple: S type Pt-Rh.
2. Quartz tube with 2.7 cm diameter and 130 cm in length is used as a reacting chamber.
3. Rotary vacuum pump (Edward RV3 50 1/m with oil mist filter) is used for the pre-evacuation of the chamber down to 1 mbar.
4. Mass flow controller (Aalborg GFC 57/67/77): 10-1000 sccm for Ar gas (Commercial 97 %)
5. Pirani Vacuum Gauge: monitoring vacuum inside the chamber -1000 to 1×10^{-3} mbar.

The VLS growth is a catalyst assisted mechanism and, Au (5 nm) deposited by thermal evaporation (Model 15F6, HINDHIVAC) on the Si (110) substrate is used as a catalyst to control the VLS growth for 1-D NSs.

2.2.2. Vapor-liquid solid growth

A mixture of SnO_2 QDs with graphite powder (Alfa Aesar, 99.9995%) is used in a 3:1 weight ratio as a precursor material and kept in an Al_2O_3 boat (99.99 %). The Si (100) coated with ~ 5 nm of Au is used as a substrate and is kept 1 cm away from the precursor material on the same Al_2O_3 boat in the direction of carrier gas (Ar). Here the role of Au is to act as a catalyst to interact with the precursor vapor and initiate nucleation site as well as guide the growth. The horizontal quartz tube CVD chamber is initially evacuated to a pressure of 10^{-3} mbar by using a rotary pump and then filled with commercial Ar gas (99.9 %) to reach one atmospheric pressure. To observe the effect of temperature on the growth, two different growth temperatures, 950 and 1000 ^{o}C are set. The growth time is 2 h, and the flow rate of Ar is maintained at 80 sccm to achieve one atmospheric pressure. The temperature profile maintained during the growth process is given in Fig. 2.10.

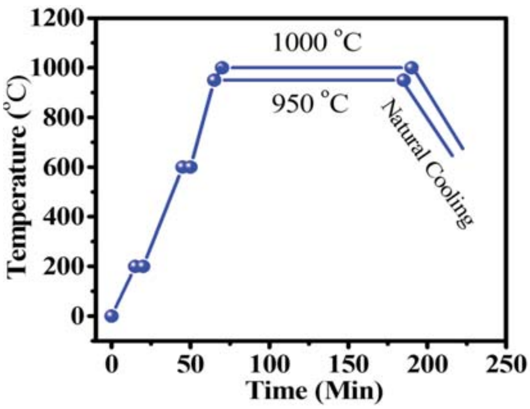

Figure 2.10 Temperature profile maintained during the growth process

The metal catalyst assisted vapor-liquid-solid (VLS) growth is one of the excellent and widespread techniques to obtain high-quality 1D NSs, especially for metal oxide 1-D NSs [11, 13, 14].In the first step of the process, the metal catalyst forms a liquid alloy droplet at high temperature and interacts with the vapor component of the precursor material.[15] It leads to the supersaturation of alloy droplets, followed by precipitation of the vapor component at the liquid-solid interfaces. Then a solid phase protruded 1-D NS is obtained. Regarding the control on the shape and size of 1-D NSs, the temperature is one of the crucial parameters which may influence the growth process drastically. A schematic is given in Fig.2.11 to describe the growth of 1-D SnO_2 NSs by the VLS mechanism.

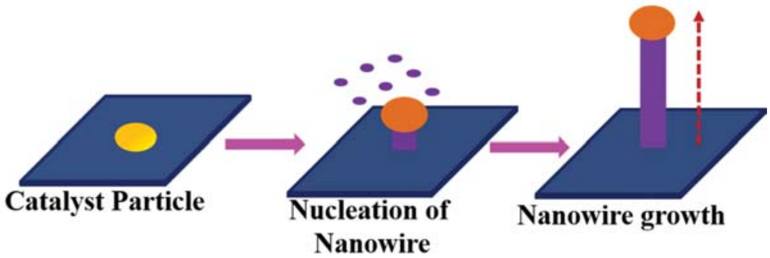

Figure 2.11 Schematic growth of vapor-liquid-solid growth.

2.2.2.1. Morphology of VLS grown 1-D SnO_2 NSs

Densely packed NWs grown at two different temperatures, 950 and 1000 ^oC are shown in FESEM images in Fig. 2.12. The inset for 950 ^oC grown sample shows a NW with a square cross-section. A dark contrast observed at the top [Circled in Fig. 2.12 (a) inset] of the NWs indicates the presence of the Au. This observation supports the catalyst based VLS model for growth. The length and width of the NWs are found to be around 100 μm and 200-250 nm, respectively.

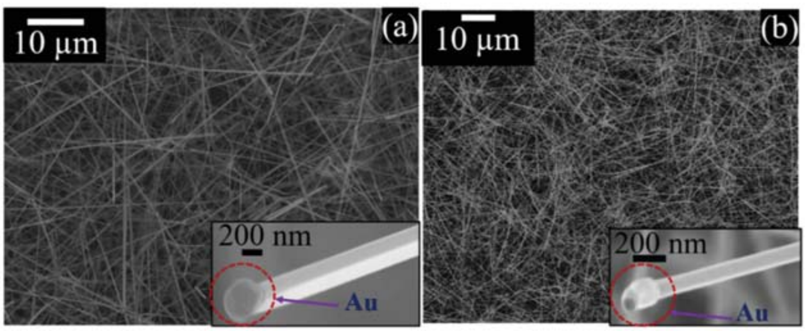

Figure 2.12 FESEM images of NWs grown at (a) 950 ^oC and (b) 1000 ^oC. Insets are high-resolution FESEM for NWs with Au droplet.

Fig. 2.12(b) shows the NWs grown at a temperature of 1000 °C. The surface appears to be smooth with Au at the top of the NW [inset Fig. 2.12 (b)]. In contrast to 950 °C grown sample, cylindrical NWs with thinner width is seen. The length and width of the cylinder-shaped NWs are calculated to be around 100 µm and 100-150 nm, respectively.

2.2.2.2. Transmission electron microscopy studies VLS grown 1-D SnO_2 NSs

Structural analysis of NWs is carried out by the TEM technique, and results are shown in Fig. 2.13. Figure 2.13 (a) shows the square-shaped NWs grown at 950 °C. The high-resolution TEM image of the single square type NWs reveals crystalline (101) plane of the rutile tetragonal SnO_2 with a *d* spacing value of 0.26 nm [Figure 2.13 (a) top inset]. The corresponding SAED pattern further demonstrates the single-crystalline nature of NWs [Figure 2.13 (b) bottom insert]. It is indexed as a [020] zone axis of the rutile SnO_2 phase.

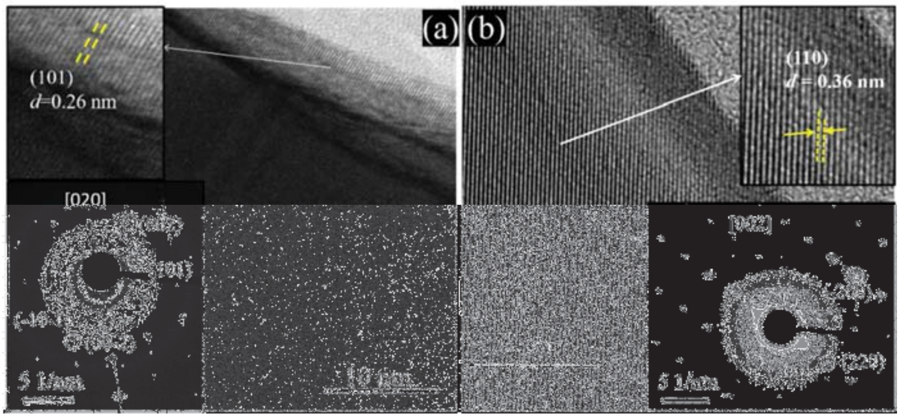

Figure 2.13 TEM image of (a) square shape NWs grown at 950 °C with [top inset (101) plane of rutile SnO_2 and bottom inset SAED pattern obtained along the [020] zone axis and (b) cylindrical shape NWs grown at 1000 °C with [top inset (110) plane of rutile SnO_2 and bottom inset SAED pattern obtained along the [002] zone axis.

Fig. 2.13 (b) shows the TEM image of a cylinder-shaped NW grown at 1000 °C. The single cylindrical NW shows a crystalline (110) plane of the rutile tetragonal SnO_2 with a *d* spacing value of 0.36 nm [Fig. 2.13 (b) top inset]. Corresponding

SAED patterns further demonstrate that NWs are single crystalline in character, which can be indexed with [002] zone axis of the rutile SnO_2 [Fig. 2.13 (b) bottom inset].

2.2.2.3. Raman spectra of VLS grown 1-D SnO_2 NSs

Raman spectroscopic measurements of NWs, grown at 950, and 1000 ^oC with laser excitation of 514.5 cm^{-1} in the back-scattering geometry are shown in Fig. 2.14.

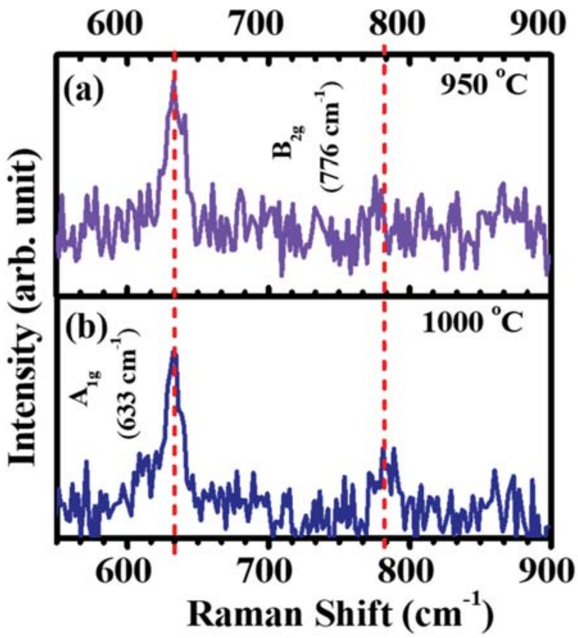

Figure 2.14 Raman spectra collected from (a) square shape and (b) cylindrical shape NWs.

Raman peaks at 633 and 776 cm^{-1}, which correspond to A_{1g} and B_{2g} symmetries of rutile tetragonal SnO_2, respectively[5].

2.2.2.4. Growth mechanism of NWs

NWs grown catalytically at two different temperatures show two different morphologies as well as growth directions. It is evident from FESEM and TEM images that the width of squares shape NWs is around 200 nm with the growth direction (101), whereas the diameter of cylindrical NWs is around 150 nm with growth direction along (110) plane. Hence width of square-shaped NWs is approximately 1.33 times bigger than the diameter of cylindrical NWs. Different sizes and shape transitions can be addressed thermodynamically by taking into consideration Gibbs free energy as a measure of structural phase transformation[15, 16]. During the VLS growth, the formation of nucleation from the saturated catalyst (Au) is an important step for the shape and structure. As reported earlier, the difference in Gibbs free energies promotes the phase transition between two competing phases at the nucleation stage itself and is found to control square and cylindrical shapes[15]. This indicates the involvement of a rectangular shape nucleus for square shape NW [Fig. 2.15 (a)] and circular shaped nucleus for cylindrical NWs [Fig. 2.15 (b)]. Based on this intuition, Gibbs free energies can be expressed for rectangular and cylindrical nucleus using equation (2.1) and (2.2), respectively[15]:

$$\Delta G_1 = -\Delta g_{v1} r_1^2 L_1 + r_1^2(\delta_1 + \delta_1^{''}) + 4 r_1 L_1 \delta_1 \qquad \textbf{2.1}$$

$$\Delta G_2 = -\Delta g_{v2} r_2{}^2 \pi r_2{}^2(\delta_2 + \delta_2^{''}) + 2\pi r_2 L_2 \delta_2 \qquad \textbf{2.2}$$

Here Δg_v is the Gibbs free energy per unit volume and quantified as RT (1,2) / V_m ln(P/Pe), and Δg_v is basically a function of growth temperature (T_1= 1223 K/ 950 ^oC, for square-shaped NWs and T_2=1273 K/ 1000 ^oC, for cylindrical shape NWs). Again, r_1 (r_2) and L_1 (L_2) are width (radius) and length of rectangular (cylindrical) shape nucleus. δ_1(δ_2) and δ_1''(δ_2'') are nucleus vapor interface energy and nucleus-liquid interface energy for rectangular (column) shaped nucleus, respectively. Optimizing Eqn. 2.1 and Eqn. 2.2, the critical radius of these two different systems can be expressed as r_1^*= 4δ1/Δgv_1 for the rectangular nucleus, whereas r_2^*=2δ1/Δgv2 is for the cylindrical nucleus. So, comparing the size of these two nuclei, gives r_1^*/r_2^* =2$\delta_1 T_2/\delta_2 T_1$. Now, depending on growth direction, δ_1 and δ_2 are found to be 1.43 and 1.20, respectively[17]. Substituting the appropriate value, it can be shown that $r_1^* = 2.48 r_2^* \approx 1.24(2 r_2^*)$.

After the formation of the nucleation, the continuous supply of precursors led to axial as well as radial growth. Kwon *et al.* have shown that axial growth is more favorable than radial growth, and the growth continues until the aspect ratio reaches its limit[18]. However, radial growth rates for rectangular and cylindrical NWs essentially are the same for both during the growth of nanostructure. In that case, the final size depends on the initial size of the nucleus. Accordingly, the width of square NWs should be around 1.24 times of the diameter of cylindrical NWs, and it matches closely with our experimental results. As the width of square NWs and the diameter of cylindrical NWs are ~200 and 150 nm, respectively.

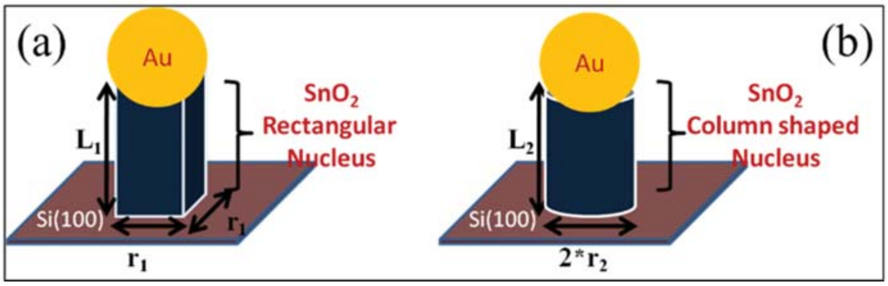

Figure 2.15 Schematic of the VLS growth mechanism for (a) Square and (b) Cylinder shaped NWs

2.2.3. Vapor-solid growth

For VS growth of 1-D NSs, mixture of the as-prepared SnO_2 QDs of size 2.4 nm and graphite powder (Alfa Aesar 99.9995%) in a weight ratio of 3:1 is placed in a high pure (99.99 %) Al_2O_3 crucible. The dimension of the crucible is 1 and 0.5 cm in the diameter and height, respectively. The crucible is placed in the Al_2O_3 boat. The horizontal quartz tube CVD chamber is initially evacuated to a pressure of 10^{-3} mbar by using a rotary pump and then filled with the commercial Ar gas. The NWs were grown for 2 h under atmospheric pressure at 1000 ^oC with 80 sccm of Ar flow rate. The NWs are grown in the crucible itself. This 1-D structure is grown without any metal catalyst.[16] Fig. 2.16 shows the temperature profile of the chamber during the growth.

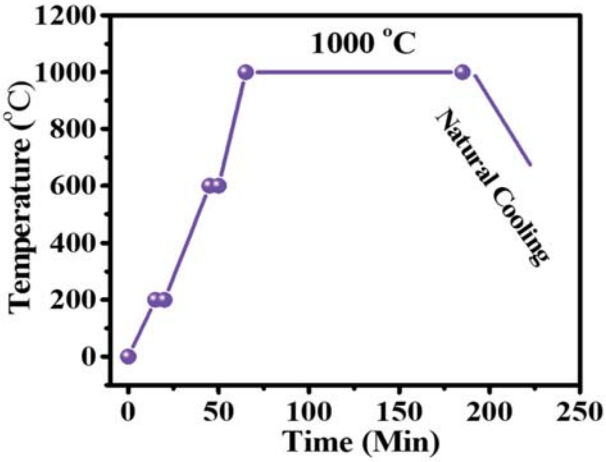

Figure 2.16 Temperature profile maintained during the growth process

2.2.3.1. Morphology of VS grown 1-D SnO_2 NSs

Fig 2.17 shows the FESEM images of VS grown SnO_2 dispersed on the Si substrate. It is found that this sample contains SnO_2 NSs of random structure [Fig. 2.17 inset bottom] along with micro-belt morphology [Fig. 2.17 inset top]. No catalysis found at the top of this nanostructure indicates the self-catalytic growth mechanism of these nanostructures.

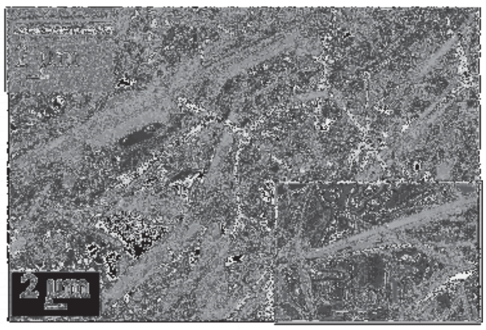

Figure 2.17 FESEM image of VS grown SnO_2. Micro belt (top inset) and beak-shape (bottom inset) NSs.

2.2.3.2. Transmission electron microscopy study of VS grown SnO_2

Fig 2.18 shows the TEM image of a nanobelt grown at 1000 °C. The HRTEM image of a single nanobelt with a crystalline (110) plane belongs to rutile tetragonal SnO_2 with a *d* spacing of 0.36 nm. The SAED pattern demonstrates a single crystalline character of nanobelt, which has a [020] zone axis.

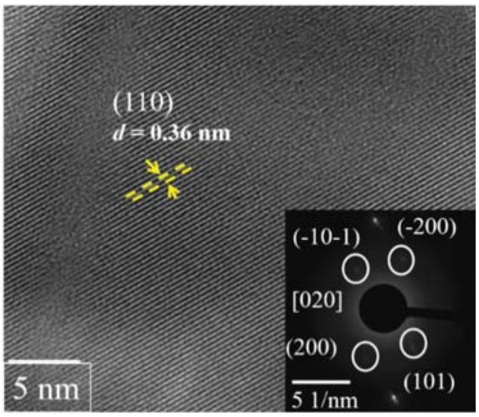

Figure 2.18 TEM images of SnO_2 micro-belt (inset) SAED pattern obtained along [020] zone axis.

2.2.3.3. Raman spectra of VS grown 1-D SnO_2 NSs

Raman spectroscopic measurement from a single μB is recorded with the laser excitation of 514.5 cm^{-1} (Fig. 2.19). Distinct A_{1g} (633 cm^{-1}) and B_{2g} (776 cm^{-1}) peaks confirm the rutile structure of SnO_2 [5].

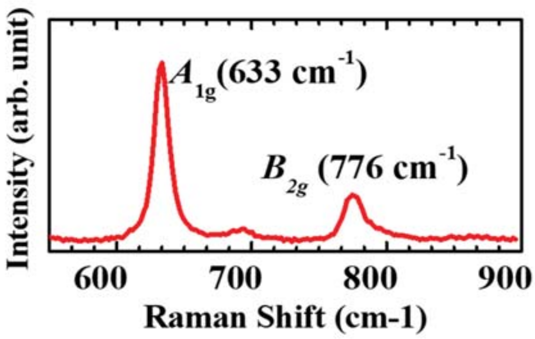

Figure 2.19 Raman spectra of a single SnO_2 micro-belt.

Thus, various 1-D nanostructures are grown by both methods, VLS and VS using the same as-prepared SnO_2. All the nanostructures reveal the rutile tetragonal phase of SnO_2.

2.3. Growth of SnO_2 NPs in GO matrix

GO, structurally similar to graphene, has various functional groups that can be tailored for beneficial applications. Here the role of the functional groups present in the GO on the growth of SnO_2 NPs is firstly highlighted. For comparative study, two different growth procedures are followed[19]:

1. For in-situ growth, GO (IMPEX, India) is initially dispersed in DI water and kept under ultra-sonication for half an hour to get a homogeneous mixture. Then, $SnCl_4$ is added under continuous stirring of the solution, followed by the addition of 2M NH_4OH dropwise. The resultant black solution is washed repeatedly with DI water to remove additional chlorine ion. The final product is then dried at 100 ^oC. This obtained sample is GO-SnO_2 (in-situ).
2. For the ex-situ sample, SnO_2 QDs are added to a dispersed GO solution in DI water, and the mixture is sonicated for half an hour. The resultant product was filtered out and kept at 100 ^oC. This sample is referred to as GO-SnO_2 (ex-situ).

A schematic presentation to elaborate on the synthesis procedures is given in Fig. 2.20:

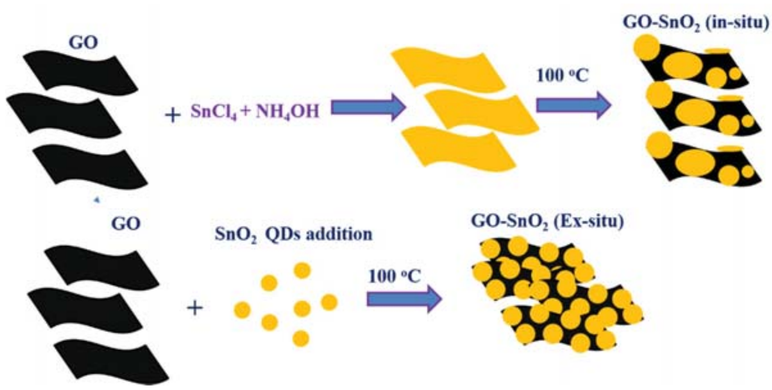

Figure 2.20 Schematic view of in-situ and ex-situ synthesized GO-SnO_2.

2.3.1.1. Morphology of GO-SnO_2 composite

Electrostatic self-assembly happens when two different colloids with opposite charges are mixed together. Herein reduction of Sn_4Cl with NH_4OH leads to the formation of $Sn(OH)_4$, which generally carries a positive charge, whereas the GO suspension possesses a negative charge due to the presence of the various functional groups.[20, 21] Hence there is a strong probability for attachment of positively charged $Sn(OH)_4$ towards the negatively charged oxygen-containing groups such as hydroxyl and epoxy groups, which are attached to both sides of a GO sheet.[22] In the case of the ex-situ sample, non-conventional interactions like Van der Waals interactions, hydrogen bonding, or π-π stacking prevail and stabilize the sample.

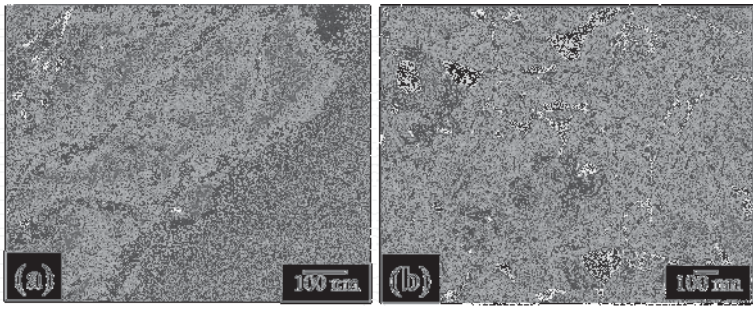

Figure 2.21 FESEM images of (a) GO-SnO_2 (in-situ) and (b) GO-SnO_2 (ex-situ)

To verify the morphological characters of both, GO-SnO_2 (in-situ) and GO-SnO_2 (ex-situ), FESEM images are recorded and shown in Fig. 2.21 (a) and (b), respectively. In both cases, SnO_2 NPs are uniformly dispersed on to the curved flaky layer of the GO sheets. This aspect confirms a close combination between GO and SnO_2 NPs. However, particle sizes cannot be detected distinctly due to limited resolution and contrast.

2.3.1.2. Transmission Electron Microscopy studies

For further structural information, a TEM study carried out for the GO-SnO_2 (in situ) sample is presented in Fig.2.22.

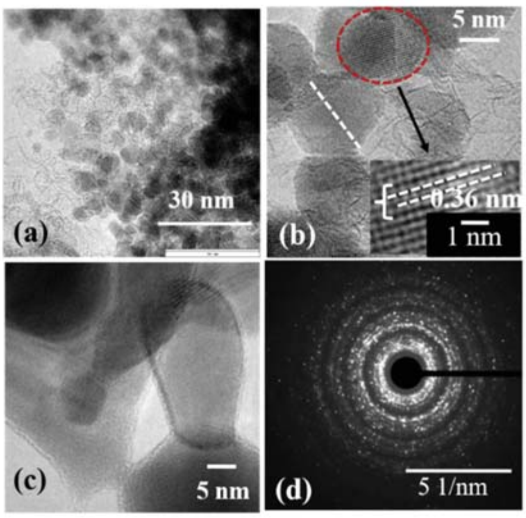

Figure 2.22 (a), (b), (c) Irregular shaped TEM images of SnO_2 nanoparticles in GO matrix. (d) SAED patterns of SnO_2 collected from SnO_2 NPs.

Fig.2.22 (a) displays the dispersion of spherical NPs of varied sizes. For instance, Fig.2.22 (b) highlights the particle size of 10 nm ± 2 in the GO matrix, which is much bigger than the as-prepared SnO_2 QDs of 2.4 nm, as shown in the previous section. A lattice spacing of 0.36 nm shown as an inset in Fig.2.22 (b) corresponds to (110) plane of the rutile SnO_2 crystal. In addition to a spherical shape, irregular shaped NPs are also spotted [Fig 2.22 (c)]. Earlier works with Fe_2O_3 and GO, followed by thermal annealing to reduce GO into rGO, have demonstrated the formation of irregularly shaped metal oxide. The post-annealing after the growth was discussed as a reason behind the irregular shaped NPs. In the current study, the growth of SnO_2 metal oxide is drastically affected without any heat treatment but by the presence of GO. It can be presumed that GO provides a heterogeneous nucleation site for the growth of metal oxide, whereas the functional groups found on the basal plane as well as edge act as anchoring sites[19]. Further, SnO_2 is not aggregated, and the embedded NPs prevents the restacking of multilayers. SAED pattern displays [Fig. 2.22 (d) spotty ring pattern indicating an improved crystalline structure compared to SnO_2 QDs. However, blurred rings indicate the possible presence of a short-range ordering in NPs.

2.3.1.3. Vibrational spectroscopy of GO-SnO_2 composite

Raman spectroscopy offers structural information as well as defect related information. It is employed to understand the typical role of GO in the growth process of SnO_2 and their interaction. Raman spectra are collected from both GO-SnO_2 (in-situ), and GO-SnO_2 (ex-situ) samples and are shown in Fig.2.23 (a). A broad peak at 573 cm^{-1}(*S*) is seen for the as-prepared sample [Fig.2.23 (b)]. This is similar to the Raman spectra of SnO_2 QDs.[1, 23, 24] This broad peak arises due to the non-stoichiometric layer of the ultra-small NP. The absence of other Raman allowed modes indicates a low crystalline phase of SnO_2 NPs. In contrast, the in-situ sample has shown the Raman allowed A_{1g} mode at 626 cm^{-1} [Fig.2.23 (b)]. This mode is never seen for the as-prepared SnO_2, however, seen for the bigger crystalline SnO_2 NPs. Thus, 626 cm^{-1} peak is a signature for the formation of a large crystalline SnO_2 particle in the presence of GO, as supported by TEM results shown in Fig. 2.23.

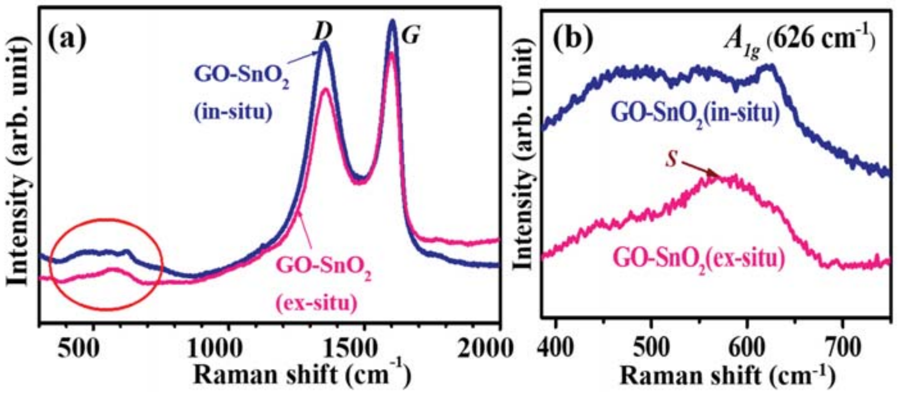

Figure 2.23 Raman spectra of (a) GO-SnO_2 composite and (b) SnO_2 portion in the composite

In addition, graphene-related peaks at 1355 cm^{-1} (*D*) and 1598 cm^{-1}(*G*) are also found for both in-situ and ex-situ samples [Fig. 2.23 (a)][23, 24] Generally, the *D* mode appears due to the breathing mode of the *k*-point phonon of A_{1g} symmetry. In contrast, G mode is due to the1st order scattering of the E_{2g} phonon of the C atom. The intensity ratios (I_D/I_G) of D and G peaks of the in-situ GO-SnO_2 and ex-situ GO-SnO_2 estimated after deconvoluting the spectra [Fig. 2.24 (a) and (b)] are found to be 1.07 and 1.02, respectively. Thus, the in-situ sample displays a higher amount of defects component. Notably, Wang *et al.* deduced the same ratio for GO, rGO, and SnO_2-rGO samples and reported it to be 0.85,0.80 and 1.12, respectively[22]. They correlated the increased I_D/I_G value of SnO_2-rGO to the defects created by the introduction of SnO_2 to the GO matrix. Moreover, an enhanced I_D/I_G ratio for the Fe_3O_4-rGO system (1.02) relative to GO (0.94) was also reported. They ascribed it to the increased disorders in the GO matrix due to the loading of Fe_2O_3 [25]. Considering the above observations, the enhanced intensity of the A_{1g} band reflects improved intercalation of SnO_2 NPs in the GO sheets during the in-situ growth.

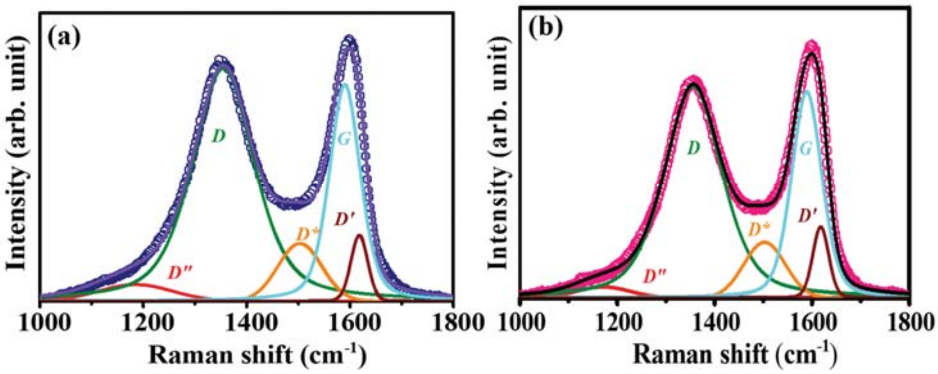

Figure 2.24 Deconvoluted Raman spectra of (a) GO-SnO_2 (in-situ) and (b) GO-SnO_2 (ex-situ)

Vibrational spectroscopy like FTIR provides rich information on metal oxide, functional groups of GO, and their interactions. In the present study, the growth procedure of SnO_2 is different for the ex-situ, and the in-situ samples and accordingly prevailed interactions with GO matrix appear to be different. For the ex-situ procedure, the as-prepared SnO_2 acts mainly as a spacer between GO sheets, and in turn, the NPs prevent the GO sheets from the collapse. In contrast, a reaction occurs for the in-situ procedure between $SnCl_4$ and NH_4OH in the presence of oxygenated moieties of GO. The growth procedure follows the anchoring of Sn^{4+} precursor selectively with functional groups of the graphene layer, as explained in reference[26]. In the process, a partial decrease of functional groups of GO due to an attachment to a metal oxide intermediate $Sn(OH)_4$ could occur. FTIR measurements are done to understand such attachment and interaction of NPs with various groups of GO, and the obtained spectra are shown in Fig. 2.25.

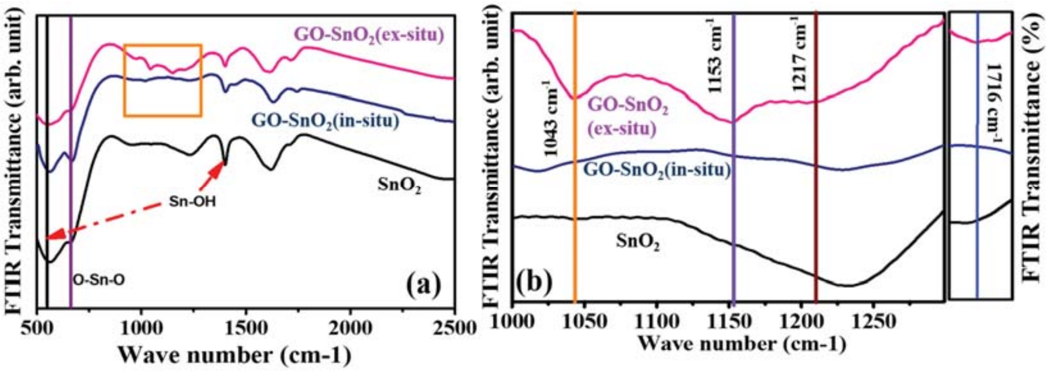

Figure 2.25 (a) FTIR spectra of SnO_2 and GO-SnO_2 composites (b) highlighting presence/ absence of functional groups in the ex-situ and the in-situ GO-SnO_2 composites.

Characteristic vibration peaks related to SnO_2 NPs as well as GO are clearly observed for both in-situ and ex-situ samples. Peak at 670 cm^{-1} corresponds to O-Sn-O vibrations of SnO_2.[27, 28] A stronger intensity with less FWHM at 670 cm^{-1} is recorded for the in-situ sample than the same for the ex-situ sample. The stronger intensity is an indication of the improved crystalline phase of SnO_2 NPs. The peaks in Fig. 2.25 (a) at 560 and 1630 cm^{-1} are assigned to vibrational modes of Sn-OH. Other modes observed at 1043, 1154,1224, and 1716 cm^{-1} for the ex-situ sample are assigned to –C-O (epoxy), -C-OH (Hydroxyl), -C-O (Stretching vibration of carbonyl), and –C=O (stretching vibration of carbonyl and carboxyl) group attached to GO [Fig. 2.26 (b)][22, 25].It is important to note that these peaks (1045, 1154, 1224, and 1716 cm^{-1}) show decreased intensities for the in-situ sample [Fig. 2.25 (b)]. A similar observation is also reported for the synthesis of metal/metal oxide-rGO composite. However, functional group related information prior to the formation of rGO by thermal or chemical treatment is limited in the literature[21, 22]. For example, Wang *et al.* discussed the FTIR spectra of the composite resulted from the addition of Sn $(OH)_4$ to the GO solution followed by annealing at 500 ^oC[22]. They observed the absence of 1732 and 1224 cm^{-1} modes in the resulted rGO from the GO. In another report on the rGO-Fe_2O_3 composite, the absence of carboxyl group and epoxies group at 1723 and 1093 cm^{-1}, respectively, in the reduced GO was also discussed, however, without detailing the same for the $Fe(OH)_3$-GO intermediate prior to the formation of rGO-Fe_2O_3 by thermal treatment[25]. Hence, the role of functional groups attached to GO that anchored the NPs was not sufficiently specified. However, participation and reduction of these functional groups in GO-SnO_2 composite (in-situ) are clearly observed in the current study, which indicates that $Sn(OH)_4$ interacts with functional groups of GO during the synthesis of SnO_2. Subsequently, the deposition of SnO_2 takes place on the GO surfaces. A schematic representation of possible pathways for different interactions among the functional groups and $Sn(OH)_4$ is depicted in Fig.2.26. This also explains possible breaking and rearrangement of epoxy, hydroxyl, and carbonyl groups after participation in interaction with metal oxide precursor, $Sn(OH)_4$. The formation of the bond, as shown in Fig. 2.26, can initiate an immobilized nucleation center, which further acts for the growth process to give rise to a large nanoparticles [19]. Such a bond fixation-based nucleation center is not possible in the synthesis of only metal oxide NPs. In fact, this process resembles a heterogeneous nucleation system which offers low energy barrier for nucleation and growth of NPs [29]. Thus, there are energetically enhanced chances for the creation of a large number of nucleation sites in close proximity, and subsequently, their participations allow creating a bigger NP than the as-prepared SnO_2 NP. Therefore, the growth of NPs is found to be dependent on the GO surfaces.

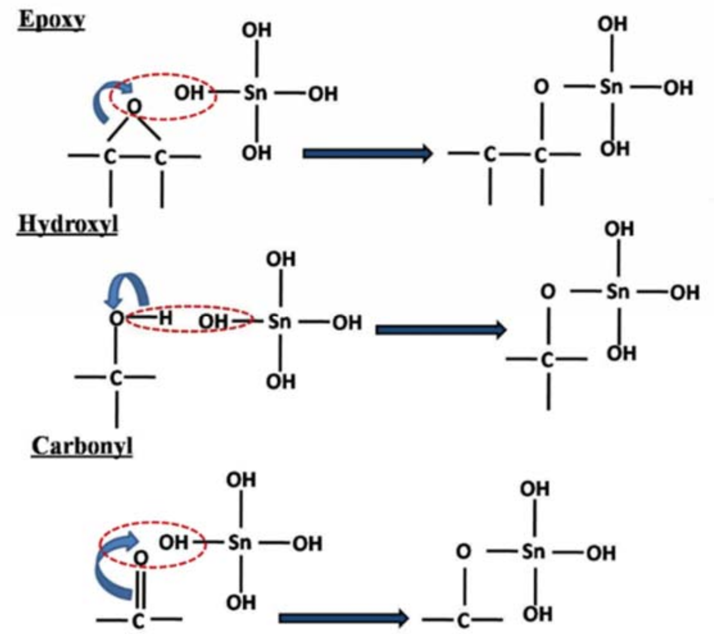

Figure 2.26 Schematic representation of possible reaction pathways for functional groups of GO during the formation of nucleation for SnO_2 NPs.

2.3.1.4. Growth mechanism of SnO_2 NPs in GO matrix

Based on the findings from the FTIR study on the typical role of epoxy, hydroxyl, and carbonyl groups and TEM and Raman investigations elaborating morphological information like the variation in size and irregular shape of SnO_2 for the in-situ sample, a schematic illustration on the growth mechanism of GO-SnO_2 is shown in Fig.2.27. It shows that the presence of a functional group for the in-situ sample, brings metal oxide nuclei in closer proximity to result in the bigger and irregular shaped NPs. In contrast, different functional groups remain unaffected in the case of the ex-situ sample with smaller SnO_2 NPs.

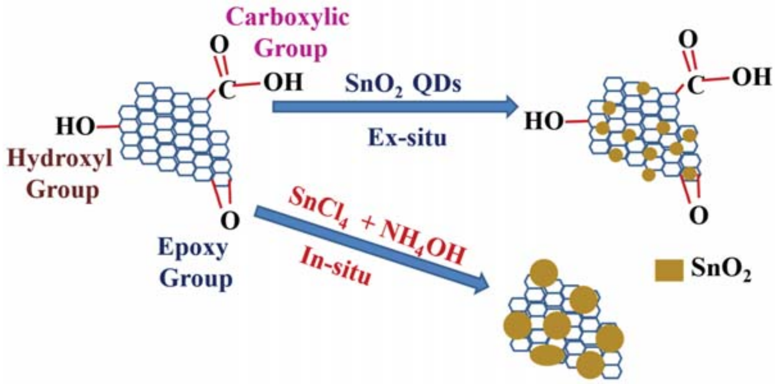

Figure 2.27 Schematic representation of decoration of SnO_2 NPs on the surface of GO sheet by both ex-situ and in-situ process of synthesis.

2.4. Summary

Using a soft-chemical growth technique, SnO_2 QDs are synthesized. Subsequent annealing of these QDs results in bigger particles with improved crystallinity. This observation is verified with shreds of evidence provided by XRD, FESEM, and TEM measurements. Spectroscopic measurements like Raman and FTIR further support the formation of the SnO_2 phase. The broad peak in the Raman spectra at 573 cm^{-1} for the smaller particles (2.4 and 4.2 nm) indicates the presence of defects and a non-stoichiometric layer. Further VLS and VS growth processes are used to grow NWs and μB, respectively. The typical effect of temperature on morphology is observed, such as lower temperature VLS growth favors square-shaped NWs than the cylindrical-shaped NWs grown at a higher temperature. At the same time, the VS grown samples demonstrate random structure, including μB. The growth of SnO_2 NPs in the presence of GO reveals the important role of functional groups of GO on the growth of bigger SnO_2 NPs than the ex-situ grown NPs.

2.5. References

[1] B.K. Sahu, A. Das, Significance of in-plane oxygen vacancy rich non-stoichiometric layer towards unusual high dielectric constant in nano-structured SnO_2, Physica E: Low-dimensional Systems and Nanostructures, (2018).
[2] A. Das, V. Bonu, A.K. Prasad, D. Panda, S. Dhara, A.K. Tyagi, The role of SnO_2 quantum dots in improved CH_4 sensing at low temperature, Journal of Materials Chemistry C, 2 (2014) 164-171.
[3] B.D. Cullity, Elements of X-ray diffraction, Addison-Wesley Pub. Co., Reading, Mass., 1956.
[4] A. Kar, S. Kundu, A. Patra, Surface defect-related luminescence properties of SnO_2 nanorods and nanoparticles, The Journal of Physical Chemistry C, 115 (2010) 118-124.

[5] A. Dieguez, A. Romano-Rodrıguez, A. Vila, J. Morante, The complete Raman spectrum of nanometric SnO_2 particles, Journal of Applied Physics, 90 (2001) 1550-1557.
[6] L.P. Ravaro, L.V. Scalvi, A.S. Tabata, F.M. Pontes, J.B. Oliveira, Nanoparticle characterization of Er-doped SnO_2 pellets obtained with different pH of colloidal suspension, Journal of Applied Physics, 114 (2013) 084304.
[7] B. Cojocaru, D. Avram, V. Kessler, V. Parvulescu, G. Seisenbaeva, C. Tiseanu, Nanoscale insights into doping behavior, particle size and surface effects in trivalent metal doped SnO_2, Scientific Reports, 7 (2017) 9598.
[8] A. Biaggi-Labiosa, F. Sola, M. Lebrón-Colón, L. Evans, J. Xu, G. Hunter, G. Berger, J. Gonzalez, A novel methane sensor based on porous SnO_2 nanorods: room temperature to high temperature detection, Nanotechnology, 23 (2012) 455501.
[9] V. Bonu, A. Das, S. Amirthapandian, S. Dhara, A.K. Tyagi, Photoluminescence of oxygen vacancies and hydroxyl group surface functionalized SnO_2 nanoparticles, Physical Chemistry Chemical Physics, 17 (2015) 9794-9801.
[10] V. Bonu, B.K. Sahu, A. Das, S. Amirthapandian, S. Dhara, H.C. Barshilia, Sub-wavelength waveguide properties of 1D and surface-functionalized SnO_2 nanostructures of various morphologies, Beilstein journal of nanotechnology, 10 (2019) 379-388.
[11] R. Wagner, W. Ellis, Vapor-liquid-solid mechanism of single crystal growth, Applied physics letters, 4 (1964) 89-90.
[12] S. Luo, J. Fan, W. Liu, M. Zhang, Z. Song, C. Lin, X. Wu, P.K. Chu, Synthesis and low-temperature photoluminescence properties of SnO_2 nanowires and nanobelts, Nanotechnology, 17 (2006) 1695.
[13] H. Anzai, M. Suzuki, K. Nagashima, M. Kanai, Z. Zhu, Y. He, M. Boudot, G. Zhang, T. Takahashi, K. Kanemoto, True vapor–liquid–solid process suppresses unintentional carrier doping of single crystalline metal oxide nanowires, Nano letters, 17 (2017) 4698-4705.
[14] Z. Zhu, M. Suzuki, K. Nagashima, H. Yoshida, M. Kanai, G. Meng, H. Anzai, F. Zhuge, Y. He, M.l. Boudot, Rational concept for reducing growth temperature in vapor–liquid–solid Process of metal oxide nanowires, Nano letters, 16 (2016) 7495-7502.
[15] B. Wang, Y. Yang, N. Xu, G. Yang, Mechanisms of size-dependent shape evolution of one-dimensional nanostructure growth, Physical Review B, 74 (2006) 235305.
[16] B. Wang, Y. Yang, C. Wang, G. Yang, Nanostructures and self-catalyzed growth of SnO_2, Journal of Applied Physics, 98 (2005) 073520.
[17] A. Beltran, J. Andrés, E. Longo, E. Leite, Thermodynamic argument about SnO_2 nanoribbon growth, Applied physics letters, 83 (2003) 635-637.
[18] S.J. Kwon, Theoretical analysis of non-catalytic growth of nanorods on a substrate, The Journal of Physical Chemistry B, 110 (2006) 3876-3882.
[19] B.K. Sahu, A. Das, Graphene oxide surface chemistry regulated growth of SnO_2 nanoparticles for electrochemical application, Journal of Alloys and Compounds, (2020) 154901.
[20] J. Ding, B. Li, Y. Liu, X. Yan, S. Zeng, X. Zhang, L. Hou, Q. Cai, J. Zhang, Fabrication of Fe_3O_4@ reduced graphene oxide composite via novel colloid electrostatic self-assembly process for removal of contaminants from water, Journal of Materials Chemistry A, 3 (2015) 832-839.
[21] F.-A. He, J.-T. Fan, F. Song, L.-M. Zhang, H.L.-W. Chan, Fabrication of hybrids based on graphene and metal nanoparticles by in situ and self-assembled methods, Nanoscale, 3 (2011) 1182-1188.
[22] Y. Wang, Y. Liu, J. Zhang, Colloid electrostatic self-assembly synthesis of SnO_2/graphene nanocomposite for supercapacitors, Journal of Nanoparticle Research, 17 (2015) 420.
[23] A.C. Ferrari, D.M. Basko, Raman spectroscopy as a versatile tool for studying the properties of graphene, Nature nanotechnology, 8 (2013) 235.
[24] S. Claramunt, A. Varea, D. López-Díaz, M.M. Velázquez, A. Cornet, A. Cirera, The importance of interbands on the interpretation of the Raman spectrum of graphene oxide, The Journal of Physical Chemistry C, 119 (2015) 10123-10129.
[25] S. Majumder, M. Sardar, B. Satpati, S. Kumar, S. Banerjee, Magnetization Enhancement of Fe3O4 by Attaching onto Graphene Oxide: An Interfacial Effect, The Journal of Physical Chemistry C, 122 (2018) 21356-21365.

[26] M. Mishra, A.P. Singh, B.P. Singh, S. Dhawan, Performance of a nanoarchitectured tin oxide@ reduced graphene oxide composite as a shield against electromagnetic polluting radiation, RSC Advances, 4 (2014) 25904-25911.
[27] Y. Wang, J. Ding, Y. Liu, Y. Liu, Q. Cai, J. Zhang, SnO_2@ reduced graphene oxide composite for high performance lithium-ion battery, Ceramics International, 41 (2015) 15145-15152.
[28] E.-S.M. Duraia, S. Das, G.W. Beall, Humic acid nanosheets decorated by tin oxide nanoparticles and there humidity sensing behavior, Sensors and Actuators B: Chemical, 280 (2019) 210-218.
[29] N.T. Thanh, N. Maclean, S. Mahiddine, Mechanisms of nucleation and growth of nanoparticles in solution, Chemical reviews, 114 (2014) 7610-7630.

Chapter 3

SERS and unlikely phonon modes in SnO_2 NPs

Raman spectra of nanostructures carry important structural information, including the disorder and surface defects related modes[1-4]. In general, the Raman signals are weak, and it becomes difficult to identify the disorder and surface-related modes in conventional Raman measurements[5]. This chapter focuses on the use of the SERS for exploring the underneath structural information of SnO_2 nanomaterials. SERS is known for ultrasensitive trace detection[6, 7]. In SERS measurement, strong enhancement of the weak Raman signal of an analyte molecule absorbed on the plasmonic metal or metallic NSs takes place[8-10]. Importantly, a highly localized surface plasmon resonance in the NSs of plasmonic metal like Ag and Au with suitable electromagnetic irradiation occurs to enhance the Raman signal[9, 11]. Along these lines, the SERS study is carried out to observe Raman allowed mode from the as-prepared QDs, which otherwise does not show any Raman allowed modes but show a broad Raman forbidden mode[4, 7, 12]. The electromagnetic irradiation on the metal surfaces results in a strong electric field in the vicinity of the plasmonic metal[13]. Thus, away from the metal surface, a high electric field gradient is realized in the localized region[14, 15]. Due to this strong electric field gradient, an analyte molecule near the metal surface experiences an inhomogeneous electric field. Importantly, such an inhomogeneous field is reported to influence the vibration property of the analyte[15, 16]. The effect of a similar field on the vibrational properties is considered for investigation with SnO_2 NPs in the presence of an efficient plasmonic substrate. Prior to performing SERS studies, two plasmonic materials, such as Au and Ag nanomaterials, are prepared and optimized to provide high electric field confinement during the SERS experiment. A seed-mediated growth is adopted for the synthesis of Au NRs, whereas Ag nanoparticles are synthesized without any capping agent to form network structures. The SERS efficiencies of both plasmonic structures are carried out with rhodamine 6G (R6G). Finally, the SERS substrate with higher efficiency is utilized to investigate the effect of a strong inhomogeneous electric field on the vibrational property of SnO_2 NPs.

3.1. Optimization of SERS substrate

3.1.1. Synthesis of Au NRs

Au NRs, one of the efficient choices as SERS substrate due to its chemical stability and superior optical property[17], are synthesized by a seed-mediated method[18, 19]. As a first step of the synthesis procedure, cetrimonium bromide (CTAB) protected Au seeds are prepared from ice-cold $NaBH_4$ solution (600 µl, 0.01 M) and Au precursor (250 µl, 0.01 M) in CTAB solution (10 ml, 0.1 M). The solution is kept undisturbed for 2 h for the growth of uniform Au seeds. In another pot, a growth solution is prepared by the addition of 250 µl of Au precursor in a 12 ml CTAB solution followed by the addition of 20 µl $AgNO_3$. Then 70 µl of ascorbic acid is added dropwise. Finally, an optimum 60 µl of seed is poured into the growth solution to initiate the growth of Au NRs[19]. The solution is incubated at room temperature for 5 h to continue the growth of the rods.

3.1.2. Optical characterization of Au NRs

UV-Visible spectrum is collected for the Au NRs solution using UV-Visible spectrometer (AVANTES) in absorbance mode and is depicted in Figure. 3.1.

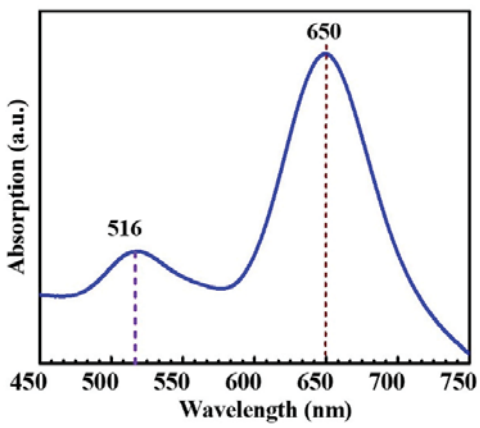

Figure 3.1 UV-Visible spectrum of Au NRs with LSPR at 650 nm.

Two distinct absorption peaks observed at 516 and 650 nm are ascribed to transverse and longitudinal surface plasmonic resonance (T/LSPR) peaks, respectively[20, 21]. Because of the presence of an easily tunable LSPR peak, Au NRs are the subject of extensive research.

3.1.3. Morphological characterization of Au NRs

To investigate the morphology of the prepared Au NRs, FESEM study is performed, and the typical micrograph is shown in Fig. 3.2.

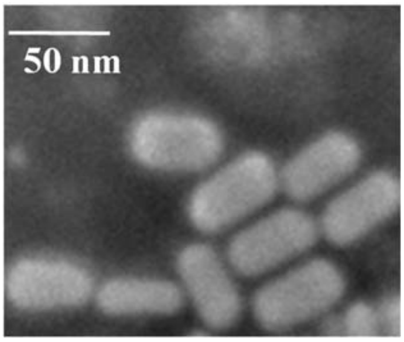

Figure 3.2 FESEM micrograph of Au NRs.

FESEM image of Au NRs indicates the formation of cylindrical NRs with a hemispherical end. The average aspect ratio of Au NRs is calculated to be 2.1±0.2. In an aqueous solution SPR absorption maximum (λ_{max}) is correlated by (λ_{max}= 95 AR+ 420)[22]. AR corresponding to the LSPR wavelength 650 nm is calculated to 2.4, and they tally closely with the experimental data.

3.1.4. Synthesis of Ag nanonets

For the synthesis of Ag nanonet, 6 ml of 10 mM ice-cold aqueous $NaBH_4$ solution is added dropwise to 30 ml of 0.25 mM $AgNO_3$ solution. The color of the solution turns slowly from a pale yellow to orange-yellow and then to a reddish orange. After incubation for 30 min, lighter particles aggregating on top of the solution are collected on Si substrates by dip coating. These flaky structures on the Si substrates are found to be stable with a size of 1-2 mm and are used for further characterization along with SERS experiments.

3.1.5. Optical characterization of Ag nanonet

The absorption spectrum is collected from the Ag nanonets on the Si substrate in a reflection mode and is shown in Fig. 3.3. A broad SPR peak related to Ag is observed around 375 nm[11].

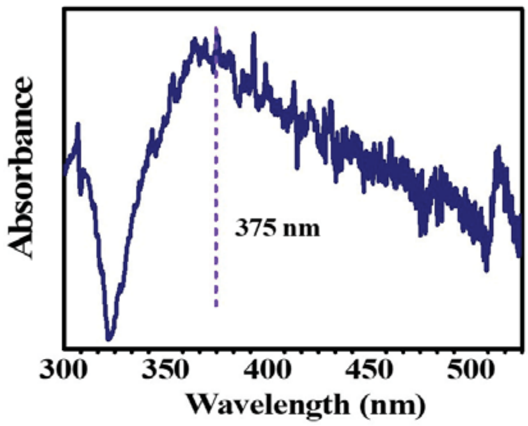

Figure 3.3 UV-Vis spectrum of Ag nanonets on Si substrate.

3.1.6. Morphological characterization of Ag Nanonet

FESEM microstructure of Ag nanonets is depicted in Fig. 3.4. The image shows the formation of a network structure on the substrates due to the random aggregation of Ag NPs. The inset represents the chain of Ag NPs of ~ 50 nm. The presence of nano-crevices is seen at the joints of Ag nanoparticles [Fig.3.4 inset]. The formation of such a structure acts as a hotspot for confining the electric field[23, 24] and can act as excellent sites for SERS enhancements.

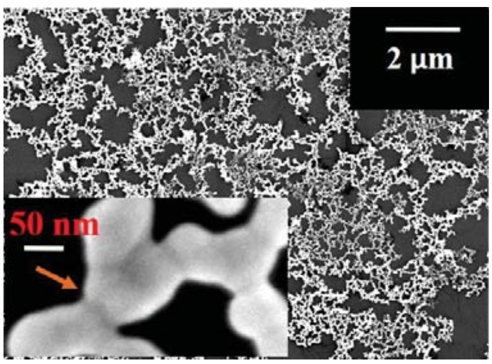

Figure 3.4 FESEM image of Ag nanonets with nano crevices (inset).

3.1.7. Comparing the efficiency of Au NRs and Ag nanonets as SERS substrates

SERS is a non-destructive technique to trace a very low concentration of the analyte. This enhancement arises because of the confinement of the electromagnetic field on the metal surface owing to the plasmonic property[25, 26]. The confined light enhances the Raman signal by (a) local field enhancement and (b) radiation enhancement[5]. Because of the combined effect, a huge enhancement in the Raman signal is possible, and an electromagnetic field induced enhancement (EF_{EM}) is represented as in Eqn. 3.1[27]:

$$EF_{EM}(\omega_{0,}\omega_{R,}r_m) \approx \left|\frac{E_{Local}(\omega_{0,}r_m)}{E_0(\omega_{0,}r_m)}\right|^4 \qquad \textbf{3.1}$$

The equation is well known as the E^4 approximation for the EF_{EM} of SERS[27, 28]. However, the finest enhancement is dependent on various parameters such as plasmonic position, the morphology of plasmonic materials, the bonding nature of analytes with metals, and so on. Firstly, for the SERS measurement purpose, Au NRs solution is dropped cast on a Si substrate and dried with IR light. Similarly, Ag nanonets collected on the Si substrate is utilized as a SERS substrate. Different concentrations of R6G are drop casted on the SERS substrates, and the Raman spectra are collected. The results are shown for Au NRs in Fig.3.5(a) and for Ag nanonets in Fig.3.5(b).

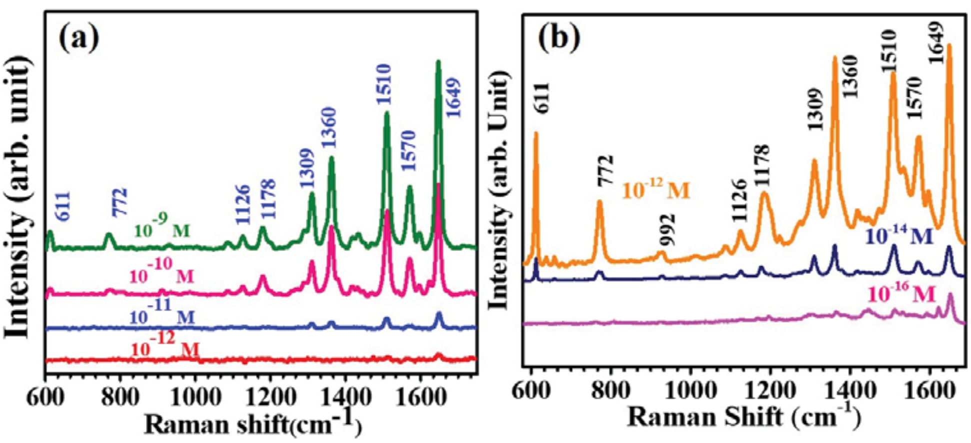

Figure 3.5 SERS collected from the different concentrations of R6G in the presence of (a) Au NRs and (b) Ag nanonets.

Vibrational frequencies of R6G at 611,772,1126,1178,1309,1360,1510,1570 and 649 cm^{-1} are observed[28, 29]. Importantly, the lowest concentrations of R6G detected are up to 10^{-12} M and 10^{-16} M by Au NRs and Ag nanonets, respectively. This result indicates the better efficiency of Ag nanonet as a SERS substrate than the Au NRs. Moreover, the blinking effect is observed with Ag nanonets for 10^{-16} M of R6G and is shown in Fig. 3.6. The blinking behavior conjectures the variation in the intensity of R6G peak. The blinking mode due to the variation of Raman intensity with time indicates the possible effect of variation in configurations of a single molecule[30]. Generally, such a blinking effect is related to single-molecule trace detection[31]. Therefore, its observation infers efficient electric field confinement upon irradiation with an electromagnetic wave.

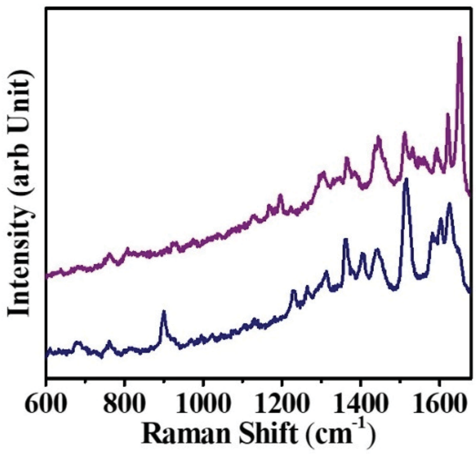

Figure 3.6 Variation of the Raman intensity with time indicating the blinking effect of R6G molecule.

Finally, because of superior Ag nanonet based SERS substate is chosen for further study to explore the phonon mode in SnO_2 NPs.

3.2. Vibrational property of SnO_2 NPs and influence of SERS substrate

3.2.1. Vibrational spectra of SnO_2 NPs

The detailed synthesis and characterization of SnO_2 NPs are described in Chapter-2. In the current chapter, the vibrational property is further discussed in detail. As prepared SnO_2 QDs, A (100 °C) and annealed NPs at 800 °C, D (800 °C) are subjected to detailed studies using SERS substrates. Vibrational spectra collected from Raman and IR measurements for A (100 ºC) and D (800 ºC) samples are depicted in Fig. 3.7.

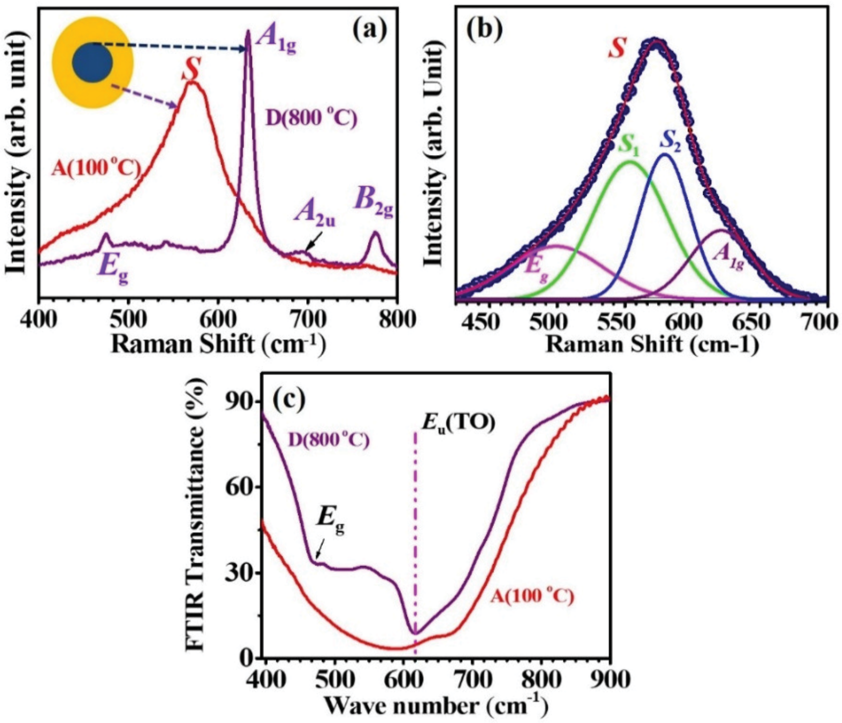

Figure 3.7 (a) Raman spectra of SnO_2 NPs, (b) deconvoluted Raman spectrum of A (100 ºC) (c) FTIR spectra of SnO_2 NPs.

The prominent Raman allowed modes, A_{1g}, E_g, and B_{2g} at 633, 475, and 774 cm^{-1}, respectively, are clearly visible for sample D(800 ºC) [Fig.3.7 (a)][32]. Along with the Raman allowed modes, it also possesses an intense IR active mode at 694 cm^{-1}, which is due to the A_{2u} (LO) mode of vibration [Fig.3.7 (a)][4]. The centrosymmetric SnO_2 crystal forbids IR active modes to appear in the Raman spectrum due to the mutual exclusion principle[33]. Hence, the presence of A_{2u} (LO) indicates symmetry breaking due to finite size. However, except for the A_{2u} (LO), other IR allowed modes are not visible during the Raman measurement. This may be due to limited local change restricting the influence on other IR modes and hence a non-significant intensity for other modes [34, 35]. It is to be noted that conventional Raman spectroscopy is a weak scattering phenomenon. Furthermore, the IR spectrum of D (800 ºC) displayed in Fig. 3.7(c) shows the presence of a Raman allowed E_g mode at 475 cm^{-1} along with the IR active mode from Eu (TO). This observation also supports the possible breaking of the mutual exclusion principle in the case of D (800 ^{o}C).

In contrast, to sample D, the as-prepared QDs [A (100 ^{o}C)] possesses a broad Raman band around 573 cm^{-1} [Fig.3.7(a)] referred as *S* peak. This band is linked to defects and a non-stoichiometric layer of few nanometer thicknesses around a relatively crystalline core of SnO_2 [Fig.3.7(a) inset][1, 36]. This highly disordered layer, in comparison to the core structure, owes its origin to mainly surface O_V[37]. The broadband is convoluted into two Raman allowed modes (E_g and A_{1g}) and two defect-related modes (S_1 and S_2). It is worth noticing that the A_{1g} peak position is decided by deconvolution with the intuition that it supposedly shifts to a lower frequency[36]. This shift arises due to a smaller dimension effect, and thus the exact position remains guesswork so far. Thus, a definite observation of the peak is required to understand the finite size effect and the change in bond constant of the QDs SnO_2. However, the scope is still open. The advancement of the Raman technique with SERS measurements providing an improved intensity may be helpful in deciphering on the peak position. Earlier Liu *et al.* have correlated the presence of *S* peak with V_P for the pulsed laser deposited 10 nm SnO_2 nanocrystals[37]. Furthermore, the V_P in the non-stoichiometric layer modifies the local symmetry to avoid the in-phase vibration, and thus it affects the intensity of an active phonon in the Raman spectrum. Raman studies, therefore, provide crucial evidence for the presence of surface O_V, more specifically about the V_P in the as-prepared SnO_2[1]. Hence the crystalline core being too small to provide the Raman allowed vibration, as it is hidden under the broad *S* peak. Thus, the SERS field needs reaching to the hidden core to reveal details.

3.2.2. Analysis of SnO_2 NP (25 nm) vibrational modes in the presence of Ag nanonet

Sample D (800 ^{o}C) with particle size ~ 25 nm are dispersed on Ag nanonets for collecting the Raman spectra (Fig. 3.8).

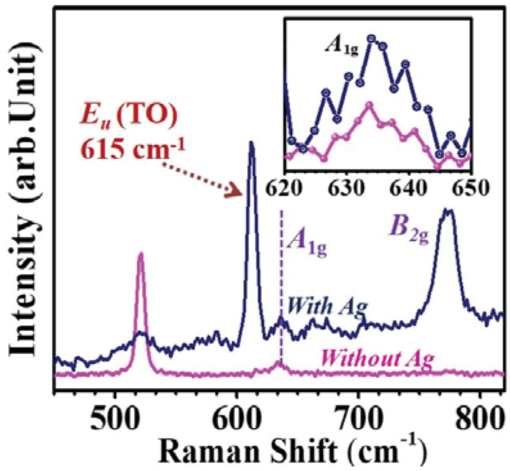

Figure 3.8 Raman spectra of sample D (800 ^{o}C) with and without Ag nanonets.

The A_{1g} peak with very low intensity is observed at 633 cm^{-1} without Ag nanonets, as shown in Figure 3.8. However, because of the small amount of material with low laser power, the B_{2g} peak is not seen clearly. Relatively high-intensity of A_{1g} peak (inset Fig. 3.8) is observed in the presence of Ag nanonets along with a huge enhancement of B_{2g} mode. A similar enhanced response of the B_{2g} mode of SnO_2 crystal in the presence of Ag colloids was reported[2]. Apart from that, a highly intense peak at 615 cm^{-1} is observed, and it is of high significance as it is not an allowed Raman mode. Notably, the E_u(TO), an IR mode, is predicted in the same position as shown in Fig.3.7(c)[35, 36]. Hence the observation of an intense IR peak in the Raman spectrum obviously indicates a breaking-down of the mutual exclusion principle, which forbids the IR active peak to be present as a Raman mode for a centrosymmetric molecule like SnO_2. Importantly, such a feature is observed solely in the presence of Ag nanonet, and thus the strong plasmonic field of it becomes a critical factor to consider. The strong field enhancement is already demonstrated as a SERS substrate for trace level detection of R6G molecule and blinking effect. Breaking of symmetry in organic molecules due to the presence of plasmonic materials was highlighted earlier[15]. For instance, 2,2'-diamino-dimercaptoazobenzene (2,2' DA-DMAB) was tested under varied electromagnetic gradient during the high vacuum tip-enhanced Raman spectroscopy (TERS) experiment[15]. In this study, IR active mode is observed during the Raman measurement, and interestingly relative intensity of an IR peak with respect to Raman peak was found to increase with the enhanced field gradient. Experimentally the variation in the field gradient was obtained by variation of the distance between the tip and an analyte. In a separate study, Sun *et al.* have reported an observation of an IR peak (B_u) of pyrazine adsorbed on the Ag films is due to the electric field gradient effect during the TERS experiment[15]. In principle, this was realized by bringing the tip very close to the metal surface, which made a nanogap structure. Subsequently, it provided the observation of multiple vibration modes, generation of second harmonics, and, more importantly, electric field gradient effects. These effects originated due to the higher-order Hamiltonian for the Raman frequencies of the molecule[15]. This higher-order term is more prominent when the molecule is placed in an inhomogeneous electromagnetic field. This experiment was also carried out in a high vacuum to ensure that the metal tip was close enough to the analyte molecule. Interestingly, simulating electromagnetic and quantum chemical calculation without considering high vacuum into account, the same group have proposed a strong possibility of generating the strong field gradient. Thus, the possibility remains that an efficient SERS substrate with enough capability to confine the high electric field in a strong manner can replace the high vacuum requirement, as seen in the TERS experiment. In this direction, Fazio *et al.*[2] have carried out a detailed study to show changes in Raman frequencies of varied sizes SnO_2 particles, from micron to nanometer ranges in the presence of Ag. This study revealed dissimilar Raman signals for the different SnO_2 NSs. For example, pellet and colloidal solution consisting of similar SnO_2 particles showed a strong

E_u (TO) mode. In contrast, a non-stochiometric thin film showed an enhancement in the Raman allowed mode (E_g) with no E_u (TO). The stochiometric film demonstrated strong E_u (TO) mode in the presence of Ag colloids. The presence of E_u (TO) mode during the Raman measurement was explained with the breaking of the mutual exclusion principle due to the metallic surfaces. The strong field gradient shifted the potential energy of the induced dipole in an asymmetric manner and affected the centrosymmetric nature of the SnO_2 crystal. Hence it eliminated the mutual exclusion principle in SnO_2 crystal. In contrast to the above, the present study with sample D (800 ^oC) shows a presence of IR active, A_{2u} (LO) mode at 696 cm^{-1} during the Raman measurement [Fig.3.6 (a)] indicating a possible violation of the mutual exclusion principle. Similarly, the presence of a Raman mode, E_g at 475 cm^{-1} from 25 nm SnO_2 in the FTIR spectrum, further supports the breaking of the mutual exclusion principle. Hence, beyond the breaking of the mutual exclusion principle, the critical role of a strong gradient field influencing the vibrational property by Raman measurements can be anticipated. This aspect, known as gradient field Raman (GFR), was first put forwarded by Ayars and Hallens in the year 2000. However, it is still a largely unexplored topic, especially for inorganic molecules[38]. Generally, the transition in the vibrational level due to coupling with the radiation field is described by perturbation Hamiltonian. The derivative of the spectroscopic signal proceeds with the first order expansion in the vibrational co-ordination Q and after elimination of Q independent term[38]:

$$\mu_a = \left\{ \left(\frac{d\mu_a^p}{dQ}\right)_0 + \left(\frac{d\alpha_{ab}E_{ab}}{dQ}\right)_0 \mathrm{E}_b + \frac{1}{3}\frac{\partial E_b}{\partial c}\left(\frac{dA_{abc}}{dQ}\right)_0 \right\} Q \qquad \mathbf{3.2}$$

Where, μ_a^P is the permanent dipole moment and α is the polarizability term. In general, E_b can be taken out from the 2nd term of RHS of equation 3.2 because it does not vary with Q. However, in the existence of a strong electric field gradient, the equation can be modified to[38]:

$$\mu_a = \left\{\left(\frac{d\mu_a^p}{dQ}\right)_0 + \left(\frac{d\alpha_{ab}}{dQ}\right)_0 \mathrm{E}_b + \alpha_{ab}\left(\frac{dE_{ab}}{dQ}\right)_0 + \frac{1}{3}\frac{\partial E_b}{\partial c}\left(\frac{dA_{abc}}{dQ}\right)_0\right\} Q \qquad \textbf{3.3}$$

1st term in the equation describes the IR absorption, 2nd term defines Raman scattering, and the last term indicates the GFR term. The third term is non zero in the presence of a strong electric field gradient. Further GFR selection rule requires that E belongs to the same symmetry species as the vibration or that dE/dQ be non-zero at Q=0. This will be true if the vibration has a component in the direction where E varies rapidly. This is a possible reason behind the observation of the E_u (TO) mode with a very high enhancement. This mode involves the in-plane vibration. Whereas the other IR peak A_{2u} vibrates out of the plane and may not be experiencing a strong change of the field gradient. Further considering the Hamiltonian of a molecule in an inhomogeneous EM field, the intensity ratio of IR peak (I_2) to Raman peak (I_1) can be co-related as [15, 39]:

$$\frac{I_2}{I_1} = 4 \times \frac{1}{3}\sum_{\alpha\beta\upsilon} \frac{A_{\alpha,\beta\upsilon}}{\alpha_{\alpha\beta}} \times \frac{\nabla E_{\beta\upsilon}}{E_\beta} \qquad \textbf{3.3}$$

Here ∇E refers to a gradient of the electric field. In the current report, high intensity in the IR peak is hence noticed because of the strong field gradient, which arises due to the formation of multiple junctions, including the nano junction in the Ag nanonets. Fazio *et al.*[2] have observed similar phenomenon, however, using Ag colloids for the SERS measurement of SnO_2 where they have increased the concentration of Ag to manipulate the electric field and hence the relative intensity of the IR peak. It is worthy to note that the influence of polarizability in the magnitude of the intensity from the Eqn.3.3 where the GFR term (3rd term) is directly proportional to the magnitude of polarizability. Hence, the effect of GFR proportionately increases with polarizability. Furthermore, SnO_2, an ionic compound, has a fairly high degree of ionic bonds. It, therefore, produces a high value of polarizability. The GFR effect should be strongest for the vibration mode for which an infrared absorption is strong. So, the ionic nature of SnO_2 is one further reason behind the observation of an enhanced IR peak in comparison to the Raman mode. Similar to Ag nanonets, Au nanoparticles or Au NRs are also used. However, no features as seen with Ag nanonets are observed, indicating inefficiency of generating required electric field locally to offer GFR effects.

3.2.3. Raman spectroscopic analysis of SnO_2 QDs in the presence of Ag nanonet

In contrast to the sample D (800 ^oC), the Raman spectrum of SnO_2 QDs possesses only a broad peak at 573 cm^{-1} [Fig. 3.7(b)]. However, in the presence of Ag nanonet, clear peaks have appeared (Fig.3.9). Most importantly, the existence of a 627 cm^{-1} peak is observed in the presence of Ag nanonets (Marked with a red arrow Fig.3.9).

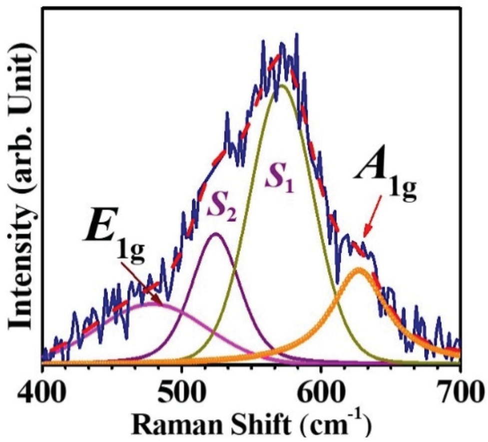

Figure 3.9 Raman spectrum of sample A (100 ^oC) in the presence of Ag nanonet.

This peak, close to A_{1g} mode (633 cm^{-1}) for the D sample, is ascribed to the A_{1g} mode from the SnO_2 QDs. So far, no report is there on the clear existence of A_{1g} mode in QDs SnO_2.Kuzume *et al.* have predicted the possible presence of A_{1g} mode using the DFT calculation; however, it failed to show it experimentally[12]. It is worth mentioning that they also had utilized the hot spots of shell-isolated nanoparticles (SHINs) as a SERS substrate. However, the EM enhancement obtained from the Shell-isolated nanoparticle enhanced Raman (SHINER) SERS substrate was not sufficient to enhance the A_{1g} mode frequency in the QDs. Earlier Raman study, as depicted in [Fig. 3.7(b)], has four constituent peaks (S_1, S_2, E_{2g}, and A_{1g})[32]. As described earlier, the peaks S_1 and S_2 arise due to a nonstoichiometric shell, which is thought to surround a small crystalline core. At the same time, E_{2g} and A_{1g} modes are intuitively fitted without knowing the exact position of the peaks. In contrast, the Raman data collected from QDs in the presence of Ag nanonet are now deconvoluted with a precise understanding of various modes such as E_g, S_1, S_2 along with an enhanced A_{1g} (Fig. 3.9). Thus, the experiment on QDs confirms the enhancement of the Raman allowed A_{1g} mode due to the use of strong plasmonic filed from the Ag nanonets. For further confirmation on the presence of A_{1g} peak in QDs, a high-pressure Raman study is done and described in the following section.

3.3. High-pressure Raman study on SnO_2 NPs

High-pressure Raman spectroscopic studies are carried out using a compact symmetric diamond anvil cell (DAC)[40]. Powder samples of SnO_2 NPs are loaded into a 200-μm hole of a stainless-steel gasket (pre-indented to a thickness of ~70-μm) in the DAC. A 4:1 methanol-ethanol mixture as a pressure transmitting medium is used, and Ruby balls as pressure calibrant are loaded along with the sample. Raman spectra of the sample in the DAC are collected using a 514.5 nm excitation line from an Ar-ion Laser using a 20 × long working distance objective, the spot size on the sample was about 1 μm. Raman spectra are also recorded in the pressure-reducing cycle. Ruby R1 fluorescence method was used for pressure measurements[41]. Raman spectra collected up to pressure 17.6 GPa for D (800 ^oC) and 17.2 GPa for A (100 ^oC) are depicted in Fig.3.10.

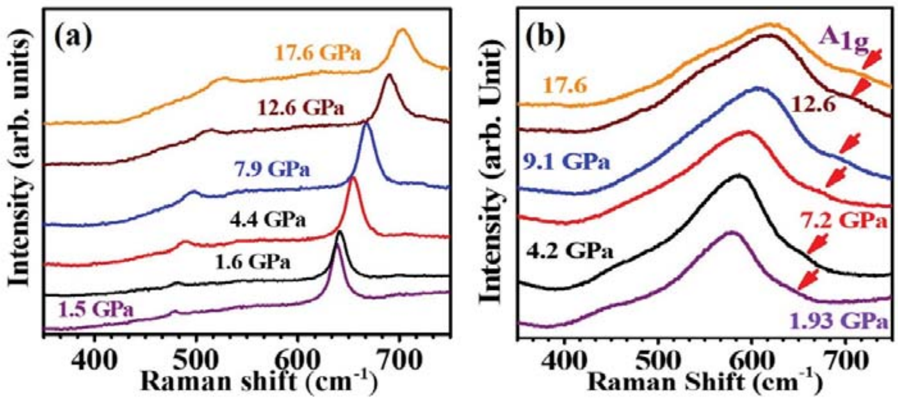

Figure *3.10 Pressure dependent Raman spectra of (a) D (800 ^{o}C) and (b) A (100 ^{o}C).*

High-pressure Raman modes observed in SnO_2 contains several information regarding the structure. It is noteworthy that in ambient condition, SnO_2 possess a rutile-type structure. Upon increasing the pressure, it transforms into $CaCl_2$ type at 11.8 GPa[40, 42]. However, prior to attaining the pressure SnO_2 exists in its pristine condition. It is interesting to observe a blueshift in the A_{1g} peak of sample D (800 ^{o}C) with increasing pressure. However, in the ambient condition, no A_{1g} peak can be identified for A (100 ^{o}C). But with increased pressure, a new peak is coming up for QDs. For instance, at 7.2 GPa, a small peak is found at ~664 cm^{-1}. This can be attributed to blue-shifted A_{1g}, which is otherwise masked under a broad *S* peak. The appearance of such Raman allowed peak at high pressure, further support the observation of the A_{1g} peak in QDs by the SERS investigation.

3.4. Summary

In summary, the presence of the broadband instead of Raman allowed mode in smaller crystalline SnO_2 NPs is a long-standing problem. However, the current chapter sheds light on this aspect by utilizing the Ag nanonets as SERS substrate. In terms of SERS substrates, Ag nanonets are found to be more efficient than the seed-mediated grown Au

NRs or Au NPs. With Ag nanonets, for the first time, the Raman allowed A_{1g} mode for the as-prepared QDs is observed. High-pressure Raman study further supports the presence of A_{1g} mode. Furthermore, the strong electric field around the Ag nanonets helps in the observation of an intense IR mode exclusively in the Raman spectrum of the 25 nm SnO_2 sample for the first time with a solid SERS substrate. A plausible explanation is also presented with GFR theory in regard to enhancement of the IR signal in the presence of a strong plasmonic field created by the Ag substrate.

3.5. References

[1] L.P. Ravaro, L.V. Scalvi, A.S. Tabata, F.M. Pontes, J.B. Oliveira, Nanoparticle characterization of Er-doped SnO_2 pellets obtained with different pH of colloidal suspension, Journal of Applied Physics, 114 (2013) 084304.

[2] E. Fazio, F. Neri, S. Savasta, S. Spadaro, S. Trusso, Surface-enhanced Raman scattering of SnO_2 bulk material and colloidal solutions, Physical Review B, 85 (2012) 195423.

[3] A. Kar, S. Kundu, A. Patra, Surface defect-related luminescence properties of SnO_2 nanorods and nanoparticles, The Journal of Physical Chemistry C, 115 (2010) 118-124.

[4] V. Bonu, A. Das, A. Sivadasan, A. Tyagi, S. Dhara, Invoking forbidden modes in SnO_2 nanoparticles using tip enhanced Raman spectroscopy, Journal of Raman Spectroscopy, 46 (2015) 1037-1040.

[5] S.-Y. Ding, E.-M. You, Z.-Q. Tian, M. Moskovits, Electromagnetic theories of surface-enhanced Raman spectroscopy, Chemical Society Reviews, 46 (2017) 4042-4076.

[6] A. Lee, A. Ahmed, D.P. dos Santos, N. Coombs, J.I. Park, R. Gordon, A.G. Brolo, E. Kumacheva, Side-by-side assembly of gold nanorods reduces ensemble-averaged SERS intensity, The Journal of Physical Chemistry C, 116 (2012) 5538-5545.

[7] J.C. Fraire, V.N. Sueldo Ocello, L.G. Allende, A.V. Veglia, E.A. Coronado, Toward the design of highly stable small colloidal SERS substrates with supramolecular host–guest interactions for ultrasensitive detection, The Journal of Physical Chemistry C, 119 (2015) 8876-8888.

[8] H. Xu, J. Aizpurua, M. Käll, P. Apell, Electromagnetic contributions to single-molecule sensitivity in surface-enhanced Raman scattering, Physical Review E, 62 (2000) 4318.

[9] M. Li, S.K. Cushing, N. Wu, Plasmon-enhanced optical sensors: a review, Analyst, 140 (2015) 386-406.

[10] W. Ji, X. Xue, W. Ruan, C. Wang, N. Ji, L. Chen, Z. Li, W. Song, B. Zhao, J.R. Lombardi, Scanned chemical enhancement of surface-enhanced Raman scattering using a charge-transfer complex, Chemical Communications, 47 (2011) 2426-2428.

[11] L. Bachenheimer, R. Scherzer, P. Elliott, S. Stagon, L. Gasparov, H. Huang, Degradation mechanism of Ag nanorods for surface enhanced Raman spectroscopy, Scientific Reports, 7 (2017) 1-4.

[12] A. Kuzume, M. Ozawa, Y. Tang, Y. Yamada, N. Haruta, K. Yamamoto, Ultrahigh sensitive Raman spectroscopy for subnanoscience: Direct observation of tin oxide clusters, Science advances, 5 (2019) eaax6455.

[13] A. Maity, A. Maiti, B. Satpati, A. Patsha, S. Dhara, T.K. Chini, Probing localized surface plasmons of trisoctahedral gold nanocrystals for surface enhanced Raman scattering, The Journal of Physical Chemistry C, 120 (2016) 27003-27012.

[14] S.N. Podoynitsyn, O.N. Sorokina, N.L. Nechaeva, S.V. Yanovich, I.N. Kurochkin, Surface-enhanced Raman spectroscopy in tandem with a gradient electric field from 4-mercaptophenylboronic acid on silver nanoparticles, Microchimica Acta, 187 (2020) 1-9.

[15] Y. Fang, Z. Zhang, L. Chen, M. Sun, Near field plasmonic gradient effects on high vacuum tip-enhanced Raman spectroscopy, Physical Chemistry Chemical Physics, 17 (2015) 783-794.
[16] M. Sun, Z. Zhang, L. Chen, S. Sheng, H. Xu, Plasmonic gradient effects on high vacuum tip-enhanced Raman spectroscopy, Advanced Optical Materials, 2 (2014) 74-80.
[17] X. Huang, I.H. El-Sayed, W. Qian, M.A. El-Sayed, Cancer cells assemble and align gold nanorods conjugated to antibodies to produce highly enhanced, sharp, and polarized surface Raman spectra: a potential cancer diagnostic marker, Nano letters, 7 (2007) 1591-1597.
[18] J.A. da Silva, M.R. Meneghetti, New aspects of the gold nanorod formation mechanism via seed-mediated methods revealed by molecular dynamics simulations, Langmuir : the ACS journal of surfaces and colloids, 34 (2017) 366-375.
[19] B.K. Sahu, A. Dwivedi, K.K. Pal, R. Pandian, S. Dhara, A. Das, Optimized Au NRs for efficient SERS and SERRS performances with molecular and longitudinal surface plasmon resonance, Applied Surface Science, (2020) 147615.
[20] K. Park, L.F. Drummy, R.C. Wadams, H. Koerner, D. Nepal, L. Fabris, R.A. Vaia, Growth mechanism of gold nanorods, Chemistry of Materials, 25 (2013) 555-563.
[21] T.K. Sau, C.J. Murphy, Seeded high yield synthesis of short Au nanorods in aqueous solution, Langmuir : the ACS journal of surfaces and colloids, 20 (2004) 6414-6420.
[22] X. Huang, S. Neretina, M.A. El-Sayed, Gold nanorods: from synthesis and properties to biological and biomedical applications, Advanced materials, 21 (2009) 4880-4910.
[23] A.M. Michaels, J. Jiang, L. Brus, Ag nanocrystal junctions as the site for surface-enhanced Raman scattering of single rhodamine 6G molecules, The Journal of Physical Chemistry B, 104 (2000) 11965-11971.
[24] J.-M. Nam, J.-W. Oh, H. Lee, Y.D. Suh, Plasmonic nanogap-enhanced Raman scattering with nanoparticles, Accounts of chemical research, 49 (2016) 2746-2755.
[25] M.J. Mulvihill, X.Y. Ling, J. Henzie, P. Yang, Anisotropic etching of silver nanoparticles for plasmonic structures capable of single-particle SERS, Journal of the American Chemical Society, 132 (2009) 268-274.
[26] K. Kneipp, Y. Wang, H. Kneipp, L.T. Perelman, I. Itzkan, R.R. Dasari, M.S. Feld, Single molecule detection using surface-enhanced Raman scattering (SERS), Physical review letters, 78 (1997) 1667.
[27] C.J. Orendorff, L. Gearheart, N.R. Jana, C.J. Murphy, Aspect ratio dependence on surface enhanced Raman scattering using silver and gold nanorod substrates, Physical Chemistry Chemical Physics, 8 (2006) 165-170.
[28] S.-Y. Ding, J. Yi, J.-F. Li, B. Ren, D.-Y. Wu, R. Panneerselvam, Z.-Q. Tian, Nanostructure-based plasmon-enhanced Raman spectroscopy for surface analysis of materials, Nature Reviews Materials, 1 (2016) 1-16.
[29] L. Jensen, G.C. Schatz, Resonance Raman scattering of rhodamine 6G as calculated using time-dependent density functional theory, The Journal of Physical Chemistry A, 110 (2006) 5973-5977.
[30] J.A. Dieringer, K.L. Wustholz, D.J. Masiello, J.P. Camden, S.L. Kleinman, G.C. Schatz, R.P. Van Duyne, Surface-enhanced Raman excitation spectroscopy of a single rhodamine 6G molecule, Journal of the American Chemical Society, 131 (2008) 849-854.
[31] N.P. Pieczonka, R.F. Aroca, Single molecule analysis by surfaced-enhanced Raman scattering, chemical society reviews, 37 (2008) 946-954.
[32] B.K. Sahu, A. Das, Significance of in-plane oxygen vacancy rich non-stoichiometric layer towards unusual high dielectric constant in nano-structured SnO_2, Physica E: Low-dimensional Systems and Nanostructures, (2018).
[33] W. Zhou, R. Liu, Q. Wan, Q. Zhang, A. Pan, L. Guo, B. Zou, Bound exciton and optical properties of SnO_2 one-dimensional nanostructures, The Journal of Physical Chemistry C, 113 (2009) 1719-1726.
[34] F. Wang, X. Zhou, J. Zhou, T.-K. Sham, Z. Ding, Observation of single tin dioxide nanoribbons by confocal Raman microspectroscopy, The Journal of Physical Chemistry C, 111 (2007) 18839-18843.
[35] X. Peng, L. Zhang, G. Meng, Y. Tian, Y. Lin, B. Geng, S. Sun, Micro-Raman and infrared properties of SnO_2 nanobelts synthesized from Sn and SiO 2 powders, Journal of applied physics, 93 (2003) 1760-1763.

[36] A. Dieguez, A. Romano-Rodrıguez, A. Vila, J. Morante, The complete Raman spectrum of nanometric SnO 2 particles, Journal of Applied Physics, 90 (2001) 1550-1557.
[37] L.Z. Liu, J.Q. Xu, X.L. Wu, T.H. Li, J.C. Shen, P.K. Chu, Optical identification of oxygen vacancy types in SnO2 nanocrystals, Applied Physics Letters, 102 (2013) 031916.
[38] E. Ayars, H. Hallen, C. Jahncke, Electric field gradient effects in Raman spectroscopy, Physical review letters, 85 (2000) 4180.
[39] L. Meng, Z. Yang, J. Chen, M. Sun, Effect of electric field gradient on sub-nanometer spatial resolution of tip-enhanced Raman spectroscopy, Scientific reports, 5 (2015) 1-5.
[40] H.T. Girão, T. Cornier, S.p. Daniele, R.g. Debord, M.A. Caravaca, R.A. Casali, P. Mélinon, D. Machon, Pressure-Induced Disordering in SnO_2 Nanoparticles, The Journal of Physical Chemistry C, 121 (2017) 15463-15471.
[41] S. Sahoo, T. Ravindran, S. Chandra, R. Sarguna, B. Das, T. Sairam, V. Sivasubramanian, C. Thirmal, P. Murugavel, Vibrational spectroscopic and computational studies on diisopropylammonium bromide, Spectrochimica Acta Part A: Molecular and Biomolecular Spectroscopy, 184 (2017) 211-219.
[42] H.T. Girao, P. Hermet, B. Masenelli, J. Haines, P. Mélinon, D. Machon, Pressure-Induced Sublattice Disordering in SnO_2: Invasive Selective Percolation, Physical review letters, 120 (2018) 265702.

Chapter 4

PL based selective ammonia detection and waveguide application in SnO_2 NSs

SnO_2 with profound optical properties is less explored as an optical sensing material however, it is well studied for resistive sensors[1-5]. Further, its superior optical property makes 1-D NSs an alluring nominee for waveguide application[6]. In this chapter, SnO_2 NPs, including QDs of 2.4 nm, are discussed for the PL sensing of aqueous ammonia (NH_3). For a comparative study, different sizes of NPs are used, and the selectivity of NH_3 is tested against analytes, like ethanol, methanol, and propanol. Importantly, NH_3 is considered a hazardous chemical for health with a threshold limit of 30 ppm[7]. Performances of the SnO_2 NPs as an optical sensor, along with characteristics such as recovery, reproducibility, and a wide detection range (32 to 256 ppm) at room temperature, are discussed in detail. A quartz-based chamber coupled with 325 nm laser is utilized for PL sensor study from SnO_2 NPs. Two obscured PL peaks at 2.77 and 2.96 eV are observed to be enhanced significantly from SnO_2 NPs due to NH_3 exposures. Their alterations in intensities with exposed NH_3 concentrations serve as sensor signals. Details of sensor mechanism with emphasis on the correlations between surface defects associated with Sn and Ov in SnO_2 NPs for the enhancement of 2.77 and 2.96 eV PL peaks are elaborated in this chapter. In the second section of this chapter, the utility of SnO_2 1-D NSs such as circular, square, and rectangular cross-section for waveguide application is discussed. The PL emission from 1-D NSs upon excitation with a 325 nm laser is found to be guided through the NSs to accomplish as a waveguide for the transmitting visible light. X-ray absorption spectroscopy (XAS), lifetime measurements, and temperature-dependent PL studies are also carried out. With a detailed probe of the nature of defects in NSs, a possible band diagram of the SnO_2 NS is also proposed.

4.1. PL based optical sensor

In this section, the changes in the PL of different SnO_2 NPs in the presence of various analytes are described. Prior to that, the luminescence properties of the NPs are described in detail.

4.1.1. Luminescence properties of SnO_2 using PL

For understanding the intricacy of defects prevailing in SnO_2 NPs, PL spectra are obtained from samples A (100 ºC), B (300 ºC), C (500 ºC), and D (800 ºC) using 325 nm laser excitation, and the results are depicted in Fig 4.1.

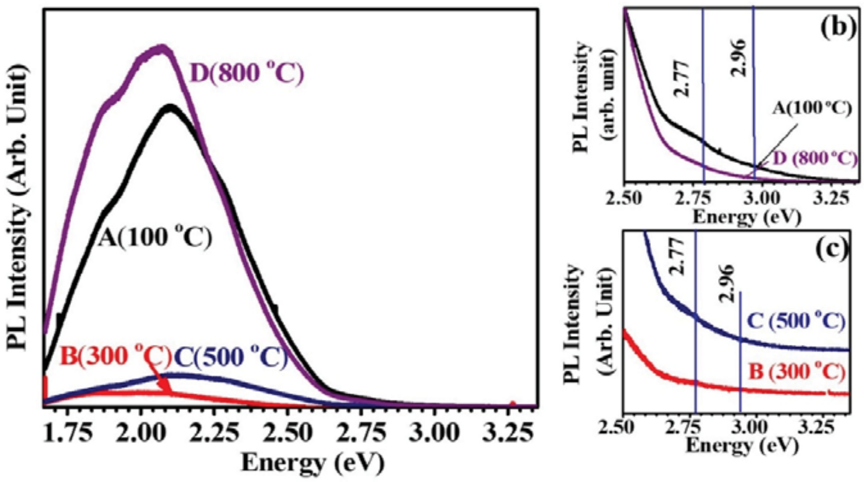

Figure 4.1 PL of SnO_2 NPs at (a) RT and existence of peaks at 2.77 and 2.96 eV for samples (b) A&D and (c) B&C

.

The detailed synthesis, structural, and morphological characterization of these samples are already discussed in the chapter-2. Samples B, C, and D are prepared by annealing the QDs (A) at 300, 500, and 800 ºC, respectively. All these NPs demonstrate a broad PL peak at around 2.1 eV, however, with varying intensities [Fig. 4.1(a)]. This attribute is due to the presence of O_V [8-11] in SnO_2 NPs. Among them, the as-prepared sample exhibits the strong PL peak, which is reduced drastically to a nominal value for sample B (300 ºC) of 4.1 nm size (Fig.4.1). The decreased intensity indicates the annihilation of defect centers responsible for the strong luminescence (from 1.87 to 2.5 eV) because of the annealing process in the air atmosphere. However, the same further increases with an increase in the annealing temperatures (500 and 800 ^oC). Such an increase in intensity happens due to the further creation of Ov by the desorption process of oxygen at higher temperatures [12]. The detailed analysis of O_V is elaborated in the following section of the chapter. Besides the broad PL peak, two feeble peaks could be seen at 2.77 and 2.96 eV in Fig. 4.1(b) [for A (100 ^oC) and D (800 ^oC)] and Fig. 4.1 (c) [for B (300 ^oC) and C (500 ^oC)].

4.1.2. Effect of NH_3 on PL

For the purpose of recording PL sensor responses from SnO_2 NPs, a quartz chamber is used, and its schematic representation is shown in Fig. 4.2. for contactless measurement.

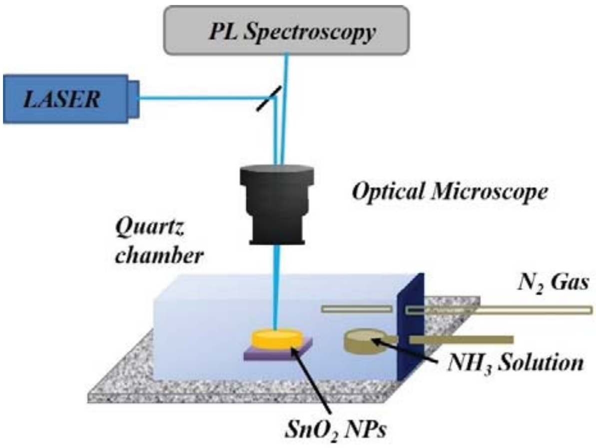

Figure 4.2 Schematic view of the set-up used for PL sensor study with different analytes.

For a source of NH_3 as an analyte, 50 µl (3.125 %) of aqueous NH_3 is inserted inside the quartz chamber, and the concentration of NH_3 gas is determined to be 256 ppm using the following formula [13]:

$$C_{ppm} = \frac{\delta \times V \times R \times T \times 10^6}{M \times P_b \times V_b} \quad \textbf{4.1}$$

Where the density, molecular weight, and volume of exposed NH_3 is given by δ, M and V, respectively. Further, R and T refer to universal gas constant and absolute temperature, respectively. P_b and V_b are the chamber pressure and volume, respectively. After each measurement, N_2 is purged to get rid of the exposed gas. The recorded PL spectra are shown in the Fig.4.3 for different NPs in the absence and presence of NH_3 exposure. Clearly, there is a strong increase in PL intensity, in particular, above 2 eV in the presence of NH_3.

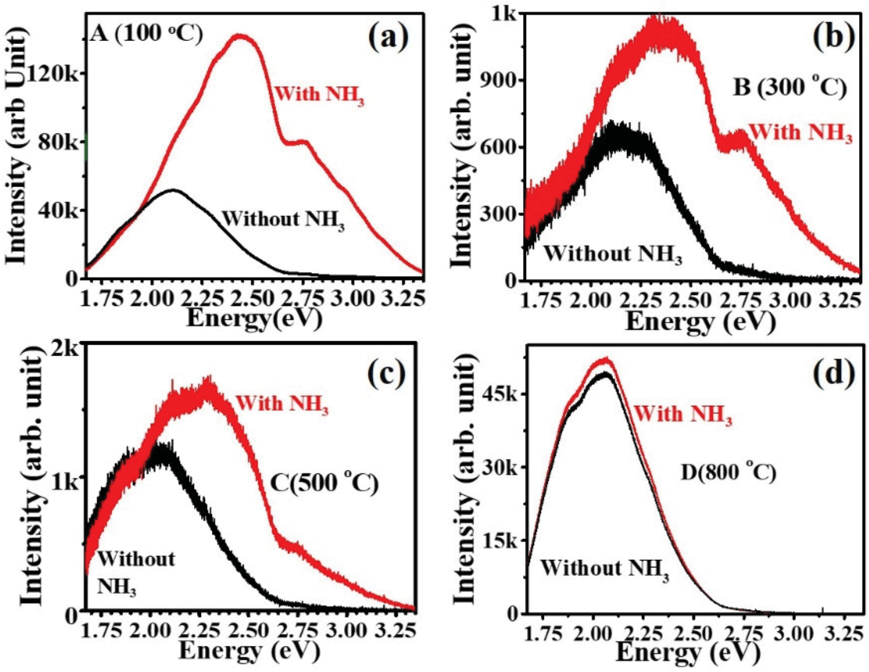

Figure 4.3 PL collected in the absence and presence of NH_3 for (a) A (100 °C), (b) B (300 °C), (c) C (500 °C), and (d) D (800 °C) samples.

Among all NPs, the highest enhancement comes from A (100 °C) sample, and the particle D (800 °C) of ~ 25 nm shows the least response to NH_3 exposure. Further, B and C samples also show nominal enhanced PL spectra with NH_3 exposures. To understand the reason for enhancements and the different responses from varied sizes, a detailed investigation is done and elaborated in the next section.

4.1.3. Origin of PL in SnO_2 NPs

The broad PL peak from A (100 °C) and D (800 °C) due to O_V is depicted in Fig.4.1[8, 14]. For a better insight into the distribution of O_V defects, PL spectra are deconvoluted into five Gaussian peaks, which are centered at 1.85, 1.96, 2.11, 2.28, and

2.45 Ev, results are shown in Fig.4.4. The first three positions (1.85, 1.96, and 2.11 eV) correspond to V_B defects, while the peaks at 2.28 and 2.45 eV represent V_P defects [15, 16].

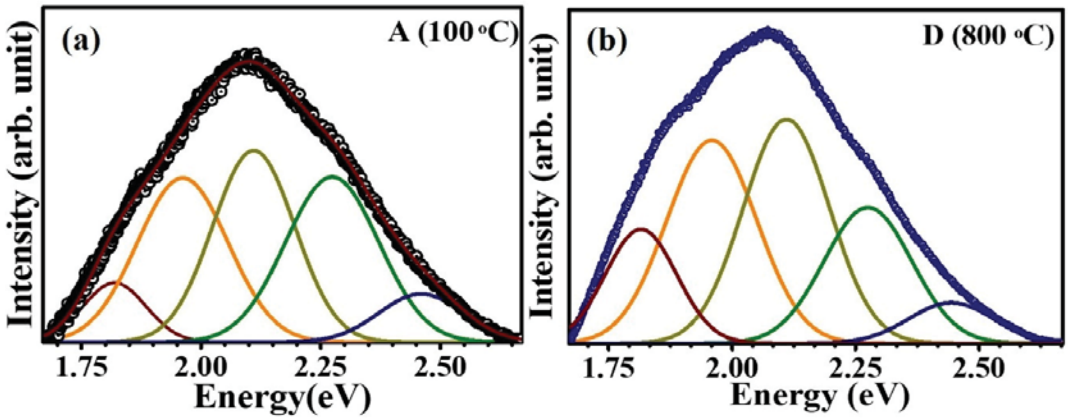

Figure 4.4 Convoluted PL spectra of (a) A (100 °C) and (b) D (800 °C).

Both the V_P and V_B defects are related to the removal of oxygen from the in-plane and bridging position of SnO_2 crystal, respectively. A schematic presentation is given in Chapter-1(Fig 1.2) to demonstrate the V_P and V_B and their successive removal to create respective vacancy sites[17, 18]. The formation of these vacancies in SnO_2 leads to the creation of certain energy levels inside the bandgap[18, 19]. The transitions of the electron from these defect states to the ground state make the above discussed emissions as a broad peak at 2.1 eV.

PL measurements for both samples A and D with a liquid N_2 controlled Linkam stage are done from a temperature of 80 K to RT. Results are shown in Fig. 4.5 to shed light on the possible positions of V_B and V_P inside the band.

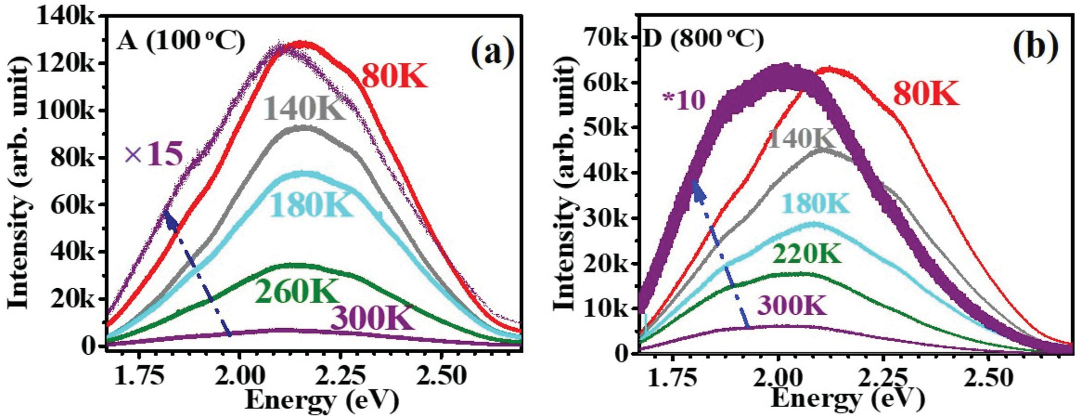

Figure 4.5 Temperature dependent PL spectra of (a) A (100 °C) and (b) D (800 °C) samples.

It is evident from Fig. 4.5 that with lowering the temperature, an enhancement in PL signal is observed for both samples, and on arriving at 80 K, it shows the highest intensity. This observation indicates the existence of shallow donor states in SnO_2 NPs[12]. Comparing various PL spectra recorded at 80 K and RT for an individual sample, the increased intensity of V_P (peak above 2.28 eV) is also found to be stronger than that of the V_B peaks at lower temperatures. This increase shows that V_P defects create an energy band closer to the conduction band minimum (CBM)[8, 16]. Apart from V_P and V_B defects, as shown in Fig.4.1, there are two other obscured peaks, at 2.77 and 2.96 eV. Notably, PL peak above 2.6 eV of SnO_2 NSs as a blue emission has attracted considerable research interest [19-21]. For instance, Zhou *et al.* have reported a very fast decay lifetime for a PL transition above 2.6 eV and slow decay for the PL emission below 2.6 eV[19-21]. The fast decay was assigned to a direct transition from the CBM to a level 0.9 eV above the VBM without the involvement of any trap state. This band is related to the loss of surface oxygen. However, the later transition with < 2.6 eV was interpreted with the help of traps states for electron transitions from a vacancy level slightly below the CB edge (shallow donor). Lettieri *et al.* have shown a similar PL feature at 2.75 eV from SnO_2 NWs[18]. They have assigned this observation to the typical role of "extended to localized" and "localized to localized" transitions between the surface and the projected band structure of SnO_2. The extended to localized transition happens due to transitions from the bulk-like CB states to localized O_V states at the 'Γ' point and results in a PL peak at around 2.75 eV with a feeble intensity[17]. One more point is a possible lift of degeneracy at the 'Γ' point in the band as described by Lettieri *et al.,* who have considered a flat band structure everywhere above the VBM except at 'Γ' point. Thus, there are possible two transitions at the 'Γ' point due to lifting in the degenerate energy state of the band near the VBM. Such origin of two states is presumably the reason behind the observation of two distinct peaks at 2.77 and 2.96 eV in the current study. Noteworthy, Lettieri *et al.*, have focused only on the flat band condition and have explained only the observed peak at 2.75 eV. Further, any role of the surface truncation of SnO_2 NPs for the origin of these peaks is investigated and illustrated below. Generally, Sn in SnO_2 is six-coordinated and surrounded by six O atoms[17, 22]. However, at surfaces, Sn has a reduced coordination number from six to five or four[23]. These five and four-coordinated Sn atoms carry charge states in the form of Sn^{4+} and Sn^{2+}, respectively, and it acts as surface traps for the photo-excited electrons, which can undergo non-radiative recombination later[10, 24]. Thus, a blue emission arises due to the presence of surface truncated Sn atoms, and the related lifetime is found to be less than other transitions (1.87-2.45 eV)[19]. It is obvious that in the reduced particle size the truncated Sn atoms become huge in number, and hence features related to it are prevalent. Thus, QDs with the largest specific surfaces has the most dominant such features compared to 25 nm D (800 ^{o}C) particles. For further supports for above explanation and insights about the role of defects, EELS and XAS studies are carried out in the following section.

4.1.4. Electron energy loss spectroscopy (EELS)

EELS focuses on the assertion of the electronic states of both Sn and O atoms in SnO_2[25, 26]. As certain O_V is present in the metal oxide, EELS is, therefore, a relevant and useful tool to provide information about the unoccupied electronic state of the metal oxide along with details about the prevalent surface defects. The typical role of the defects interacting with the absorbed molecule at room temperature is of high importance for the sensor study[15]. EELS investigation is performed on both the as-prepared A (100 °C), and the D (800 °C) samples, and the results are depicted in Fig.4.6.

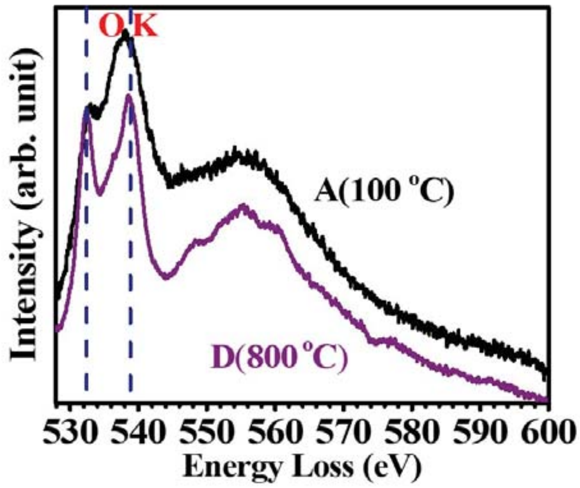

Figure 4.6 O K edge EELS for SnO_2 NPs.

Two major peaks observed at 532.2 and 538.4 eV represent the O *K* edges, arising from the transitions of electrons from the core to O 2*p* and O 2*p*-Sn 5*p* hybridization states, respectively. The difference between these two peaks, 6.2 eV, is considered as a fingerprint for the rutile tetragonal phase of SnO_2[25]. However, the broadness of the peak, as observed for the as-prepared QDs, represents an increased surface defect state from the un-coordinated atoms[27]. To obtain information regarding Sn $M_{4,5}$ peaks, the X-ray absorption near-edge spectroscopy (XANES) is carried out and discussed in the following section.

4.1.5. X-Ray absorption near-edge spectroscopy

XANES measurement is performed at the XAS beamline (BL-1) in total electron yield (TEY) mode at INDUS-2 synchrotron source (2.5 GeV, 200 mA) of the Raja Ramanna Center for Advanced Technology (RRCAT), Indore, India. The Sn $M_{5,4}$ edge is recorded for both A (100 °C) and D (800°C) and shown in Fig.4.7.

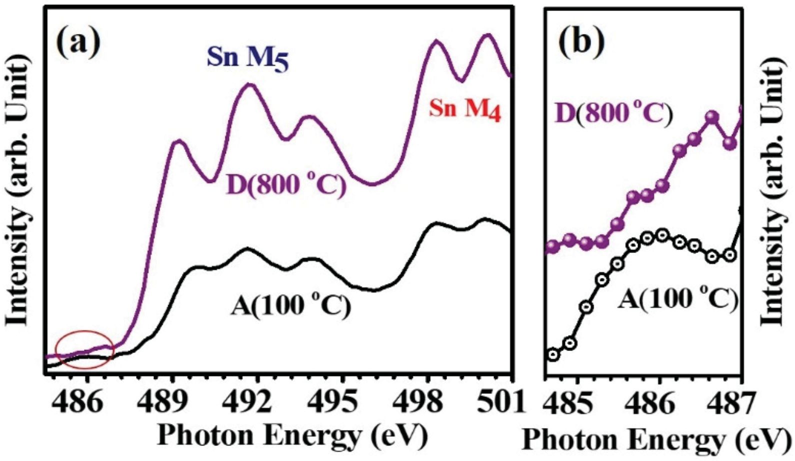

Figure 4.7 (a) Sn $M_{4,5}$ edge XANES spectra of SnO_2 NPs (b) Zoom of the encircled part of Fig (a).

XANES probes the unoccupied density of states above the Fermi level via dipole selection rule that is *d* to *p* and *d* to *f* for the Sn 3*d* ($M_{5,4}$) edge (spin-orbit splitting into $3d_{3/2}$ and $3d_{5/2}$ levels giving rise to M_4 and M_5 edges, respectively) [Fig. 4.7(a)[28, 29]. Two distinct peaks at 498 and 500 eV are observed due to Sn M_4 edges for both samples. Besides that, three distinct features of Sn M_5 are observed at 489, 491, and 493 eV for both QDs and 25 nm NPs. However, the relative decrease in intensity with a broadening effect in the peak is seen only for the SnO_2 QDs except for a peak at 493 eV [Fig. 4.7(a)]. The peak at 493 eV increases in intensity compared to the 491eV peak for the QDs. Similar observation was reported and correlated to an increase in the specific surface area for smaller particles[29]. For deeper insights, Kucheyev *et al.* have estimated a partial density of state (PDOS) corresponding to Sn $M_{5,4}$ edge to corroborate the increasing intensity of the 493 eV peak with the smaller size of particles[29]. It was concluded that the increased intensity of the 493 eV feature was possible due to the overlapping of the original peak of SnM_5 with another peak, which arose due to the spin-orbital-split of SnM_4. This additional feature of SnM_4 is surface-sensitive and more prominent for a smaller particle. The additional surface-related counterpart results in a weak peak at 486 eV due to the pre-edge of the Sn *M* component

[Fig. 4.7(b)]. Zhou *et al.* have shown a similar pre-edge peak in SnO_2 NWs in total electron yield (TEY) mode, which was absent in the bulk phase[19, 20]. They have correlated it to the under-coordinated surfaces with Sn atoms that have provided a 2.7 eV luminescence peak of a PL spectrum. As discussed earlier, transition-related to 2.77 and 2.96 eV should show a faster decay compared to the PL peak below 2.6 eV, and the following lifetime measurement supports that.

4.1.6. Lifetime measurement

Transitions above 2.6 eV in the PL spectrum do involve any initial trap state, and hence the transition is directly from the CBM to energy states created above the VBM. These states just above the VBM appear due to the un-coordinated surfaces of Sn atoms. However, the PL transitions below 2.6 eV occur involving the initial traps states, created by O_V, mainly V_P and V_B [19]. The lifetime measurement of 2.27 eV peak is shown in Fig. 4.8 (a). The resultant spectrum is fitted with a tri-exponential equation, and lifetimes are estimated. Similarly, the lifetime of a peak at 2.8 eV is also recorded and fitted. The result is shown in Fig. 4.8 (b). It turns out that transition corresponding to 2.8 eV exhibits a lower lifetime than the peak at 2.27 eV to indicate a quicker decay in a predicted way. Thus, the clear role of Sn truncated defects for peaks above > 2.6 eV is illustrated.

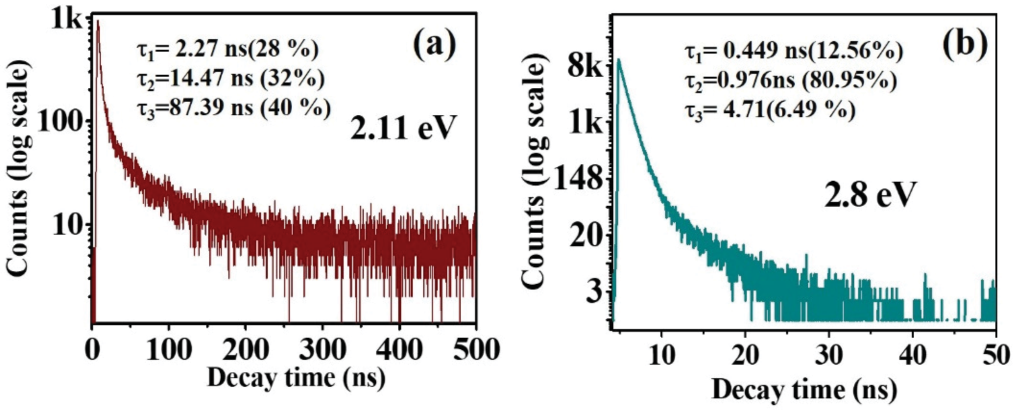

Figure 4.8 Lifetime measurements of SnO_2 QDs for the emissions at (a) 2.27 and (b) 2.8 eV.

4.1.7. Band diagram of SnO_2 NPs

Based on the above discussions, the probable PL transitions in the SnO_2 NP are a combination of transitions involved with O_V (V_P and V_B) and surface truncated or un-coordinated Sn atoms. The former one, O_V creates a band closer to the CBM and links to electrical conductivity. The later type of defects create energy states above the VBM. A schematic diagram is given to describe the band diagram of SnO_2 NPs in Fig. 4.9, and the combined mechanism is summed up as follows:

1. The excitation in SnO_2 NPs starts with the creation of an electron-hole pair after the laser excitation. The electron is promoted to the CB, leaving a hole in the VB. However, the direct recombination electron-hole for the CB to the VB transition is dipole forbidden and is not seen as PL for SnO_2 NPs. However, the active hole created can be trapped in the energy band created above the VBM[19].
2. The photo-excited electron comes back to the energy level created just below the CB due to V_P or V_B. The electrons from these states recombine with the holes trapped in the energy states above the VBM. The transitions from V_B result in emissions at 1.88, 1.99, and 2.14 eV, whereas transitions from V_P result in emissions at 2.29 and 2.45 eV. Due to the involvement of the trap states, these transitions possess a higher decay time. This feature is corroborated with the exhibition of a higher decay lifetime for 2.27 eV peak [Fig.4.9 (a)].
3. Further, the photo-exited electron may recombine directly from the CB to the hole above the VBM (created due to under coordinated Sn^{4c} atom Sn^{2+}) to provide PL peaks at 2.77 and 2.96 eV. However, Sn^{4+} acts as a surface trap for these electrons and affects the transition probability. In subsequence, obscured peaks with very weak intensity appear at 2.77 and 2.96 eV (as shown in scheme 4.9). As these transitions happen without the involvement of a first trap, they exhibit a lower decay time, and it is discussed in the previous section with Fig.4.8 (b) for the emission peak

at 2.8 eV. In this case, the passivation of Sn^{4+} can lead to an enhanced probability to allow an overall improvement in the intensities for peaks at 2.77 and 2.96 eV.

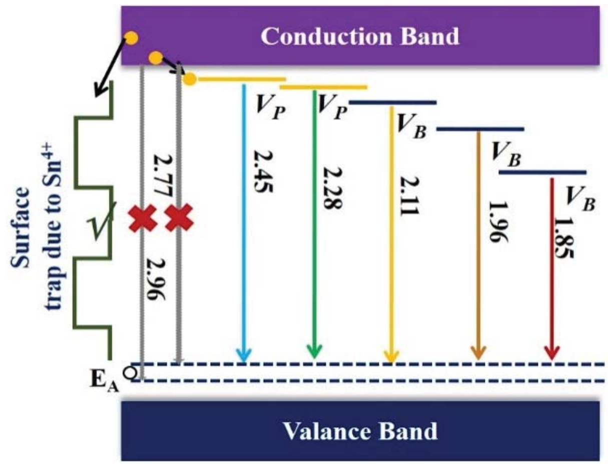

Figure 4.9 Band diagram for SnO_2 NPs showing different PL transition levels.

Understanding the origin of PL spectra helps to decipher the enhancement of some selective PL peaks observed in certain NPs. For instance, the smallest particle [A (100 ºC)-QDs] shows the highest response in contrast to the biggest particle ~25 nm [D (800 ºC)] with NH_3 exposures. Thus, further detailed interpretation PL measurements are taken in the presence of different concentrations of NH_3 for SnO_2 QDs and discussed in the following section in detail. This exercise leads to develop a selective PL NH_3 sensor at room temperature.

4.1.8. Blue emission for selective ammonia sensor

To enumerate the interaction of NH_3 with SnO_2 NPs, PL measurements are recorded from the SnO_2 QDs with NH_3 exposures. As a source of NH_3, 50 µl of different concentrations (3.125, 1.55, 0.781, 0.39, and 0%) of aqueous NH_3 solution are introduced inside the quartz chamber. The concentrations of NH_3 from solution are determined to be 256, 128, 64, and 32 ppm, respectively, by using Eqn. 4.1[13]. The recorded PL is given in the following Fig. 4.10.

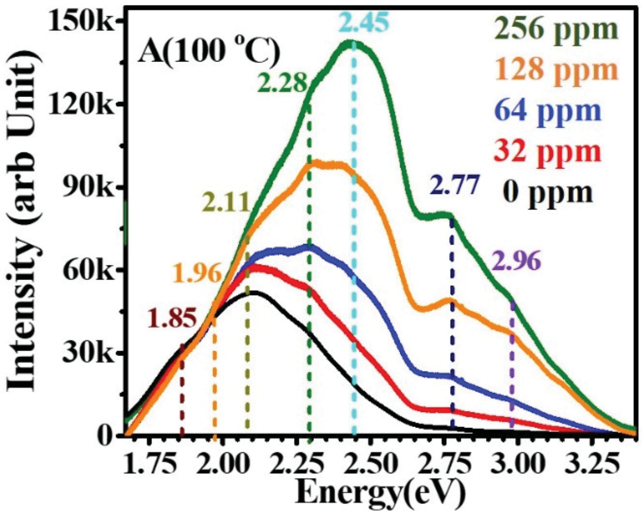

Figure 4.10 PL spectra collected in the presence of different concentrations of NH_3.

There is an increase in the PL intensity above 2.28 eV with NH_3. This spectral region deals mostly with V_P and direct transitions from the CBM to the band 0.9 eV above the VBM. However, the PL region associated with V_B remains mostly unaffected. Further, with an increase of NH_3 concentration, a gradual enhancement of the PL region is observed for QDs (Fig.4.10). The PL spectra collected for different concentrations of NH_3 are deconvoluted further to access insights into the prevailing mechanism for sensor responses. The deconvoluted spectra are shown in Fig.4.11.

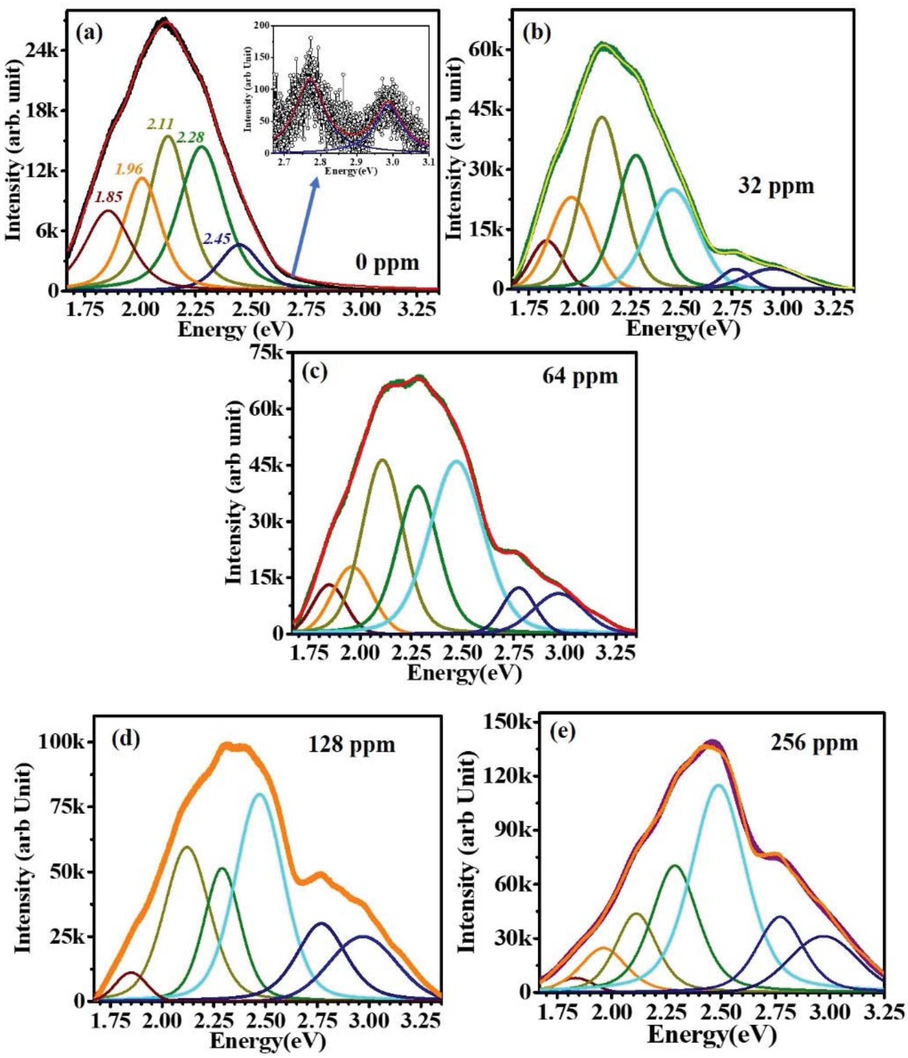

Figure 4.11 Convoluted PL spectra of the SnO_2 QDs exposed to (a)0, (b)32, (c) 64, (d)128 and (e)256 ppm of NH_3.

It is evident from the above plots that the presence of NH_3 influences mostly the peak related to V_P (2.28 and 2.45eV) and the undercoordinated Sn atom (2.77 and 2.96 eV). Furthermore, the obscured 2.77 and 2.96 eV peaks as shown in the inset of Fig. 4.11(a), are enhanced highly for QDs. Such enhancement serves as a sensor signal. The sensor response, R, is calculated for all deconvoluted peaks (1.85, 1.96, 2.11, 2.28, 2.45, 2.77, and 2.96 eV) using the formula R= $(I_{gas}-I_0)/I_{gas}$. Where, I_{gas} and I_0 are the areas under the curve of a particular peak in the presence and absence of NH_3. The results are depicted in Fig. 4.12[16]. Significantly, peaks corresponded to direct transitions from the conduction band (2.77 and

2.96 eV) show the strongest response [Fig.4.12(a)]. However, V_P related transitions (2.45 and 2.28 eV) display better performance than the V_B related PL peaks (1.85,1.96 and 2.11 eV) as seen from Fig.4.12 (b).

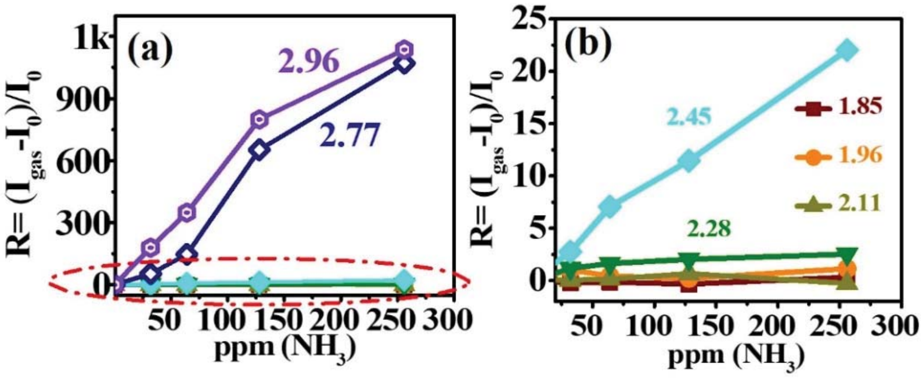

Figure 4.12 (a) Sensor responses of QDs for all the peak positions, (b) zoomed version of the encircled part for peaks, V_P and V_B.

4.1.9. PL sensing mechanism

A strong rise in intensities of 2.77 and 2.96 eV peaks is observed in the presence of NH_3 for smaller particles or, in other words, NPs with the higher surface to volume ratios. These transitions are connected to the under coordinated Sn atoms (Sn^{4+} and Sn^{2+}) found on the truncated surfaces. Moreover, Sn^{4+} and Sn^{2+} act as Lewis acids[30-32], which can attract Lewis bases. So, acidic SnO_2 surfaces can interact with NH_3, a Lewis base, because of the presence of a lone pair of electrons. Marikutsa *et al.* have revealed the crucial impact of particle dimension on the distribution of acidic sites on the metal oxide surfaces[32, 33]. By elaborating the outcomes from thermal desorption profiles (TDP) of NH_3, they have demonstrated that smaller SnO_2 particle possesses a high amount of acidic sites. In a separate study on deep oxidation of toluene, the important role of acidic sites with the varying particle size of SnO_2 was also documented[34]. In that study, the active attachment of the acidic site occurs for toluene because of the presence of a delocalized Π bond, which acts as a strong electron donor. The small particle with a large amount of acidic surface side was reported to act as the most efficient candidate for the deep oxidation of toluene. In the current discussion (Fig.4.9), the un-coordinated metal cations (Sn^{4+}) act as a trapping site also for the photogenerated electrons and make 2.77 and 2.96 eV related PL peaks less intense. On the other hand, during the exposure, NH_3 is engaged with Sn^{4+} through acid-base interaction, and in this process, the site (Sn^{4+}) is not then readily available to trap the photo-excited electrons. Consequently, the photo-excited electrons become free to make the transitions directly from the CBM to the acceptor level above the VBM and enhance the PL intensity in the region of 2.77 and 2.96 eV. A scheme highlighting the above process is illustrated in Fig. 4.13 for the proposed mechanism. However, with increased particle size, the available acidic sites decrease strongly on the SnO_2 surface, and hence the big particles fail to show responses to NH_3 exposures as good as the QDs.

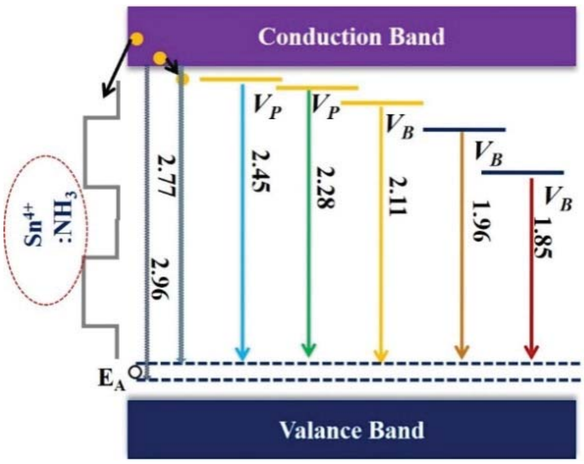

Figure 4.13 PL transitions in SnO_2 NPs during interaction with NH_3.

4.1.10. Theoretical support for the sensing mechanism

Based on the above-proposed mechanism, the presence of both Sn^{5c} and Sn^{4c} is equally vital. While the former acts as an adsorption site for NH_3, and the latter helps in the creation of an energy state above the VBM. However, both the sites [Sn^{5c}(Sn^{4+}) and Sn^{4c}(Sn^{2+})] are acidic and prone to attach with NH_3.To find out the most favorable site for NH_3 adsorption, first-principles density functional theory (DFT) based calculations are employed using VASP (Vienna ab-initio simulation package) with a plane-wave basis set

[35]. Interaction between electron and nucleus is described using the projector augmented wave method (PAW)[36]. For exchange-correlation energy, the generalized gradient approximation (GGA) based exchange-correlational revised Perdew-Burke-Ernzerhof (rPBE) functional is used[37]. The energy cut-off for the plane waves is chosen to be 500 eV. Brillouin zone was sampled using 5×5×1, *k*-point mesh with a total energy tolerance of 10^{-8} eV for reaching SCF. All structures are relaxed until the force on each atom was less than a value of 0.005 eV/Å. The simulation cell consists of a surface slab containing four SnO_2 (110) layers with 48 atoms, and a vacuum separation of 12 Å is given in the Z direction. SnO_2 (110) surface is chosen as it is the most stable site for rutile SnO_2. To find out the favorable adsorption site for Lewis base NH_3 on the (110) surfaces of SnO_2, two different sites [Fig.4.15 (a) Sn^{5c} (five coordinated Sn), (b) Sn^{4c} (four coordinated Sn)] are chosen. The Sn^{4c} site is created by removing the O_B to mimic the real scenario of the reduced surfaces closely. For all sites, the adsorption energy is calculated using the equation: E_{ads}= E_{tot}-E_s-E_m[38]. Where, E_{tot}, $E_{s,}$ and E_m refer to the total energies of the SnO_2 slab with adsorbed NH_3 on the surface, the SnO_2 slab alone before the NH_3 adsorption, and the isolated NH_3 molecule, respectively. Negative E_{add} indicates that the adsorption is energetically favorable, or the reaction is exothermic. For the simulation of the slab and cell image, the VESTA program is utilized and shown in Fig.4.14.

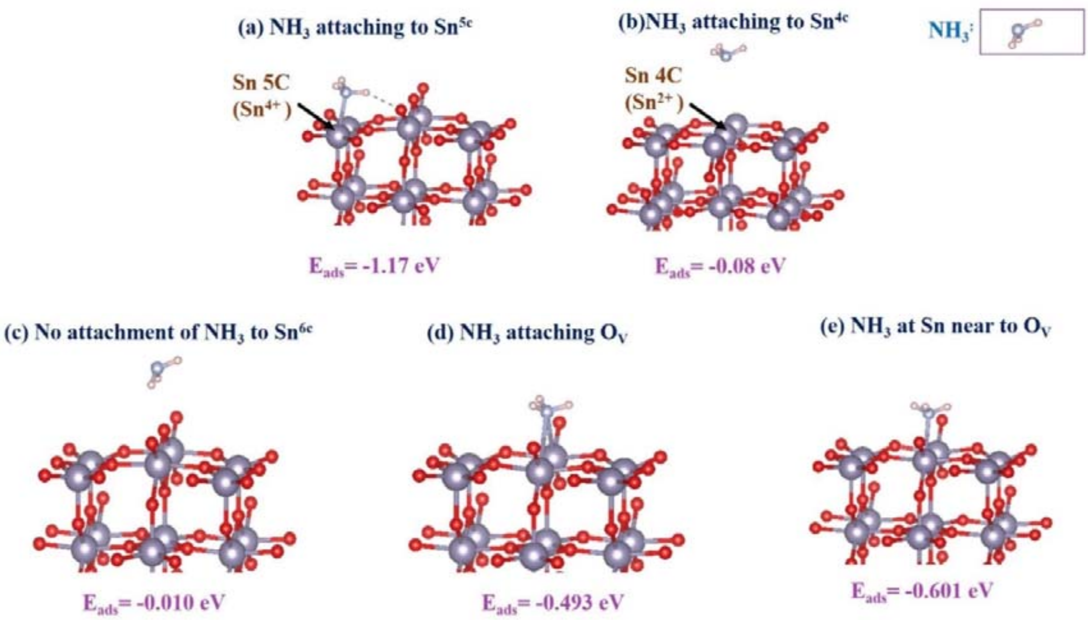

Figure 4.14 Scheme of the adsorption of NH_3 at different sites of SnO_2 (110) surfaces.

From the DFT calculation, E_{ads} for the Sn^{5c} and Sn^{4c} are found to be -1.17 and -0.08 eV, respectively [Fig.4.14 (a) and (b)]. The lower value indicates that Sn^{5c}, which carries a +4 charge, is the most favorable site for NH_3 adsorption. Further, the energy of adsorption is found to be negative, and hence it points to the feasibility of the reaction at room temperature without any external temperature. Additionally, other adsorption sites like Sn^{6c}, O_V, and Sn near to O_V are tried for NH_3 attachment and depicted in Fig.4.14. All other energies are found to be higher than that of the Sn^{5c} adsorption site.

4.1.11. Recovery study

After each measurement, N_2 is purged into the chamber to get rid of NH_3 and to check the recovery of the sensor. PL intensity at 2.77 eV peak is constantly monitored during the presence and absence of different concentrations of NH_3. The intensity of PL peak at 2.77 eV is depicted in Fig. 4.15 to understand the recovery.

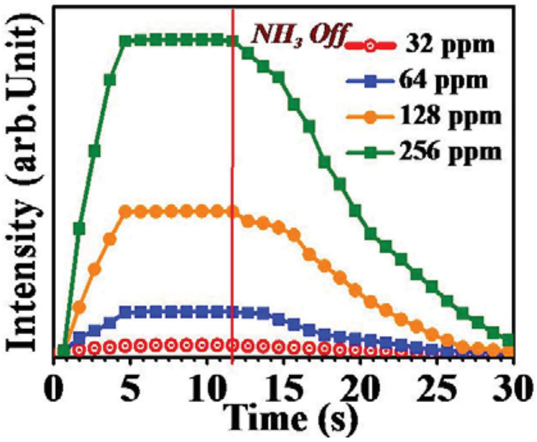

Figure 4.15 Sensor response and recovery time with reference to the intensity of 2.77 eV peak of SnO_2 QDs. The vertical line indicates the starting point of the recovery of a PL sensor with N_2 purge.

A quick response is observed. To attain 90% of saturation value for a concentration, it responds within 5 s. The recovery of the sensor is found to be relatively slow, and it takes nearly 15 s to attain 90% of the base value from the saturation point. Quick response and recover indicate good practical efficiency of the PL based sensor.

4.1.12. Selectivity study

For selectivity studies other than NH_3, analytes like methanol, ethanol, and propanol are also investigated separately, and PL data are collected from the QDs. The results are shown in Fig.4.16.

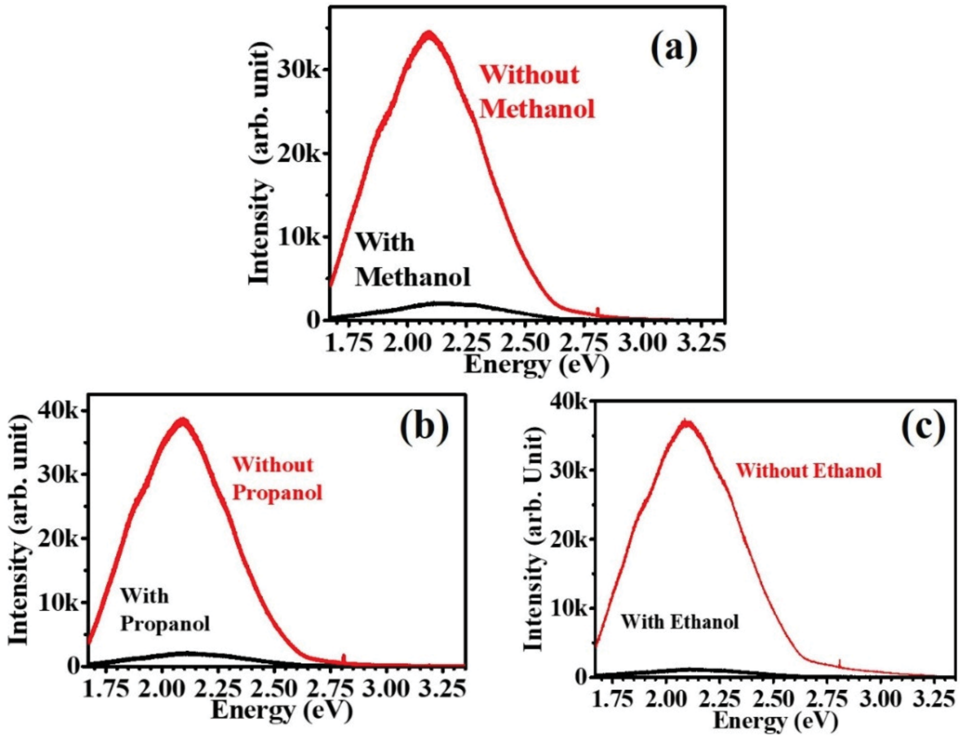

Figure 4.16 Displaying changes observed in PL signals after exposing to (a) methanol, (b) propanol, and (c) ethanol.

A marked difference from NH_3 is that no enhancement is observed in the region of 2.77 and 2.96 eV for other analytes. Moreover, overall PL intensity reduces. This reduction in intensity is due to the scavenging of electrons of the analyte molecule, as reported with regard to the presence of the hydroxyl group (-OH)[1, 23]. The analyte interacts with the SnO_2 surfaces to withdraw electrons from them, instead of selective reaction with the Lewis sites of the SnO_2 surfaces. This aspect affects the PL intensity as there is a lack of electrons for photoluminescence transitions. A schematic presentation is given in Fig. 4.17 to describe the interaction mechanism for a typical analyte like different alcohols with SnO_2 NPs.

Figure 4.17 Scheme of the active and dead region of SnO_2 NP as created before and after exposure to alcohol.

Hydroxyl group (-OH) present in alcohol can interact with SnO_2 surfaces. The -OH group acts as an electron scavenger by withdrawing electrons from the SnO_2 surface. The very fact may lead to a dead region that is an electron-deficient region, as explained by Yadav *et al*[1]. Being insensitive to the PL transition, the dead region does not contribute to PL transitions as opposed to the observation for NH_3, which interacts with Lewis acid sites efficiently. In brief, alcohol by possible adsorption facilitates the formation of a dead region and decreases the PL intensity of SnO_2 drastically.

A series of experiments are conducted to realize the PL based ammonia detection starting from 32 to 256 ppm by utilizing SnO_2 QDs at room temperature. The abundance of acidic sites present on the smaller particle size is found to be responsible for the NH_3 sensing. With increasing particle size, reduction of acidic size results, and thus bigger particles fail to respond efficiently towards the PL based NH_3 sensor. Further, among other volatile analytes, the Lewis base ammonia is effectively detected in a selective manner.

4.2. PL based waveguide of 1-D NSs

The current section is pursued to realize the importance of 1-D NSs as a waveguide. In general, waveguides are known to guide the light sent from one end to another[6, 39]. However, here the PL guided waveguide behavior of different SnO_2 1-D NSs will be discussed.

1-D SnO_2 NWs of different morphology are grown in horizontal quartz tube furnace by using catalytic VLS and self-catalytic VS methods as described in Chapter-2. In both cases, synthesized SnO_2 QDs of size 2.4 nm is used as a precursor material. It is worth mentioning that VLS grown samples comprise NWs of two different dimensions based on the growth temperature. It is noted in the previous chapter 950 and 1000 ºC growth temperature results in square and cylindrical shape NWs, respectively. Further, it is found that square-shaped NWs have a bigger width than the width of cylindrical shape NWs[40]. Additionally, NWs samples grown by VS technique possess random NSs. A few of them are μB, and a few of them of beak shape. All these 1-D NSs are employed for waveguide study. Prior to that, PL spectra are collected from all these 1-D NSs to analyze the defect induced luminescence spectra.

4.2.1. PL of SnO_2 1-D NSs

Room temperature PL is collected for all the 1-D NSs using 325 nm laser excitation and shown in Fig.4.18 (a). Irrespective of the morphology, the PL spectrum is similar for all the NSs at RT with the highest intensity at 2.1 eV. As discussed for SnO_2 NPs, this 2.1 eV peak corresponds to the presence of O_V. For further insight into defects distribution, a temperature-dependent PL study is carried out to probe the luminescence properties of the SnO_2 1-D NSs using a liquid N_2 controlled Linkam stage. Figure 4.18 (b) and (c) show the temperature-dependent PL measurements of the VLS process grown cylinder and square-shaped NWs, respectively. Fig.4.18 (d) shows the temperature-dependent PL emissions for the VL grown μB. It is clear that for all NSs, there are six peaks positioned at 1.84, 1.97, 2.1, 2.3, 2.5, and 2.75 eV, which overlap with each other to give a broad peak. An increase in PL intensity with decreasing temperature [Fig.4.18 (b)-(d)] indicates transitions from shallow donor levels, as described in section 4.1.9. However, the highest intensity at room temperature found at 2.1 eV corresponds to yellow color. The next section discusses the guiding of this defect induced PL light through the 1-D NSs.

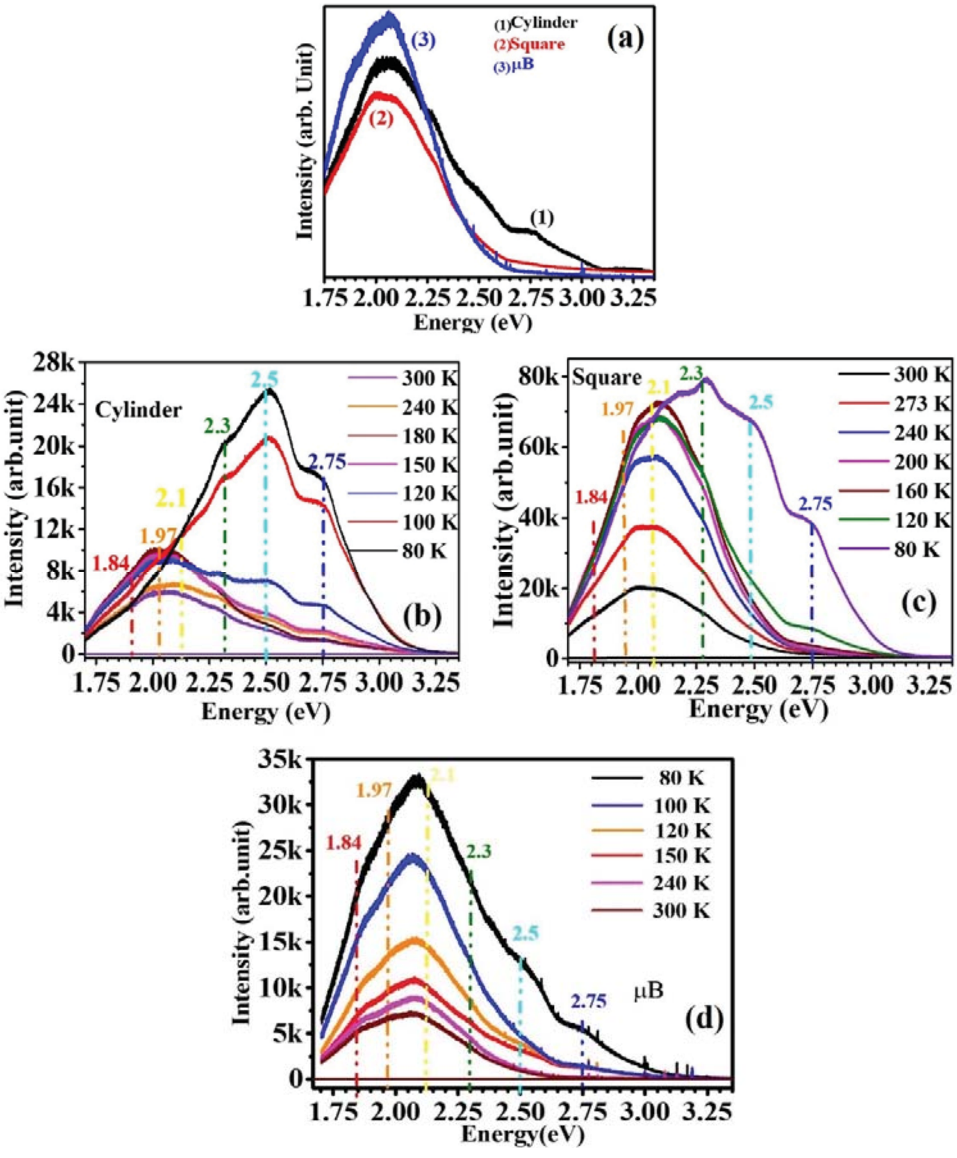

Figure 4.18 (a) PL spectra collected from all 1-D NSs, temperature-dependent PL studies of (b) cylindrical, (c) square-shaped nanowire, and (d) μB.

4.2.2. SnO_2 1-D NSs for waveguide application

The NWs are excited with 325 nm to observe the waveguide nature, as depicted in the schematic Fig.4.19.

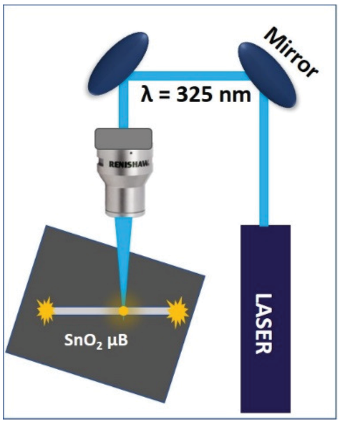

Figure 4.19 Schematic view for the waveguide study of 1-D SnO_2 NSs.

Optical images of the 1-D NSs waveguides are captured with the help of the same optical microscope using a long working distance 50x objective with a numerical aperture (N.A.) of 0.45. The images are in RGB format with the spectral response (gamma) and light intensity corrected.

Fig.4.20 (a) and (b) show the waveguide nature of the square-shaped NWs of thickness around 200 to 250 nm, where emitted yellow-red light travelled for 50 μm. Fig.4.20 (c) and (d) show the waveguide nature of the cylinder-shaped NWs of thickness around 100 to 150 nm. Light has travelled through almost 180^o bent NW [Fig.4.20(c)]. In Fig.4.20(d), apart from the tip of the exciting wire, the tip of the next wire is also glowing with intense yellow-red light. It is interesting to observe that though 325 nm laser is shined on 1-D NSs, a yellow color light is coming out from both the end of NSs. This indicates luminescence of the wires is guided by the NWs. As we have discussed earlier, the PL spectra show the highest intensity at 2.1 eV, which corresponds to yellow light.

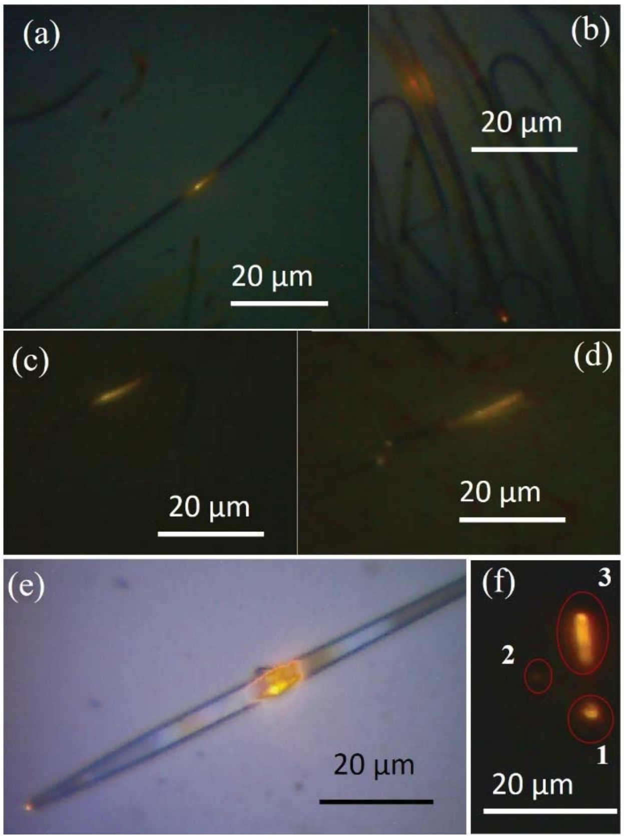

Figure 4.20 Waveguide nature of (a) and(b)square-shaped NWs, (c)and(d) cylinder-shaped NWs and (e)Tapered µB and (f) 'V' shaped µB.

Similarly, Fig. 4.20(e) shows the tapered SnO_2 NB waveguide. The width of the wire at the excitation point is around 2 µm, whereas, at the tip, the width is around 500 nm only. Tapered waveguide focuses the light at a small point efficiently. Importantly, tapered SnO_2 waveguide is used in endoscopy of micron-sized cells, single-photon sources, and strongly entangled photon pairs. Fig. 4.20(f) shows a 'V' shaped nano waveguide having an angle of 52^{o} between two handles. In this case, one of the ends '1' was excited with 325 nm laser. Consequently, emitted visible light travelled through the wire and came out at a sharp corner, '2'. Some parts of this light still travelled through the other handle and came out at position '3'. It is observable that the loss of the light at a sharp edge is high. The loss of a major amount of light at a sharp edge can be attributed to the defects and the sudden change in the waveguide direction.

4.2.3. Guiding mechanism and cut-off frequency of 1-D NSs

SnO2 1-D NSs are proved to be very good waveguides among the metal oxides[40, 41]. Well-faceted NWs majorly support axial Fabry–Pérot waveguide modes[42, 43]. High difference in the refractive index value with air (η = 1) and SnO_2 (η = 2.1) enables photonic confinement in the NW cavities. The observed waveguide nature arises from defects controlled luminescence in the visible range of SnO2 as detailed in the PL study section. In all of the cases, the highest intensity of PL peak at 2.1 eV corresponding to yellow colour is found to be guided through 1-D NSs.

For understanding the propagation of luminescence through the NWs, cut-off width is deduced. Cut-off width for cylindrical shaped NWs to guide yellow light (2.2 -2.10 eV) is found to be around 140 nm (Eqn.4.2) width of the cylindrical NWs. Similarly, for the square-shaped NWs, the cut-off width is found to be around 160 nm (Eqn. 4.3)[44].

$$a = \frac{1.841c}{2\pi\eta f_c} \quad \textbf{4.2}$$

$$b = \frac{c}{2\eta f_b} \quad \textbf{4.3}$$

Where f_c and f_b stand for the cut-off frequencies of cylindrical and square-shaped NW, respectively. Whereas *c* is the velocity of light and η (= 2.1) is the refractive index of SnO_2. '*a*' and '*b*' being the cut-off radius of cylindrical NW and cut-off width of the square-shaped NW, respectively. Importantly, these dimensions are within the scope of the cut-off dimension of NWs, as deduced in the earlier chapter-2. [experimentally obtained value for cylinder ~ 150 nm and square-shaped

NW is 200 nm]. Hence theoretical approach suggests that the propagation of luminescence is a possible phenomenon.

4.3. Summary

PL based sensor with 325 nm laser allows selective detection of trace amount of NH_3 for the first time at room temperature. Two nearly obscured PL peaks of SnO_2 at 2.77 and 2.96 eV are found to evolve significantly in the presence of the NH_3. Enhancement of these two peaks is taken as sensor output and it offers detection up to ~ 32 ppm of NH_3 with a high recovery rate at room temperature. Dipole forbidden rule outlawed band to band transition in SnO_2. Hence, the presence of the defect is the sole reason for luminescence. The enhancement of obscured peaks in the presence of NH_3 indicates the importance of certain defects. To explore the origin of the defect, X-ray absorption spectroscopy (XAS) is carried out with synchrotron radiation. From XAS, the spectral presence of pre-edge resonance peak at the SnM_5 edge is detected for SnO_2 QDs and indicates surface states due to the existence of a larger fraction of un-coordinated surface Sn atoms due to surface reconstruction and oxygen vacancies. The selectivity of NH_3 over alcohol is further tested. Besides, waveguide application of 1-D SnO_2 NSs by utilization of PL property under the 325 nm laser excitation on a single nanowire is demonstrated. During this process, PL is generated and guided through the 1-D NS is observe to transit in NWs under an optical microscope.

4.4. References

[1] K. Yadav, S.K. Gahlaut, B. Mehta, J. Singh, Photoluminescence based H_2 and O_2 gas sensing by ZnO nanowires, Applied Physics Letters, 108 (2016) 071602.
[2] B. Bhangare, N.S. Ramgir, S. Jagtap, A. Debnath, K. Muthe, C. Terashima, D.K. Aswal, S.W. Gosavi, A. Fujishima, XPS and Kelvin probe studies of SnO_2/RGO nanohybrids based NO_2 sensors, Applied Surface Science, 487 (2019) 918-929.
[3] K.C. Lam, B. Huang, S.-Q. Shi, Room-temperature methane gas sensing properties based on in situ reduced graphene oxide incorporated with tin dioxide, Journal of Materials Chemistry A, 5 (2017) 11131-11142.
[4] P. Sun, Y. Cai, S. Du, X. Xu, L. You, J. Ma, F. Liu, X. Liang, Y. Sun, G. Lu, Hierarchical α-Fe_2O_3/SnO_2 semiconductor composites: Hydrothermal synthesis and gas sensing properties, Sensors and Actuators B: Chemical, 182 (2013) 336-343.

[5] S. Lettieri, A. Setaro, C. Baratto, E. Comini, G. Faglia, G. Sberveglieri, P. Maddalena, On the mechanism of photoluminescence quenching in tin dioxide nanowires by NO_2 adsorption, New Journal of Physics, 10 (2008) 043013.
[6] L. Zhang, G. Wu, F. Gu, H. Zeng, Single MoO_3 nanoribbon waveguides: good building blocks as elements and interconnects for nanophotonic applications, Scientific reports, 5 (2015).
[7] H.C. Su, M. Zhang, W. Bosze, N.V. Myung, Tin Dioxide Functionalized Single-Walled Carbon Nanotube (SnO_2/SWNT)-Based Ammonia Gas Sensors and Their Sensing Mechanism, Journal of The Electrochemical Society, 161 (2014) B283-B290.
[8] M. Epifani, J.D. Prades, E. Comini, E. Pellicer, M. Avella, P. Siciliano, G. Faglia, A. Cirera, R. Scotti, F. Morazzoni, The role of surface oxygen vacancies in the NO_2 sensing properties of SnO_2 nanocrystals, The Journal of Physical Chemistry C, 112 (2008) 19540-19546.
[9] L.Z. Liu, J.Q. Xu, X.L. Wu, T.H. Li, J.C. Shen, P.K. Chu, Optical identification of oxygen vacancy types in SnO2 nanocrystals, Applied Physics Letters, 102 (2013) 031916.
[10] A. Kar, S. Kundu, A. Patra, Surface defect-related luminescence properties of SnO_2 nanorods and nanoparticles, The Journal of Physical Chemistry C, 115 (2010) 118-124.
[11] B.K. Sahu, A. Das, Significance of in-plane oxygen vacancy rich non-stoichiometric layer towards unusual high dielectric constant in nano-structured SnO_2, Physica E: Low-dimensional Systems and Nanostructures, (2018).
[12] V. Bonu, A. Das, A.K. Prasad, N.G. Krishna, S. Dhara, A. Tyagi, Influence of in-plane and bridging oxygen vacancies of SnO_2 nanostructures on CH4 sensing at low operating temperatures, Applied Physics Letters, 105 (2014) 243102.
[13] V. Mounasamy, G.K. Mani, D. Ponnusamy, K. Tsuchiya, A.K. Prasad, S. Madanagurusamy, Template-free synthesis of vanadium sesquioxide (V_2O_3) nanosheets and their room-temperature sensing performance, Journal of Materials Chemistry A, 6 (2018) 6402-6413.
[14] V. Bonu, A. Das, S. Amirthapandian, S. Dhara, A.K. Tyagi, Photoluminescence of oxygen vacancies and hydroxyl group surface functionalized SnO_2 nanoparticles, Physical Chemistry Chemical Physics, 17 (2015) 9794-9801.
[15] B.K. Sahu, A. Das, A.K. Prasad, G. Mangamma, The Role of In-Plane Oxygen Vacancy Defects in SnO_2 Nanoparticles for CH4 Sensing, Journal of nanoscience and nanotechnology, 19 (2019) 7764-7770.
[16] A. Das, V. Bonu, A.K. Prasad, D. Panda, S. Dhara, A.K. Tyagi, The role of SnO_2 quantum dots in improved CH_4 sensing at low temperature, Journal of Materials Chemistry C, 2 (2014) 164-171.
[17] F. Trani, M. Causà, D. Ninno, G. Cantele, V. Barone, Density functional study of oxygen vacancies at the SnO_2 surface and subsurface sites, Physical Review B, 77 (2008) 245410.
[18] S. Lettieri, M. Causà, A. Setaro, F. Trani, V. Barone, D. Ninno, P. Maddalena, Direct role of surface oxygen vacancies in visible light emission of tin dioxide nanowires, The Journal of chemical physics, 129 (2008) 244710.
[19] X. Zhou, F. Heigl, M. Murphy, T. Sham, T. Regier, I. Coulthard, R. Blyth, Time-resolved x-ray excited optical luminescence from SnO_2 nanoribbons: Direct evidence for the origin of the blue luminescence and the role of surface states, Applied physics letters, 89 (2006) 213109.
[20] J. Zhou, H. Fang, J. Maley, J. Ko, M. Murphy, Y. Chu, R. Sammynaiken, T. Sham, An X-ray absorption, photoemission, and Raman study of the interaction between SnO_2 nanoparticle and carbon nanotube, The Journal of Physical Chemistry C, 113 (2009) 6114-6117.
[21] F. Gu, S.F. Wang, M.K. Lü, G.J. Zhou, D. Xu, D.R. Yuan, Photoluminescence properties of SnO2 nanoparticles synthesized by sol− gel method, The Journal of Physical Chemistry B, 108 (2004) 8119-8123.
[22] W. Wang, Y. Liu, S. Liu, SnO_2 Nanostructure with Well-Engineered Crystal Facets by Zn Doping for Chemical Sensing Applications, Crystal Growth & Design, 20 (2020) 2742-2752.
[23] S. Ghosh, K. Das, K. Chakrabarti, S.K. De, Effect of oleic acid ligand on photophysical, photoconductive and magnetic properties of monodisperse SnO_2 quantum dots, Dalton Trans, 42 (2013) 3434-3446.
[24] M.W. Abee, D.F. Cox, NH3 chemisorption on stoichiometric and oxygen-deficient SnO_2 (1 1 0) surfaces, Surface science, 520 (2002) 65-77.
[25] M. Moreno, J. Kas, C. Ma, F. Wang, J. Rehr, M. Malac, Probing electronic structure of stoichiometric and defective SnO_2, Physical Review B, 95 (2017) 245206.

[26] M. Moreno, R. Egerton, J. Rehr, P. Midgley, Electronic structure of tin oxides by electron energy loss spectroscopy and real-space multiple scattering calculations, Physical Review B, 71 (2005) 035103.
[27] V. Bonu, B. Gupta, S. Chandra, A. Das, S. Dhara, A. Tyagi, Electrochemical supercapacitor performance of SnO_2 quantum dots, Electrochimica Acta, 203 (2016) 230-237.
[28] R.G. Pavelko, H. Daly, M. Hübner, C. Hardacre, E. Llobet, Time-resolved DRIFTS, MS, and resistance study of SnO_2 materials: the role of surface hydroxyl groups in formation of donor states, The Journal of Physical Chemistry C, 117 (2013) 4158-4167.
[29] S. Kucheyev, T. Baumann, P. Sterne, Y. Wang, T. Van Buuren, A. Hamza, L. Terminello, T. Willey, Surface electronic states in three-dimensional SnO_2 nanostructures, Physical Review B, 72 (2005) 035404.
[30] K.M. Mohammed, A. Chutia, J. Callison, P.P. Wells, E.K. Gibson, A.M. Beale, C.R.A. Catlow, R. Raja, Design and control of Lewis acid sites in Sn-substituted microporous architectures, Journal of Materials Chemistry A, 4 (2016) 5706-5712.
[31] M.N. Alaya, M.A. Rabah, Surface acidity and catalytic activity of aged SO_4^{2-}/SnO_2 catalyst supported with WO_3, Journal of Alloys and Compounds, 575 (2013) 285-291.
[32] A. Marikutsa, M. Rumyantseva, A. Gaskov, A. Samoylov, Nanocrystalline tin dioxide: Basics in relation with gas sensing phenomena part II. Active centers and sensor behavior, Inorganic Materials, 52 (2016) 1311-1338.
[33] A.V. Marikutsa, M.N. Rumyantseva, E.A. Konstantinova, T.B. Shatalova, A.M. Gaskov, Active sites on nanocrystalline tin dioxide surface: Effect of palladium and ruthenium oxides clusters, The Journal of Physical Chemistry C, 118 (2014) 21541-21549.
[34] Y. Liu, Y. Liu, Y. Guo, J. Xu, X. Xu, X. Fang, J. Liu, W. Chen, H. Arandiyan, X. Wang, Tuning SnO_2 surface area for catalytic toluene deep oxidation: on the inherent factors determining the reactivity, Industrial & Engineering Chemistry Research, 57 (2018) 14052-14063.
[35] G. Sun, J. Kürti, P. Rajczy, M. Kertesz, J. Hafner, G. Kresse, Performance of the Vienna ab initio simulation package (VASP) in chemical applications, Journal of Molecular Structure: THEOCHEM, 624 (2003) 37-45.
[36] G. Kresse, D. Joubert, From ultrasoft pseudopotentials to the projector augmented-wave method, Physical review b, 59 (1999) 1758.
[37] G. Kresse, J. Hafner, Ab initio molecular dynamics for liquid metals, Physical Review B, 47 (1993) 558.
[38] F. Shao, M.W. Hoffmann, J.D. Prades, J.R. Morante, N.r. López, F. Hernández-Ramírez, Interaction mechanisms of ammonia and tin oxide: A combined analysis using single nanowire devices and DFT calculations, The Journal of Physical Chemistry C, 117 (2013) 3520-3526.
[39] A.R. Davoyan, I.V. Shadrivov, A.A. Zharov, D.K. Gramotnev, Y.S. Kivshar, Nonlinear nanofocusing in tapered plasmonic waveguides, Physical review letters, 105 (2010) 116804.
[40] V. Bonu, B.K. Sahu, A. Das, S. Amirthapandian, S. Dhara, H.C. Barshilia, Sub-wavelength waveguide properties of 1D and surface-functionalized SnO_2 nanostructures of various morphologies, Beilstein journal of nanotechnology, 10 (2019) 379-388.
[41] R. Yan, J.-H. Park, Y. Choi, C.-J. Heo, S.-M. Yang, L.P. Lee, P. Yang, Nanowire-based single-cell endoscopy, Nature nanotechnology, 7 (2012) 191-196.
[42] P.J. Pauzauskie, A. Radenovic, E. Trepagnier, H. Shroff, P. Yang, J. Liphardt, Optical trapping and integration of semiconductor nanowire assemblies in water, Nature materials, 5 (2006) 97-101.
[43] R. Yan, D. Gargas, P. Yang, Nanowire photonics, Nature photonics, 3 (2009) 569-576.
[44] D.J. Griffiths, Introduction to electrodynamics, in, AAPT, 2005.

Chapter 5

Electrochemistry and photocatalysis applications

Defects in metal oxides have a tremendous influence on the electrical property. The present study highlights the critical role played by oxygen defects of SnO_2 QDs in electrochemical supercapacitor applications. A simple preparation method is used to incorporate the SnO_2 QDs in a carbon paper. This hybrid electrochemical capacitor shows improved capacitance value over the carbon paper electrode. Raman spectroscopy, TEM, and PL, EELS are also used to provide evidence for the presence of V_P in SnO_2 NPs. Further, the study is extended with GO as a hybrid electrochemical electrode. The main objective is to understand the typical role of functional groups of GO, a widely used starting material for rGO, in electrochemical applications. Notably, very large surfaces of GO can act as a suitable EDLC material for supercapacitor whereas, SnO_2 with variable oxidation states emerge as an excellent choice for pseudo-capacitor. In that regard, GO-SnO_2 nanocomposites are grown by in-situ and ex-situ growth procedures. The chapter details the impact of the functional groups of GO in the growth of in-situ SnO_2, the difference in the electrochemical results between two hybrid materials, and the possible explanation for the obtained electrochemical performances.

In the second section, the study focuses on the utilization of SnO_2 as a photocatalyst. A homemade photocatalysis reactor is used to demonstrate dye degradation by exciting light ranging from visible to UV wavelengths. For improving performance under the visible light, which forms the maximum part of the solar light, the utility of GO-SnO_2 composite is discussed. In general, carbonaceous materials like rGO are widely investigated for catalytic efficacy with SnO_2 NPs. The pristine GO was not chosen as a suitable photocatalyst because of its low conductivity. With a favorable work function from the GO, such composite appears to be a good candidate as a photocatalyst for dye degradation. An in-depth study with GO-SnO_2 composite is largely missing. In fact, the conductivity issue of GO can be addressed with SnO_2 QDs, which is proven to be an excellent candidate for charge carrier migration. Localized structural analysis is also done with the XANES investigation. Charge-transfer from SnO_2 to GO, which occur due to proper work function alignment, is examined by the PL and EIS.

5.1. SnO_2 QDs on carbon paper for electrochemical application

A hybrid electrode of SnO_2 QDs with carbon paper (CP) is made to realize the combined effect of pseudo-capacitance and EDLC. Firstly, the proper incorporation route of the QDs in a carbon paper is examined by various techniques before utilizing it as an electrode material.

5.1.1. Electrode preparation for electrochemical application

A white colored gel is prepared by adding 0.05M NH_4OH to $SnCl_4$ (Alfa Aesar) under continuous magnetic stirring at 80 ^oC as a source of SnO_2 QDs. For preparing the electrode, the white gel is used, which incorporates SnO_2 NPs in the CP, and electrochemical behaviour is studied. Prior to this, CPs of dimension 2×1 cm are cut and cleaned with DI water, alcohol, and acetone, respectively. Finally, these CPs are dipped in the washed gel for 5, 10, 15, and 20 min followed by a heat treatment at 100 ^oC, and they are referred to as CP-5, CP-10, CP-15, and CP-20, respectively. For the comparison purpose, the white gel is dried overnight at 100 ^oC and ground to obtain as-prepared SnO_2 QDs. The same sample is referred to as sample A (100 ^oC), as discussed in Chapter-2.

5.1.2. Structural analysis of electrode material

TEM images of SnO_2 NPs and SnO_2 in carbon paper are shown in Fig. 5.1 (a) and (d), respectively. For the preparation of the TEM sample of SnO_2-CP, a little amount is scratched to mix with propanol solvent. A few drops of the solution are cast on a copper grid for TEM analysis. TEM image indicates the average particle size is ~ 2.4 nm. It also provides further information on the crystalline phase. The lattice spacing ‘d’ is found to be

0.36 nm [Fig.5.1(b) and (e)] for both samples, and it matches the inter planner spacing of (110) plane of the rutile SnO2 phase[1]. The SAED study indicates short-range order with ring-like patterns that correspond to (110), (101), and (211) planes of rutile SnO_2, as shown in Fig. 5.1(c) and (f). The crystallite size of 2.4 nm is smaller than the Bohr exciton radius of 2.7 nm for SnO_2[2], and hence it is treated as QDs.

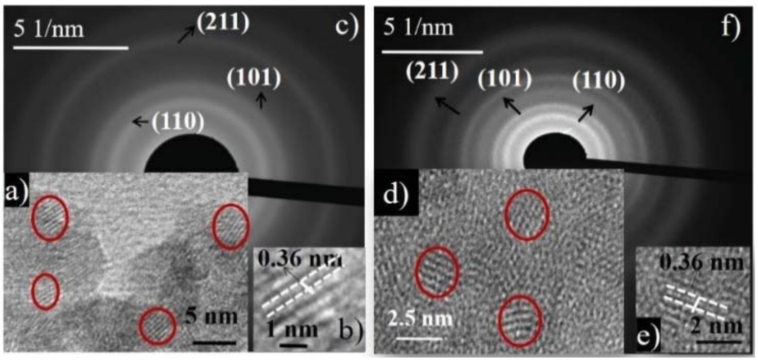

Figure 5.1 (a) TEM images, (b) lattice spacing, and (c) SAED patterns of SnO_2 QDs. (d) TEM image (b) lattice spacing and (f) SAED patterns of SnO_2 QDs in carbon paper matrix.

5.1.3. EELS analysis of SnO_2 QDs in a carbon electrode

EELS study offers rich information on structural aspects. EELS is collected from the electrode during TEM measurement and is shown in Fig.5.2. This EELS feature is quite similar to the EELS data obtained for SnO_2 QDs, as described in Chapter-4.

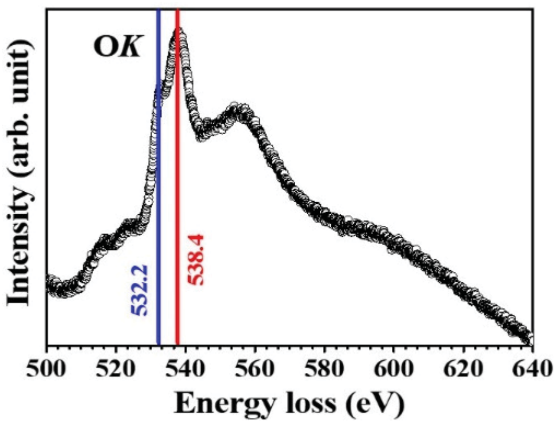

Figure 5.2 EELS of SnO_2 QDs in the carbon matrix.

Two major peaks found at 532.2 and 538.4 eV with a difference of 6.2 eV indicate a presence of Sn^{4+} state. A reduced intensity of the first peak is observed, and it is ascribed to low coordination of neighboring transition metal atom and subsequent formation of O_V. Mostly, this O_V can be V_P and V_B. Thus, a formation of the non-stoichiometry layer can be hypothesized due to surface arrangement and structural relaxation, which create a different symmetry compared to the bulk [3]. Peaks above 540 eV arise due to the multiple scattering resonance of SnO_2 NP_S[4].

5.1.4. Vibrational property of SnO_2 QDs in carbon electrode

Raman spectra collected with 514.5 nm laser from both SnO_2 QDs and SnO_2 decorated CP are shown in Fig.5.3.

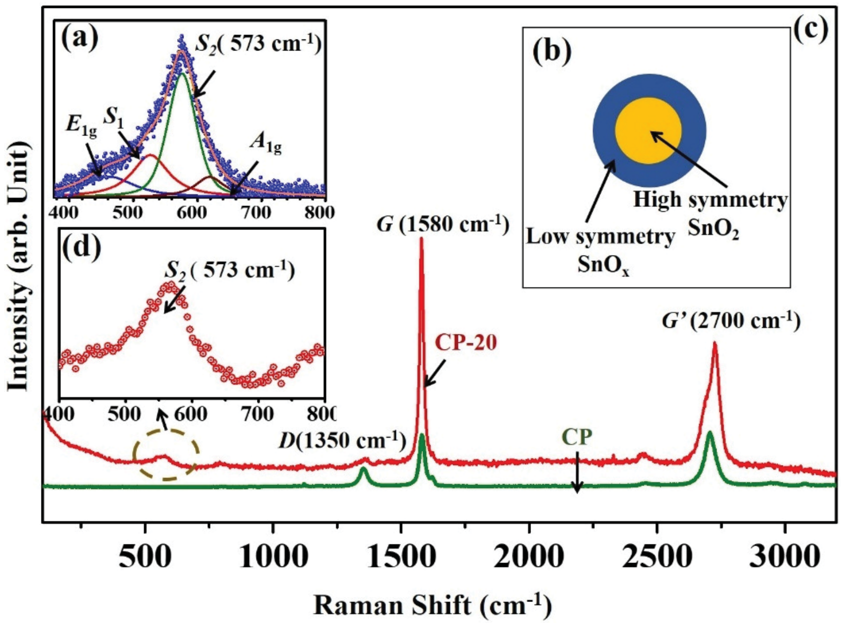

Figure 5.3 (a) Raman spectrum of SnO_2 QDs with Lorentzian fitting (b) schematic view of SnO_2 NPs with the depiction of non-stoichiometric layer (c) Raman spectra of CP and CP-20 (d)Zoomed version of the defect-related peak in SnO_2 from CP-20.

Raman spectrum of QDs displays a broad feature [Fig.5.3(a)]. Four Lorentzian peaks at E_{1g} (475 cm^{-1}), S_1 (526 cm^{-1}), S_2 (573 cm^{-1}), and A_{1g} (621 cm^{-1}) are fitted where E_{1g} and A_{1g} are Raman allowed modes[5, 6]. Importantly, a redshift of A_{1g} mode is observed with respect to the reported value at 633 cm^{-1} due to the reduced dimension effects. Other S_1 and S_2 modes are correlated to V_P that gives rise to a non-stoichiometry (SnO_x) layer [Fig.5.3(b)]. Peaks at D (1350 cm^{-1}), G (1580 cm^{-1}), and G' (2700 cm^{-1}) are observed from carbon paper only [Fig.5.3 (c)][7, 8]. The C-20 sample shows a carbon-related peak along with (S_2) 573 cm^{-1} [Fig. 5.3 (c) and (d)]. The presence of S_2 peak indicates the presence of V_P vacancies in SnO_2 and helps improving conductivity[9-11].

Detailed studies, as discussed in Chapter-4, with the help of temperature-dependent PL measurements and in upcoming chapter 6, solid-state ac-conductivity measurement and Cole-Cole plots, an active role of V_P in contributing to enhanced conductivity can be concluded [9, 12]. To look forward into the importance of the V_P in supercapacitor applications, detailed electrochemical analysis is done and discussed in the following section.

5.1.5. Electrochemical property of SnO_2 QDs

Electrochemical measurements are carried out in three-electrode configurations (Metrohm-Autolab model PGSTAT302N). SnO_2 coated carbon papers (CP-5,10,15 and 20), platinum electrode, and Ag/AgCl are used as the working electrode, the counter electrode, and the reference electrode, respectively, in 1M H_2SO_4 electrolyte. A schematic description to describe the three-electrode system is given in Fig. 5.4.

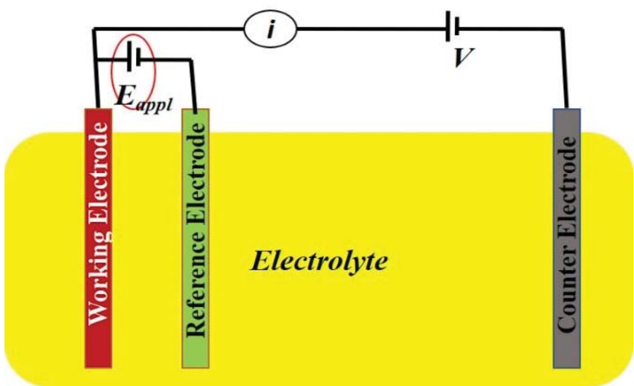

Figure 5.4 Three electrode system for electrochemical measurement.

5.1.5.1. Cyclic voltammetry

The CV measurements are carried out for all the electrodes (CP-5,10,15&20) along with CP at a scan rate of 500 mV/s with a potential window of 0.5 V. The results are shown in Fig. 5.5 (a).

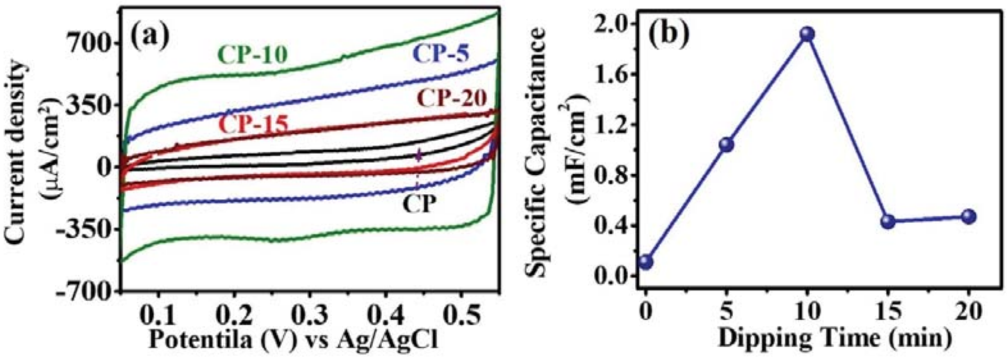

Figure 5.5 (a) CV and (b) specific capacitance for varied dipping time for all the electrodes.

For all the samples, the areal capacitance was calculated using the following formula [13, 14]:

$$C = \frac{(\int IdV)}{s \times A \times V} \qquad 5.1$$

Where I is the current (A), s is scan rate (mV/s), V is the potential window (V), and A is the active area (1 cm^2) of the electrode. The numerator of the right-hand side of Eqn. 5.1 stands for the area under the CV curve, as shown in Fig.5.5(a). The calculated areal capacitances are depicted with respect to dipping times in Fig.5.5(b). Pristine carbon paper possesses an areal capacitance of value 0.11 mF/cm^2. The increased capacitance value is observed for all SnO_2 loaded samples compared to the CP. However, the highest capacitance value of 1.92 mF/cm^2 is recorded for the C-10 sample, which is seventeen times more than that of the CP. This result indicates that a 10 min dip is an optimum time for loading the uniform SnO_2 on the CP. The excess load at 20 min possibly leads to large particulate depositions and reduces an effective surface for electrochemical interaction with electrolytes to result in a low capacitance value.

5.1.5.2. Charging discharging

Charging-discharging (CD) measurement is carried out for all the samples at a current density of 0.1 mA/cm^{2,} and the obtained results are shown in Fig.5.6.

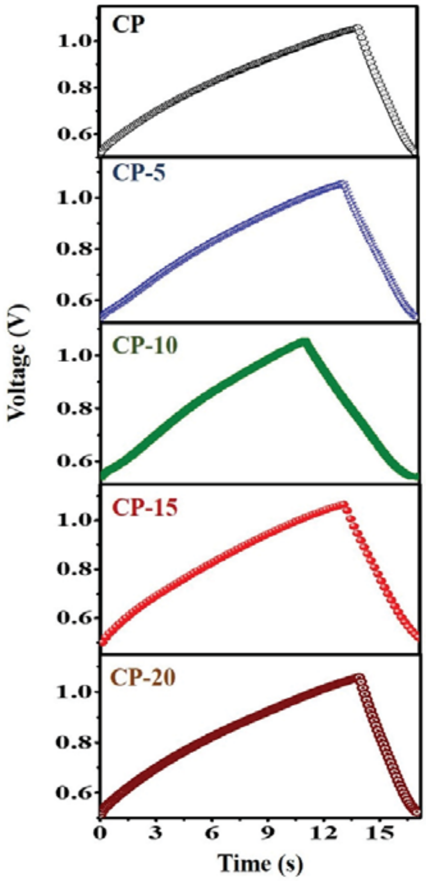

Figure 5.6 Charging discharging plots for CP and SnO_2 decorated CP.

Areal capacitance (C) is also calculated from the charging discharging curve using the following relation [13, 14]:

$$\boldsymbol{C = \frac{I \times tc}{A \times \Delta V}} \qquad \textbf{5.2}$$

Here, I is the current density (0.1mA/cm^2), tc is discharging time, A is the active area (1 cm^2), and ΔV is the potential window. The calculated value is depicted in Fig. 5.7(a). It is clear from the figure that the capacitance value obtained from charging-discharging measurement follows a similar trend for values obtained from CV measurements of Fig 5.5(b). Importantly, CD analysis also shows the highest specific capacitance for CP-10.

Further retention of capacitance is tested by running a thousand cycles of CD with a current density of 0.1 mA/cm^2 for the C-10. High retention of capacitance up to 98% is obtained [Fig.5.7(b)], and it indicates the strong stability of SnO_2 QDs in the carbon matrix.

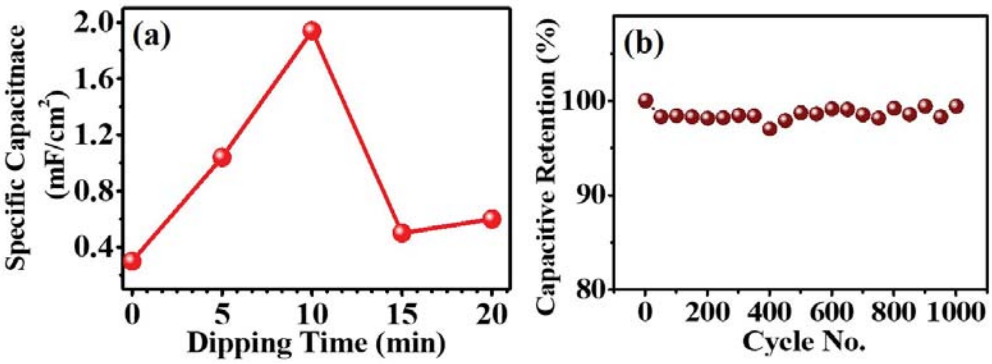

Figure 5.7 (a) Specific capacitance with respect to dipping time calculated from charging-discharging plot (b) Cyclic stability of CP-10.

5.1.5.3. Electrochemical impedance spectroscopy study

High capacitance value for the CP-SnO_2 may arise from both EDLC and pseudo-capacitance. Further elucidation of electrochemical capacitance is carried out using EIS measurements for a frequency range of 0.01 Hz to 10^5 Hz with an *ac* excitation voltage of 10 mV. Nyquist plot obtained for CP [Fig.5.8 (a)] and CP-10 [Fig.5.8 (b)] show two semicircles [Fig.5.8]. The semicircles in high-frequency and in low-frequency regions represent kinetic and diffusion-controlled phenomena, respectively. The whole Nyquist plot can be simulated as an outcome of the two parallel circuits. Each parallel circuit contains resistance and capacitance. The high-frequency part is represented with charge transfer resistance (R_{ct}) and capacitance phase element (CPE) [Fig.5.8(b) & (c) inset]. The deduced values from the simulation are given in Table. 5.1. The extremely low value of R_{ct} of C-10 refers to a pseudo-capacitive contribution from the SnO_2 QDs. Impedance equivalent to CPE is defined as $Z_{CPE}=Z_o(j\omega)^{-n}$, $0 \leq n \leq 1$. Where two extreme limits, 0 and 1, refer to the pristine form of resistance and capacitance, respectively. Thus, the value of *n* approaching 1 indicates a strong contribution of capacitance [15]. The low-frequency part represents a parallel combination of leakage resistance (R_1) and double-layer capacitance (C_{dl}) [Fig 5.8 (b) & (c) inset]. The simulated C_{dl} is slightly high for the CP compared to the CP-10, and it indicates a decoration by SnO_2 QDs prohibiting the EDLC contribution.

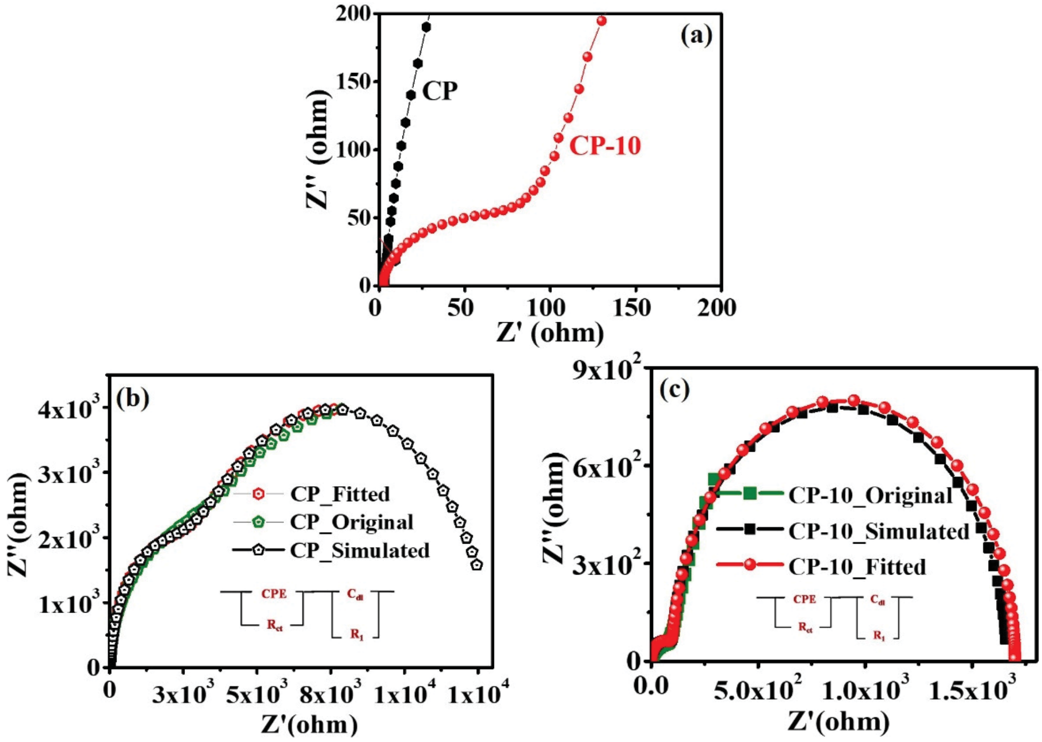

Figure 5.8 (a) Nyquist plot for CP and CP-10, Fitted Nyquist plots for (b) CP, and (c) C-10 with equivalent circuits.

Table 5.1 Fitting parameters from EIS measurements for CP and CP-10.

Name	C_{dl}(mF)	R_1(ohm)	R_{ct}(ohm)	CPE (nF)	n_1
CP	0.2	2214	11093	0.8	0.773
CP-10	0.05	100	1559	0.5	1

The above study demonstrates the utility of CP as EDLC and defects induced conductivity of SnO2 to achieve an enhanced electrochemical behavior. In the experiment, dipping time plays a decisive role. Obviously, after a certain time, the surfaces provided by CP is not sufficient to accommodate more amount of SnO_2 NPs and thus restricts further improvement in capacitance value. Graphene, like GO with a very high surface area along with layer structure, can be a potential choice to improve capacitance value. However, it may have associated issues, as discussed below.

5.2. Electrochemical application of GO-SnO_2 composite

The efficacy of defects laden SnO_2 as an electrochemical component for pseudo-capacitance is found in the above discussion. For further usefulness, it is investigated with GO, which has a skeletal structure of graphene with a very high surface area and layered structure. It is chosen as an EDLC candidate to make GO-SnO_2 composite. Two types of GO-SnO_2 (in-situ) and GO-SnO_2 (ex-situ) are prepared. The details of synthesis and characterization are described in Chapter-2. The ex-situ sample contains a functional group (epoxy, hydroxyl, and carbonyl) of GO along with SnO_2 NPs of 2.4 nm. However, the in-situ composite has bigger NPs than the as-prepared NPs with a certain reduction in functional groups in GO. The presence of functional groups in GO and the variation in size of NPs can influence electrochemical properties. Hence, the electrochemical studies with both in-situ and ex-situ samples are carried out.

5.2.1. Electrode preparation

The working electrodes are prepared by mixing active materials [pristine SnO_2 QDs /GO-SnO_2 (in-situ)/GO-SnO_2 (ex-situ) samples] and polyvinylidene fluoride (PVDF) in a mass ratio of 80:20 in N-methyl-2-pyrrolidone (NMP) solution. The resulted thick slurry is used for coating on conductive carbon paper. It is dried at 60 ^oC overnight in a vacuum oven. The loading mass of the active material is calculated to be ~ 5 mg/cm^2 for each of the electrodes.

Electrochemical measurements are done in three electrodes configuration using Metrohm-Autolab model PGSTAT302N. Carbon paper coated with active materials, platinum electrode, and Ag/AgCl is used as the working electrode, the counter electrode, and the reference electrode, respectively, in 1M H_2SO_4 electrolyte. A scheme of electrode configuration is given in Fig.5.4.

5.2.2. Cyclic voltammetry

For a comparative study, CV curves obtained for all three samples, in-situ, ex-situ, and as-prepared SnO_2 QDs at 50 mV/s are shown in Fig. 5.9. The electrode with QDs demonstrates the lowest current density. The ex-situ sample shows a current density of 2 A/g against only 0.6 A/g for the in-situ sample at a scan rate of 50 mV/s.

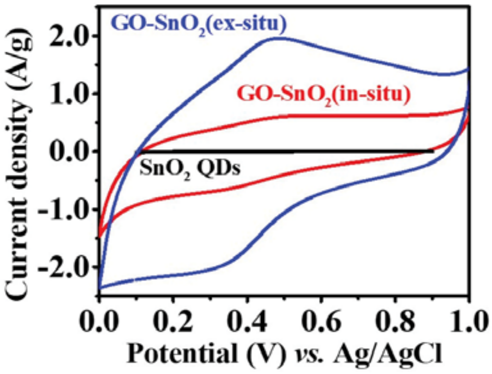

Figure 5.9 CV of in-situ, ex-situ, and as-prepared SnO_2 QDs at a scan rate of 50 mV/s.

The CV performance of GO-SnO_2 at different scan rates (10-50 mV/s) for a potential window of 1 V is evaluated and depicted in Fig.5.10.

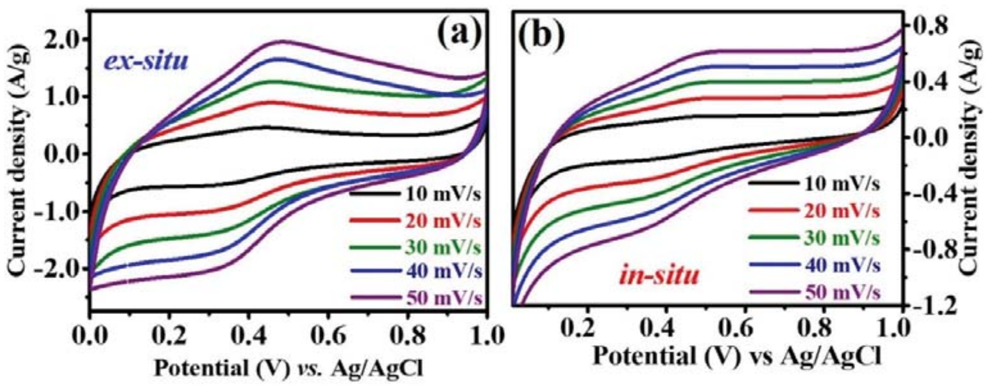

Figure 5.10 Cyclic voltammetry study of GO-SnO_2 (a) ex-situ and (b) in-situ at various scan rates.

As seen from Fig.5.10 (a) and (b), both ex-situ and in-situ samples have nearly rectangular CV curves. However, the ex-situ sample exhibits additional features, oxidation, and reduction peaks at 0.43 and 0.36 V, respectively, at a scan rate of 10 mV/s [Fig. 5(a)]. Gradually they shift to 0.47 and 0.31V at 50 mV/s, respectively. Such behavior was observed earlier and was correlated to a transition between quinine/hydroquinone groups in carbonaceous material [16, 17], and it is noticeable due to the presence of abundant hydroxyl groups in carbonaceous materials. Thus, the observed transition indicates the availability of similar functional groups in GO for the ex-situ sample. On the other hand, a drastic decrease of such peaks in the in-situ sample points less availability, possibly due to the participation of functional groups during the growth GO-SnO_2 composite. Subsequently, it reduces the GO structure of the composite sample. This observation is in line with the evidence described in Chapter 2, Fig. 2.23, and 2.25 using the Raman and FTIR spectroscopic measurements, respectively.

The increment of cathode current to the potential value of the in-situ sample is found to be sluggish at a higher scan rate [Fig 5.10(b)]. Low current and sluggishness generally occur due to the poor charge transport in low conducting samples[16]. Notably, the ex-situ sample with QDs SnO_2 is markedly different from the in-situ sample with the bigger SnO_2 crystalline particles. This difference is an important aspect as the abundant surface defects, mainly rich with the V_P in QDs[12], contribute to the improved conductivity by creating donor levels close to the conduction band. Moreover, the conductivity is found to decrease for the bigger particle size, and thus a poor conductivity might occur in the in-situ samples, which has bigger crystals in the GO matrix. Such inference is supported further from the EIS study, as discussed later part in the chapter.

For quantitative analysis, specific capacitances are calculated using the following formula [7]:

$$C = \frac{(\int IdV)}{s \times m \times V} \quad 5.3$$

Where I is the current (A), s is scan rate (mVs^{-1}), V is the potential window (V), and m is the active mass of electrode (g). Specific capacitances for both GO-SnO_2 calculated for various scan rates are shown in Fig.5.11.

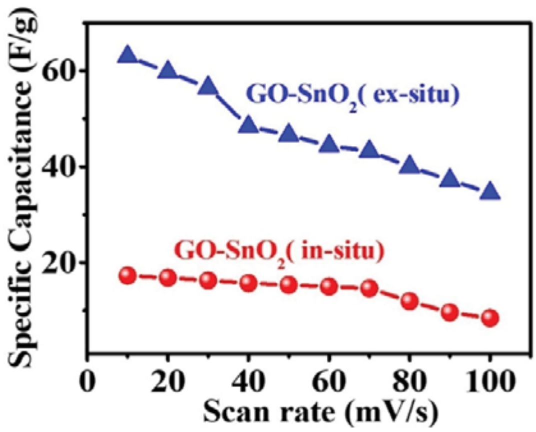

Figure 5.11 The specific capacitance of GO-SnO_2 composites at various scan rates.

Both GO-SnO_2 samples have shown higher specific capacitance values than the as-prepared SnO_2 NPs. EDLC and pseudo-capacitance arising from the oxidation and reduction of the active material contribute to the total capacitance value [18, 19]. The enhanced EDLC contribution can result from the presence of an increased surface area due to GO. Further, the GO layers can enhance the effective area by intercalation of NPs, which help to prohibit the multi-stacking of GO layers. Thus, significant improvement in the capacitance value compared to the pristine NPs is observed.

5.2.3. Charging discharging

Galvanostatic charging-discharging (CD) measurements for GO-SnO_2 samples are also carried out for various current densities ranging from 0.5 to 1.5 A/g and are shown in Fig.5.12. Fig. 5.12(a) depicts the CD of the ex-situ sample for various current densities. The ex-situ sample possesses a non-linear response during discharge with a plateau in the potential region of 0.4-0.6 V. Such plateau is not prominent in the in-situ sample shown in

Fig.5.12 (b). The origin of it is ascribed to the oxidation-reduction[16, 17] peaks of the functional groups present in the ex-situ sample, and it is in line with the CV results [Fig. 5.10(a)].

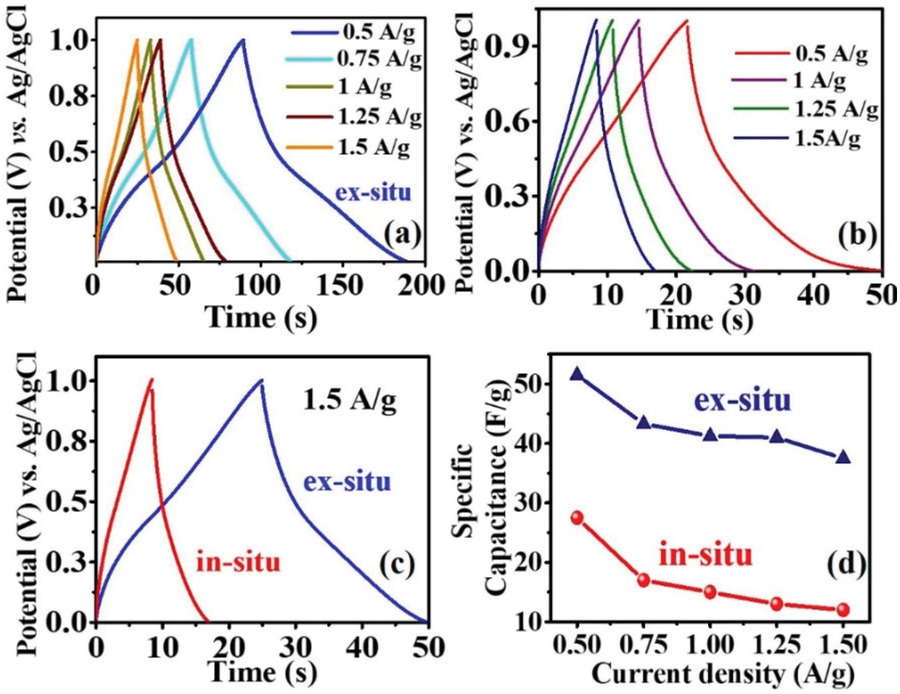

Figure 5.12 Charging discharging of GO-SnO_2 (a) ex-situ (b) in-situ at different current densities; (c) CD of the in-situ and the ex-situ samples at a current density of 1.5 Ag^{-1} (d) specific capacitance vs. current density.

CDs of both samples at a current density of 1.5 A/g are depicted in Fig.5.12(c) for the comparative evaluation. A reduced discharging time (t_d) is observed for the in-situ sample [Fig.5.12(c)]. The specific capacitance is dependent proportionately to t_d value, as seen in Eqn.5.4. The obtained specific capacitances using the relation in Eqn. 5.4 are depicted in Fig.5.12(d)[7].

$$C_s = \frac{I \times t_d}{m \times \Delta V} \quad \textbf{5.4}$$

Here, I current density, t_d discharging time, m is the active mass, and ΔV is the potential window. Clearly, a lower capacitance value is obtained for the in-situ sample than the ex-situ sample, and this result matches well with the CV measurements (Fig. 5.11).

To verify the capacitance retention of both in-situ and ex-situ samples, CD is carried out for the 1000 cycles with a current density of 0.5 A/g and is displayed in Fig.5.13. The ex-situ and in-situ samples show retention of 99% and 88%, respectively. In fact, an earlier study has pointed out that QDs are electrochemically stable [20], while the bigger SnO_2 particle suffers from the volume change during the electrochemical process. Thus, the better retention of the ex-situ is assigned to the stability of particles.

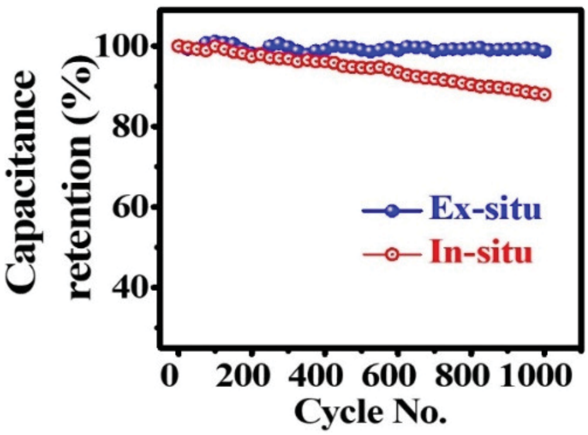

Figure 5.13 Retention of the capacitance of GO-SnO_2 composites.

5.2.4. Electrochemical impedance spectroscopy study

For further understanding, the effect of small and bigger particles as decorated in the ex-situ and the in-situ samples, respectively electrochemical impedance spectroscopy (EIS) measurements are carried out in a frequency range from 10^{-2} to 10^{5} Hz with an AC excitation voltage of 10 mV and the results are depicted in the Fig.5.14. For both the samples, two in-complete semicircles are obtained. However, a smaller radius is observed for the ex-situ sample than that for the in-situ sample. This feature conveys-a better conductivity of the smaller particle[21]. Smaller particle leads to better conductivity, and its implication enhanced dielectric value is reported in reference 9[9]. Thus, improved conductivity and stability by QDs are important aspects for GO-SnO_2 composites to provide superior electrochemical performance.

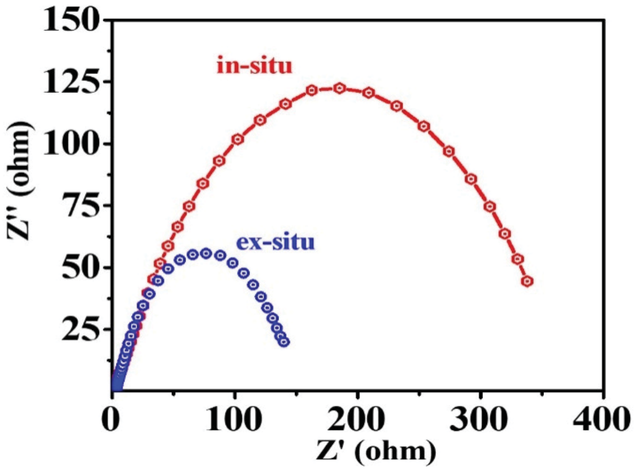

Figure 5.14 Impedance spectra for GO-SnO_2 composite.

Furthermore, the presence of functional groups in GO is also a crucial factor as they influence electrochemical performance. In the above description, the distribution of functional groups varied based on the synthesis techniques (in-situ or ex-situ), and a clear deviation in the electrochemical performance is elaborated.

5.3. Photocatalysis Application of SnO_2 and GO-SnO_2 Composite

For viable photocatalytic activity, nanostructured metal oxides like TiO_2, SnO_2, ZnO, V_2O_5, Fe_2O_3 are hugely investigated and utilized in the last two decades as frontier materials [22-24]. Among them, direct bandgap semiconductor, SnO_2 with easy processability, and non-toxic characteristics attract enormous attention[1]. Additionally, lowering the dimension from the bulk phase to the quantum confinement domain yields distinct properties along with a tremendous increase in specific surfaces. Besides, inherent O_V in SnO_2 NPs modulating the electronic band structure present it as a frontline candidate for photocatalysis. SnO_2 is a wide bandgap material, can be utilized under UV irradiation as a photocatalyst. In the current chapter, the efficacy of SnO_2 is elaborated under UV light. However, UV contribution in the natural solar spectrum reaching to the surface of the earth is limited to ~ 4% only. Thus, harvesting a large part of the visible sunlight would be a target for an organic pollutant for photocatalytic degradation. To overcome the limited utility of wide bandgap SnO_2, composite with GO is proposed. It provides large surfaces, induces hydrophilicity, and has the potential for suitable interfacial engineering with SnO_2 to hold the electron-hole recombination [25-28]. Moreover, SnO_2 QDs improves the conductivity of the system. In recent decades rGO is used in many cases for metal oxide composite; however, it lacks certain benefits of GO arising from functional groups.

5.3.1. Photocatalysis experiment

For the evaluation of the photocatalysis property of SnO_2 QDs, degradation of methylene blue (MB, 250 ppm) is investigated. A UV lamp of 2.21 mW/cm^2 (258nm, 9W, PL-S, PHILIPS, Poland) is utilized as a light source. A stock solution of the dye and catalyst (concentration of 0.05 mg/ml of SnO_2 QDs is made in the dark and is kept for desorption-adsorption equilibrium. Then it is exposed to the desired light source for different intervals of time. 4 ml of irradiated solution is analyzed using a UV-Visible (AVANTES) spectrometer. Degradation of MB is monitored by recording the absorption peak of MB at 664 nm. To test the photocatalysis behavior under the visible light, the UV-C light source is replaced by a white lamp (28.4 mW/cm^2, 11W, PL-S, PHILIPS, Poland) that covers a visible wavelength from 400 to 750 nm.

5.3.2. Photocatalysis under UV light irradiation

Photodegradation of MB dye under the UV light irradiation is studied using QDs as a catalyst. The characteristic changes of the UV-Vis absorption spectra of MB dye during the process is collected and shown in the Fig.5.15.

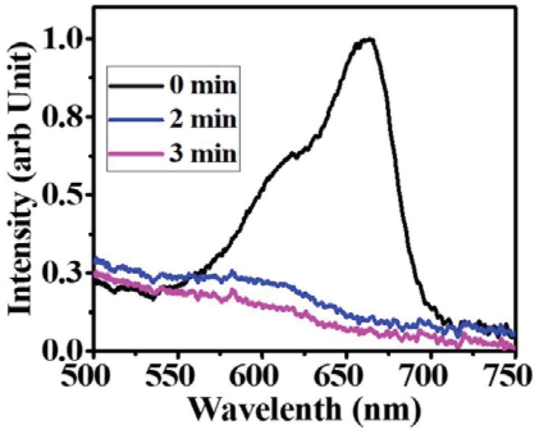

Figure 5.15 Time-dependent UV-Vis absorption spectra of MB with SnO_2 QDs under the UV irradiation.

The UV-Vis peaks between 600 to 700 nm, arising due to the hetero-poly aromatic linkage in MB dye is monitored as a reference point for the progression of dye degradation [29, 30]. The unique feature is that the corresponding MB dye peak around 664 degrades completely within < 3 minutes. Recent results on dye degradation under the UV light irradiation are enlisted in Table-1. Obviously, QDs SnO_2 shows the best performances among others for MB degradation under UV-light degradation.

Table 5.2 Comparison between degradation time of dyes in the presence of the different catalysts

S/N	Sample	Dye	Degradation time (min) (Degradation%)	Ref
1.	SnO_2	MB	120 (80%)	[31]
2.	V doped SnO_2	MB	120 (98%)	[31]
3.	SnO_2	MO	100 (52%)	[32]
4.	CdS-SnO_2	MO	100 (95.2%)	[32]
5.	SnO_2	MB	50 (90%)	[33]
6.	SnO_2 QDs	RhB	70 (99%)	[34]
7.	PEGME-SnO_2 QDs	RhB	40 (99%)	[34]
8.	SnO_2	MB	180 (73%)	[29]
9.	SnO_2	Rhodamine B	105 (99%)	[35]
10.	SnO_2	MB	600 (99%)	[36]
11.	Zn doped SnO_2	MB	80 (99%)	[36]
12.	SnO_2 QDs	MB	<3(99%)	**Present work**

5.3.3. Mechanism for dye degradation by SnO_2 QDs

Photocatalyst performance depends on the efficient routes of production of charge carriers and their availability for the generation of active radicals, in particular. To achieve a better performance, two basic criteria need to be fulfilled (1) close matching or tuning of the light source with the bandgap of catalyst and (2) delay in recombination process of photogenerated electron and hole (e-h), possibly by the presence of sufficient defect sites to trap it.

UV-Vis and PL spectroscopic measurements provide information on the bandgap and presence of defects in SnO_2 QDs respectively. Tauc's plot from UV-Visible absorption data is deduced and is shown in Fig. 5.16 (a). The detailed discussion of PL is corroborated in the earlier chapters Chapter-4.

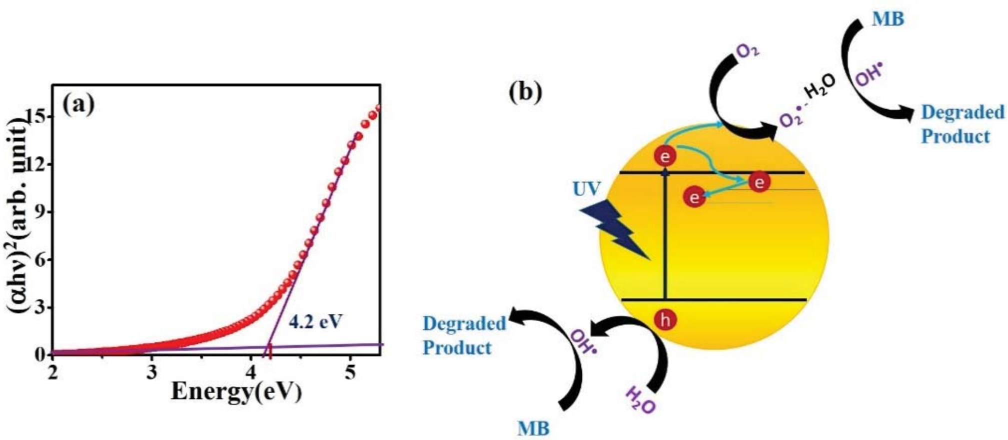

Figure 5.16 (a)UV-Vis spectrum of SnO_2 QDs (b) MB degradation in the presence of SnO_2 QDs with UV illumination.

From the Tauc's plot shown in Fig.5.16 (a), the bandgap of QDs is found to be 4.2 eV, which is lesser than the exciting radiation (4.8 eV). Based on the results from PL and UV-Vis measurements, a schematic presentation of the photocatalysis effect is given in Fig. 5.16 (b). When a metal oxide photocatalyst is illuminated by the light with energy higher than a metal oxide bandgap, electron/hole pairs are generated. Some of these pairs can migrate to the surface, and the migrated electrons react with the dissolved O_2 to make superoxide radical[37]. On the other hand, the hole reacts with water to produce hydroxyl radicals. Both these radicals are highly reactive and break the dye down. Through this process, the degradation is accomplished. However, after the formation of the electron-hole pair after the UV-light irradiation, there is a high probability of the recombination, and it leads to a decreased availability of electron and hole for the catalytic performance. However, due to the creation of energy states closer to CBM as revealed in earlier PL studies, the photo-generated electrons can get trapped in defects and prolong the recombination process. Thus, increasing the lifetime of electrons makes them available for catalytic action.

Importantly, due to limitations as manifested by a wide bandgap in the photocatalyst performance, dye degradation under a visible light remains elusive. Thus, to achieve the degradation under the visible light irradiation with QDs as a catalyst, the addition of GO is attempted. It is worth noticing that GO enjoys structural similarity with the graphene structure and possesses both π-conjugated sp^2 domains and sp^3 character along with oxygenated functional groups, present both in basal and edge through covalent type bonds with graphene carbon atoms[25]. Obviously, the presence of graphene-like characteristics in GO provides a high surface area [25, 38], and most importantly, it exhibits brilliant adsorption affinity to various dye [27, 28]. Thus, higher hydrophilicity than the graphene can lead to an improved dispersion and catalytic efficiency through close proximity by an adsorption mechanism [39]. Additionally, the functional groups of GO influence surface potential and hence the work function [40-42]. Indeed a higher work function was recorded for GO than the rGO using techniques like kelvin probe force microscopy (KPFM) or ultraviolet photoelectron spectroscopy(UPS) by various groups[43, 44]. The high work function creates a favorable strong band bending with a lower work function of semiconductor. In consequence, it leads to improved spatial charge separation in the GO matrix to enable increased performance for the semiconductor catalysis. The above decisive qualities make GO as one of the impeccable candidates for photocatalyst with SnO_2 QDs.

5.3.4. Photocatalysis under visible light irradiation

Photodegradation of MB dye under visible light irradiation is investigated, and characteristic changes of the UV-Vis absorption spectra of MB dye are collected in the presence of three different samples, namely SnO_2 QDs, GO-SnO_2, and GO. The comparative results obtained for the dye degradation are shown in Fig. 5.17(a), (b), and (c) for SnO_2 QDs, GO-SnO_2, respectively.

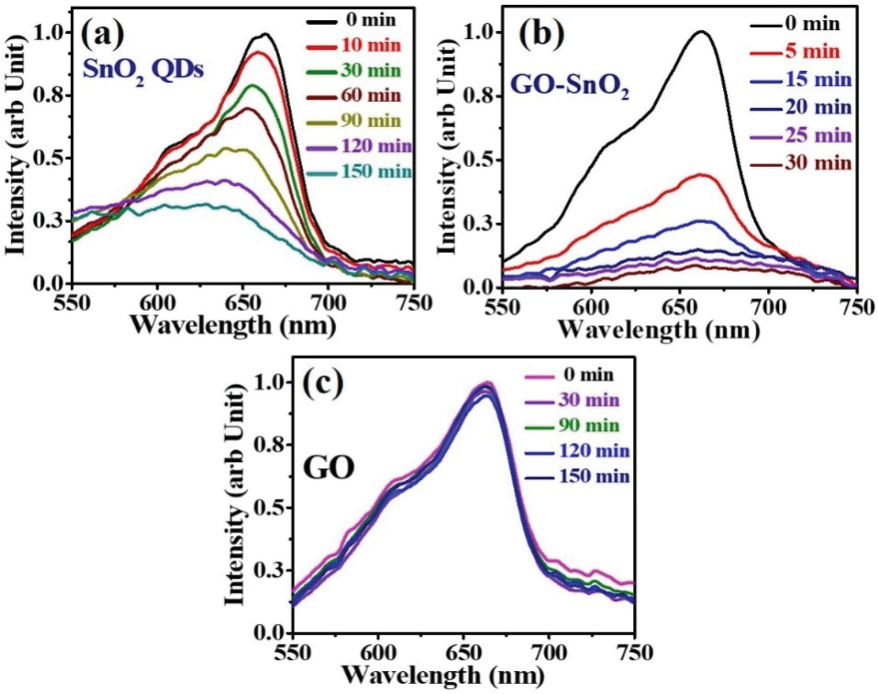

Figure 5.17 Time-dependent UV-Vis absorption spectra of MB in the presence of (a) SnO_2 QDs (b) GO-SnO_2 and (c) GO.

The peaks around 650, arising due to the hetero-poly aromatic linkage in MB dye is monitored as a reference point for the progression of dye degradation[37]. A nominal reduction is observed for the GO as a catalyst [Fig 5.17(c)]. SnO_2 QDs with a bandgap value ~4.2 eV degrades MB nearly by ~65% in about 150 min of visible light exposure [Fig.5.17(a)]. Comparatively, the composite of the above components, GO-SnO_2 QDs, does a brilliant job by near complete degradation of the dye (about 94% of MB) under the same light illumination. Most importantly, such degradation is achieved within 30 mins of light exposure [Fig.5.17(b)].

The degree of photocatalytic MB degradation as a function of time (C_t/C_0: C_0 and C_t are the initial and concentration at the time (t) is calculated for each catalyst with a considerate note of the maximum absorbance peak of MB at 664 nm. The MB degradation results are shown in Fig. 5.18(a). The quickest degradation is obvious for the nanocomposite. For further insight into the reaction kinetics for different catalysts, Fig. 5.18(b) depicts plot -ln (C_t/C) *vs.* t [45]. The linear plot for all catalysts supports pseudo-first-order kinetics for dye degradation. The rate of the reaction is then calculated by fitting the plot with the equation $\ln C_t = -kt + \ln C_0$. The rate constants '*k*' thus obtained for different catalysts such as GO, SnO_2 QDs, and GO-SnO_2 are 0.0003, 0.007, and 0.08 min^{-1}, respectively. The highest value for the GO-SnO_2 nanocomposite indicates its highest efficiency of dye degradation, among others.

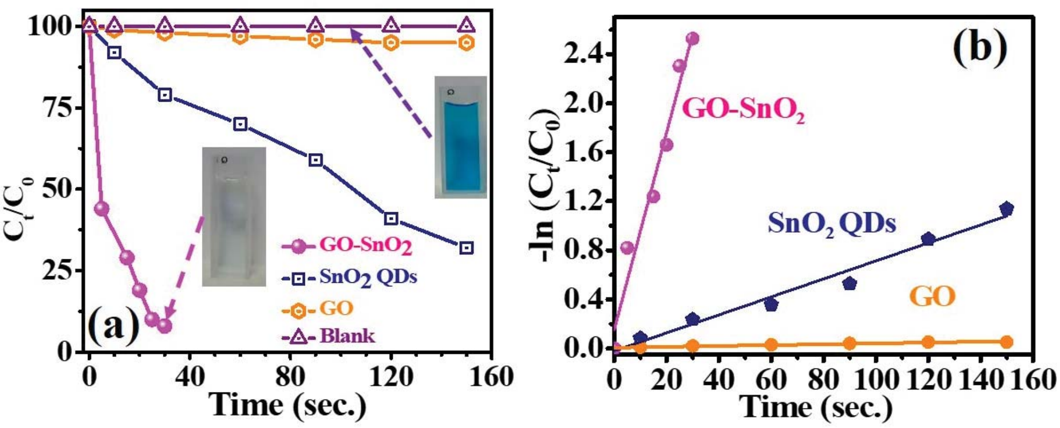

Figure 5.18 (a) C_t/C_0 vs. *irradiation time for photo-degradation of MB while the inset shows color of MB before (top) and after (bottom) degradation and (b) photocatalytic reaction kinetics.*

5.3.5. Mechanism for visible-light-driven photocatalysis

In the current scenario, the visible light excitation with less energy than the bandgap energy of QDs (4.2 eV) is not sufficient to excite an electron from the valence band (VB) to the conduction band (CB) of SnO_2. Hence the traditional mechanism of photo-generation of electron-hole pairs, from the VB to the CB, cannot hold as a process with the UV-irradiation. Hence an intermediate energy route operates for dye decay. A possible mechanism for the degradation of MB under the visible light irradiation is shown in Fig.5.19. The following diagram demonstrates the energy position of the dye and the catalyst based on the respective work functions ($q\Phi$) [$q\Phi_{MB}$ (-5.67 eV), excited MB_$q\Phi_{MB*}$ (-3.81 eV), $q\Phi_{GO}$ (-5 eV), $q\Phi_{SnO2}$ (-4.55 eV)][42, 44]. It is noteworthy that the work function is shown against the reference of GO. Moreover, the work function of GO is found to be always higher than rGO, and the transfer of an electron from SnO_2 to GO is thus possible[42, 43].

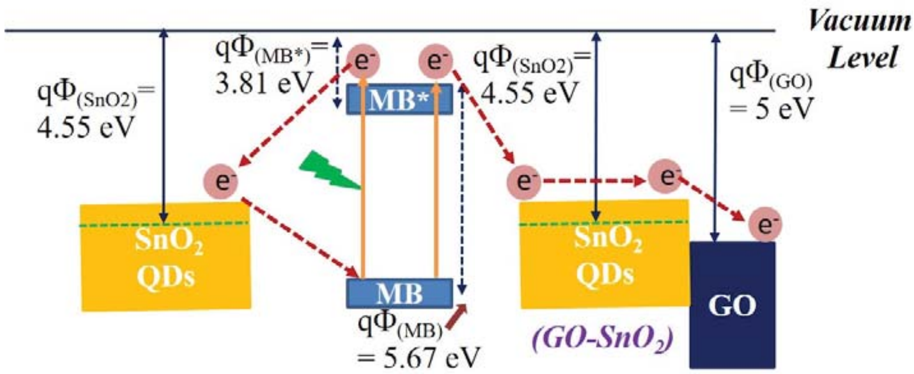

Figure 5.19 Energy diagram showing possible electron transfer mechanism from MB to SnO_2 and GO-SnO_2.

Comprehending the redox potential of MB (1.86 eV), MB is easily excited to MB* under the visible light irradiation[46]. However, in the presence of QDs, this electron from the excited state (MB*) is transferred favorably to the CB of the metal oxide, leaving behind a hole in MB (Fig.5.19). These separated electrons and holes can be trapped by the dissolved O_2 in the MB solution and form reactive oxygen species ($O^{\bullet-}$) and hydroxyl radical ($OH^{\bullet}$), which are responsible for the dye degradation. However, a slow decomposition is observed only for SnO_2 QDs. This is due to a lack of spatial separation of photogenerated electrons and holes. Similarly, a feeble response is observed for only GO. Noteworthy, the poor conductivity of GO can restrict the migration of charge carriers inside the GO from MB* and subsequently prohibits the formation of active radicals to initiate the dye degradation. The excellent performance is observed for the composite sample, and it becomes possible because of the strong adsorption of dye molecules with GO. The giant π-conjugated plane present in graphene-like GO might adsorb the dye strongly via π-π stacking with face to face orientation [28]. Besides, the strong electrostatic attraction in the aqueous medium is also possible between a positively charged MB and negatively charged functional groups present in GO. A schematic is given in Fig. 5.20 to describe this kind of interaction:

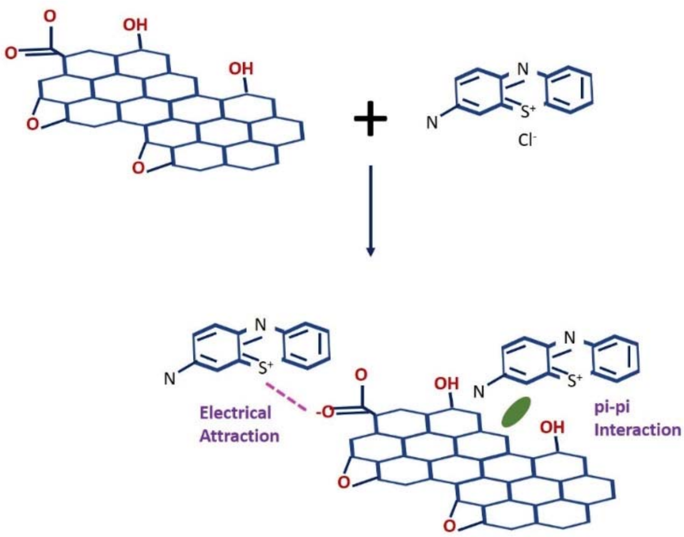

Figure 5.20 Schematic illustration for the adsorption mechanism of MB on the GO surface.

This leads to the availability of MB in the close proximity of QDs in GO-SnO_2 composite. Followed by such adsorption, the photocatalysis process begins with the absorption of visible light by the dye to result in an excited state of MB (MB*) with an electron. In the next process, the electron is transferred from the excited MB to the CB of SnO_2 because of the relatively low value of the work function of the metal oxide (Fig.5.19). Subsequently, the electron is transferred from QDs to GO owing to the work function difference. This leads to a spatially separated electron and hole. Such an arrangement delays the recombination procedure and enables availability for the degradation process. The possible reaction pathways during the photocatalytic degradation process of MB by the GO-SnO_2 composite are as follows:

$MB + h\nu \rightarrow MB^* + e^-$ (e- passes to GO through SnO_2)

$e^-_{(GO)} + O_2 \rightarrow O_2^{\bullet -}$ (formation of superoxide radical)

$O_2^{\bullet -} + H_2O \rightarrow HO_2^{\bullet} + OH^-$

$HO_2\bullet + H_2O \rightarrow HO^{\bullet} + H_2O_2$ (formation of hyoxide-oxide radical)

$H_2O_2 \rightarrow 2HO^{\bullet}$

$OH^{\bullet} + MB \rightarrow$ Degradation product

To verify the charge transfer from the SnO_2 to GO, PL spectra are taken from both SnO_2 and GO-SnO_2. The results are depicted in Fig.5.21(a). A broad peak is observed for both samples at 2.1 eV with a very strong intensity for QDs. This enhanced intensity arises due to the abundance of O_V present in the SnO_2. However, the PL intensity is reduced drastically in the case of the GO-SnO_2 [Fig. 5.21(a)]. This reduction in intensity is an indication of a photo-excited electron transfer from the SnO_2 QDs to the GO matrix [Fig. 5.21(a)inset], and subsequent prevention of the recombination of electron and hole to lead to a photoluminescence effect. Efficient charge transfer takes place in the GO-SnO_2 composite to make it an efficient catalyst compared to only the QDs. Thus, heterostructure formation with favorable engineering of interfacial properties between QDs and GO provides the most efficient performance. This understanding has a unique significance to utilize the GO, a poor conductor, as an efficient photocatalyst under visible light irradiation.

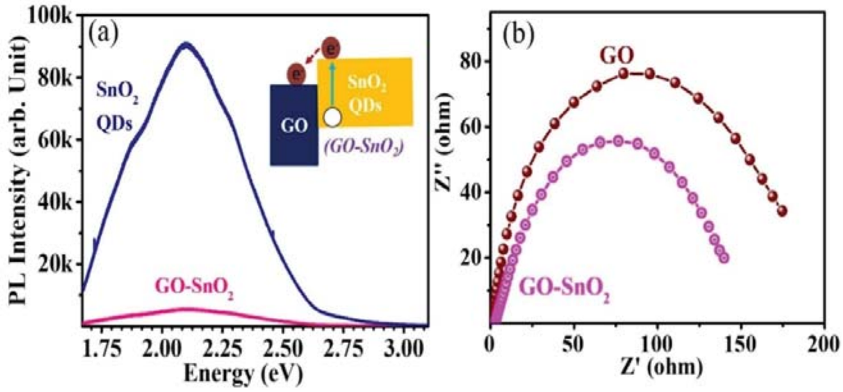

Figure 5.21 (a)PL spectra of SnO_2 QDs and GO-SnO_2 with an inset to show an electron transfer from QDs to GO (b) EIS spectra of GO and GO-SnO_2 composite.

Improved dispersion of GO-SnO_2 over SnO_2 QDs can take place because of the functional groups in GO. Moreover, the stacking of SnO_2 on the GO surfaces improves immobilization of the NPs, which enhances the conductivity of the composite altogether. Improvement in conductivity is investigated by EIS measurements, and results are shown in Fig. 5.21(b). A relatively small radius is obvious for the composite, as seen from the Nyquist plots of GO and GO-SnO_2 nanocomposite. The feature indicates a decrease in the solid-state interface layer resistance of GO after the addition of QDs into the GO matrix, which helps better charge transport by lowering the resistance at the surface[47, 48]. Thus, the interface between GO and SnO_2 becomes a novel feature to corroborate sufficient charge transfer through tailoring the defects chemistry of QDs and functional graphene, GO.

In summary, the combined effects and improved conductivity provided by SnO_2 QDs and benefits of the functional group present in the GO for modulation of work function and dye adsorption synergistically enhance the photocatalytic process to show an excellent performance for the dye degradation.

5.4. Summary

1. The role of SnO_2 QDs for supercapacitor application is elaborated. Improved conductivity, because of the presence of $V_{P,}$ is described as a reason behind the excellent supercapacitor behavior. For that purpose, SnO_2 QDs decorated CP are

examined. Further, to improve the loading of metal oxide in the electrode, GO is utilized. A very high surface area of GO is found as a proper choice to make a composite with SnO_2 for electrochemical applications. Apart from the EDLC nature of GO, the presence of a functional group is exploited as pseudo-capacitance, and the result is compared with another composite of GO-SnO_2 (in-situ), which has less amount of active functional groups. Interestingly the conductivity issue of the unreduced GO due to the presence of functional group is countered back by the presence of better conductive SnO_2 QDs.

2. In the photocatalysis study, the critical role of defect is projected for the excellent UV-light drove photocatalysis of MB using the SnO_2 QDs. The accomplishment of the degradation process within three minutes is one of the best results until now. Further, to explore the utility of this metal oxide for visible-light-driven catalysis, GO is incorporated to obtain proper interfacial engineering. This composite shows a brilliant performance of 94% degradation of MB within just 30 min. Observation of such outstanding results is possible because of efficient charge transfer from SnO_2 to GO which is proved by PL and EIS spectroscopy.

5.5. References

[1] B.K. Sahu, A. Das, Significance of oxygen defects in SnO_2 quantum dots as hybrid electrochemical capacitors, Journal of Physics and Chemistry of Solids, (2019).
[2] S. Das, V. Jayaraman, SnO_2: a comprehensive review on structures and gas sensors, Progress in Materials Science, 66 (2014) 112-255.
[3] S. Kucheyev, T. Baumann, P. Sterne, Y. Wang, T. Van Buuren, A. Hamza, L. Terminello, T. Willey, Surface electronic states in three-dimensional SnO_2 nanostructures, Physical Review B, 72 (2005) 035404.
[4] B.K. Sahu, A. Das, A.K. Prasad, G. Mangamma, The Role of In-Plane Oxygen Vacancy Defects in SnO_2 Nanoparticles for CH_4 Sensing, Journal of nanoscience and nanotechnology, 19 (2019) 7764-7770.
[5] A. Dieguez, A. Romano-Rodrıguez, A. Vila, J. Morante, The complete Raman spectrum of nanometric SnO_2 particles, Journal of Applied Physics, 90 (2001) 1550-1557.
[6] L.P. Ravaro, L.V. Scalvi, A.S. Tabata, F.M. Pontes, J.B. Oliveira, Nanoparticle characterization of Er-doped SnO_2 pellets obtained with different pH of colloidal suspension, Journal of Applied Physics, 114 (2013) 084304.
[7] S. Ghosh, G. Sahoo, S. Polaki, N.G. Krishna, M. Kamruddin, T. Mathews, Enhanced supercapacitance of activated vertical graphene nanosheets in hybrid electrolyte, Journal of Applied Physics, 122 (2017) 214902.

[8] A.C. Ferrari, D.M. Basko, Raman spectroscopy as a versatile tool for studying the properties of graphene, Nature nanotechnology, 8 (2013) 235.
[9] B.K. Sahu, A. Das, Significance of in-plane oxygen vacancy rich non-stoichiometric layer towards unusual high dielectric constant in nano-structured SnO_2, Physica E: Low-dimensional Systems and Nanostructures, (2018).
[10] M. Epifani, J.D. Prades, E. Comini, E. Pellicer, M. Avella, P. Siciliano, G. Faglia, A. Cirera, R. Scotti, F. Morazzoni, The role of surface oxygen vacancies in the NO_2 sensing properties of SnO_2 nanocrystals, The Journal of Physical Chemistry C, 112 (2008) 19540-19546.
[11] V. Bonu, A. Das, A.K. Prasad, N.G. Krishna, S. Dhara, A. Tyagi, Influence of in-plane and bridging oxygen vacancies of SnO_2 nanostructures on CH_4 sensing at low operating temperatures, Applied Physics Letters, 105 (2014) 243102.
[12] B.K. Sahu, G. Kaur, A. Das, Revealing interplay of defects in SnO_2 quantum dots for blue luminescence and selective trace ammonia detection at room temperature, ACS Applied Materials & Interfaces, (2020).
[13] Z. Yin, J. Xu, Y. Ge, Q. Jiang, Y. Zhang, Y. Yang, Y. Sun, S. Hou, Y. Zhang, Synthesis of V_2O_5 microspheres by spray pyrolysis as cathode material for supercapacitors, Materials Research Express, (2018).
[14] A. González, E. Goikolea, J.A. Barrena, R. Mysyk, Review on supercapacitors: technologies and materials, Renewable and Sustainable Energy Reviews, 58 (2016) 1189-1206.
[15] E.P. Randviir, C.E. Banks, Electrochemical impedance spectroscopy: an overview of bioanalytical applications, Analytical Methods, 5 (2013) 1098-1115.
[16] L. Lai, H. Yang, L. Wang, B.K. Teh, J. Zhong, H. Chou, L. Chen, W. Chen, Z. Shen, R.S. Ruoff, Preparation of supercapacitor electrodes through selection of graphene surface functionalities, ACS nano, 6 (2012) 5941-5951.
[17] Y. Yi, G. Weinberg, M. Prenzel, M. Greiner, S. Heumann, S. Becker, R. Schlögl, Electrochemical corrosion of a glassy carbon electrode, Catalysis Today, 295 (2017) 32-40.
[18] A.S. Arico, P. Bruce, B. Scrosati, J.-M. Tarascon, W. Van Schalkwijk, Nanostructured materials for advanced energy conversion and storage devices, Nature materials, 4 (2005) 366.
[19] C. Liu, F. Li, L.P. Ma, H.M. Cheng, Advanced materials for energy storage, Advanced materials, 22 (2010) E28-E62.
[20] V. Bonu, B. Gupta, S. Chandra, A. Das, S. Dhara, A. Tyagi, Electrochemical supercapacitor performance of SnO_2 quantum dots, Electrochimica Acta, 203 (2016) 230-237.
[21] B.K. Sahu, A. Das, Graphene oxide surface chemistry regulated growth of SnO_2 nanoparticles for electrochemical application, Journal of Alloys and Compounds, (2020) 154901.
[22] C.A. Martínez-Huitle, E. Brillas, Decontamination of wastewaters containing synthetic organic dyes by electrochemical methods: a general review, Applied Catalysis B: Environmental, 87 (2009) 105-145.
[23] S.P. Vattikuti, P.A.K. Reddy, J. Shim, C. Byon, Visible-Light-Driven Photocatalytic Activity of SnO_2–ZnO Quantum Dots Anchored on g-C_3N_4 Nanosheets for Photocatalytic Pollutant Degradation and H2 Production, ACS Omega, 3 (2018) 7587-7602.
[24] A.M. Al-Hamdi, U. Rinner, M. Sillanpää, Tin dioxide as a photocatalyst for water treatment: a review, Process Safety and Environmental Protection, 107 (2017) 190-205.
[25] S. Majumder, M. Sardar, B. Satpati, S. Kumar, S. Banerjee, Magnetization Enhancement of Fe_3O_4 by Attaching onto Graphene Oxide: An Interfacial Effect, The Journal of Physical Chemistry C, 122 (2018) 21356-21365.
[26] K. Zhao, L. Zhang, R. Xia, Y. Dong, W. Xu, C. Niu, L. He, M. Yan, L. Qu, L. Mai, SnO_2 Quantum Dots@ Graphene Oxide as a High-Rate and Long-Life Anode Material for Lithium-Ion Batteries, Small, 12 (2016) 588-594.
[27] S. Ma, S. Zhan, Y. Jia, Q. Zhou, Highly efficient antibacterial and Pb (II) removal effects of Ag-$CoFe_2O_4$-GO nanocomposite, ACS applied materials & interfaces, 7 (2015) 10576-10586.
[28] S. Song, Y. Ma, H. Shen, M. Zhang, Z. Zhang, Removal and recycling of ppm levels of methylene blue from an aqueous solution with graphene oxide, RSC Advances, 5 (2015) 27922-27932.
[29] S.P. Kim, M.Y. Choi, H.C. Choi, Photocatalytic activity of SnO_2 nanoparticles in methylene blue degradation, Materials Research Bulletin, 74 (2016) 85-89.

[30] S. Ghosh, K. Das, K. Chakrabarti, S.K. De, Effect of oleic acid ligand on photophysical, photoconductive and magnetic properties of monodisperse SnO_2 quantum dots, Dalton Trans, 42 (2013) 3434-3446.
[31] W.B. Soltan, M.S. Lassoued, S. Ammar, T. Toupance, Vanadium doped SnO_2 nanoparticles for photocatalytic degradation of methylene blue, Journal of Materials Science: Materials in Electronics, 28 (2017) 15826-15834.
[32] C.V. Reddy, R. Ravikumar, G. Srinivas, J. Shim, M. Cho, Structural, optical, and improved photocatalytic properties of CdS/SnO_2 hybrid photocatalyst nanostructure, Materials Science and Engineering: B, 221 (2017) 63-72.
[33] W. Zhao, W. Ma, C. Chen, J. Zhao, Z. Shuai, Efficient degradation of toxic organic pollutants with $Ni_2O_3/TiO_{2-x}B_x$ under visible irradiation, Journal of the American Chemical Society, 126 (2004) 4782-4783.
[34] S. Zhuang, X. Xu, Y. Pang, J. Hu, C. Yang, L. Tong, Y. Zhou, PEGME-bonded SnO_2 quantum dots for excellent photocatalytic activity, RSC advances, 3 (2013) 20422-20428.
[35] D. Venkatesh, S. Pavalamalar, K. Anbalagan, Selective photodegradation on dual dye system by recoverable Nano SnO_2 photocatalyst, Journal of Inorganic and Organometallic Polymers and Materials, 29 (2019) 939-953.
[36] L. Li, J. Liu, Y. Su, G. Li, X. Chen, X. Qiu, T. Yan, Surface doping for photocatalytic purposes: relations between particle size, surface modifications, and photoactivity of SnO_2: Zn^{2+} nanocrystals, Nanotechnology, 20 (2009) 155706.
[37] T. Kim, V.G. Parale, H.-N.-R. Jung, Y. Kim, Z. Driss, D. Driss, A. Bouabidi, S. Euchy, H.-H. Park, Facile synthesis of SnO_2 aerogel/reduced graphene oxide nanocomposites via in situ annealing for the photocatalytic degradation of methyl orange, Nanomaterials, 9 (2019) 358.
[38] Y. Hu, C. Xu, G. Xiao, M. Yi, Z. Chen, J. Zhang, Electrostatic self-assembly preparation of reduced graphene oxide-encapsulated alumina nanoparticles with enhanced mechanical properties of alumina nanocomposites, Journal of the European Ceramic Society, 38 (2018) 5122-5133.
[39] D. Li, M.B. Müller, S. Gilje, R.B. Kaner, G.G. Wallace, Processable aqueous dispersions of graphene nanosheets, Nature nanotechnology, 3 (2008) 101.
[40] L. Sygellou, G. Paterakis, C. Galiotis, D. Tasis, Work function tuning of reduced graphene oxide thin films, The Journal of Physical Chemistry C, 120 (2016) 281-290.
[41] P.V. Kumar, M. Bernardi, J.C. Grossman, The impact of functionalization on the stability, work function, and photoluminescence of reduced graphene oxide, ACS nano, 7 (2013) 1638-1645.
[42] X. Li, Y. Chen, A. Kumar, A. Mahmoud, J.A. Nychka, H.-J. Chung, Sponge-templated macroporous graphene network for piezoelectric ZnO nanogenerator, ACS applied materials & interfaces, 7 (2015) 20753-20760.
[43] B. Bhangare, N.S. Ramgir, S. Jagtap, A. Debnath, K. Muthe, C. Terashima, D.K. Aswal, S.W. Gosavi, A. Fujishima, XPS and Kelvin probe studies of SnO_2/RGO nanohybrids based NO_2 sensors, Applied Surface Science, 487 (2019) 918-929.
[44] S.-J. Choi, B.-H. Jang, S.-J. Lee, B.K. Min, A. Rothschild, I.-D. Kim, Selective detection of acetone and hydrogen sulfide for the diagnosis of diabetes and halitosis using SnO_2 nanofibers functionalized with reduced graphene oxide nanosheets, ACS applied materials & interfaces, 6 (2014) 2588-2597.
[45] A. Bhattacharjee, M. Ahmaruzzaman, A novel and green process for the production of tin oxide quantum dots and its application as a photocatalyst for the degradation of dyes from aqueous phase, Journal of colloid and interface science, 448 (2015) 130-139.
[46] H. Seema, K.C. Kemp, V. Chandra, K.S. Kim, Graphene–SnO_2 composites for highly efficient photocatalytic degradation of methylene blue under sunlight, Nanotechnology, 23 (2012) 355705.
[47] X. Liu, L. Pan, T. Chen, J. Li, K. Yu, Z. Sun, C. Sun, Visible light photocatalytic degradation of methylene blue by SnO_2 quantum dots prepared via microwave-assisted method, Catalysis Science & Technology, 3 (2013) 1805-1809.
[48] Y. Feng, N. Feng, Y. Wei, G. Zhang, An in situ gelatin-assisted hydrothermal synthesis of ZnO–reduced graphene oxide composites with enhanced photocatalytic performance under ultraviolet and visible light, RSC advances, 4 (2014) 7933-7943.

Abstract

With excellent success as a resistive-based sensing material, tin oxide (SnO_2) is well-studied among other metal oxides for the last four decades. However, with the recent progress in theoretical understanding and advancement in experimental amenities, SnO_2 is again in the limelight of research. Thanks to the presence of various defects present in this metal oxide like oxygen vacancies (O_V) includes in-plane oxygen vacancy (V_P) and bridging oxygen vacancy (V_B), which influences *n*-type conductivity in SnO_2 and make it a technically important material. However, clear demarcation of such defects in SnO_2 and their influences in various optical, electrical, and vibrational properties need further attention. Additionally, the inclusion of lower dimensions and improved understanding in the synthesis process opens up prominent areas of applications. Hence bringing two important factors, (i) synthesis and understanding the defect in lower dimension SnO_2 and (ii) utilizing these for various applications like resistive and optical-based gas sensing, supercapacitor, waveguide, photocatalysis motivates the current dissertation.

Primarily, a simple chemical route is followed to synthesis SnO_2 QDs, which are further used to obtain different sizes of nanoparticles (NPs) and defects distributions by annealing process in air atmospheres at various temperatures. For morphological and structural characterization of NPs, X-ray diffraction (XRD), transmission electron microscopy (TEM), and field emission secondary electron microscopy (FESEM) are carried out. Further, various spectroscopic investigations such as Raman, photoluminescence (PL), Fourier transfer infrared (FTIR), X-ray absorption spectroscopy (XAS), and electron energy loss spectroscopy (EELS) are carried to elaborate the presence of various defects in SnO_2 NPs and provide explanations for critical properties. Similar techniques are also employed for 1-D SnO_2 nanostructures (NSs) grown by chemical vapor deposition (CVD) by both gold assisted vapor-liquid-solid (VLS) and self-catalytic vapor-solid (VS) process. VLS

technique-grown 1-D NSs is found to hold a strong correlation with the growth temperature and the final shape of the NSs, which is also theoretically established by Gibb's free energy minimization process. Further, for the very first time, the critical role of the functional group of GO in controlling the shape of metal oxide during the growth process is demonstrated and well supported from TEM, FTIR, and Raman spectra.

The current thesis further discusses the impact of a strong plasmonic field on the vibrational properties of low dimensional SnO_2. Optimized SERS substrate obtained by using Ag nanonet enables the first-time observation of Raman allowed A_{1g} mode, which is otherwise hidden underneath defect induced D peak in SnO_2 QDs. Prior to that, the efficiency of this Ag nanonet is proven by single-molecule detection of rhodamine6G (R6G) molecule. Further, "Not mutual exclusion principle," rather the "strong plasmon from Ag nanonet resulted in gradient field Raman (GFR) induced enhancement in infrared (IR) peak" is proposed to be the reason behind the observation of IR allowed E_u(TO) mode during Raman spectra acquisition from 25 nm SnO_2 NPs. Though such GFR effect is profoundly discussed for organic molecules, rarely reported for inorganic molecules like SnO_2.

To overcome the various shortcoming of the resistive-based sensor, an alternative optical-based PL sensor using SnO_2 QDs is proposed. This quest for PL based sensing also helps to solve a long-standing problem regarding the presence of blue emission in the PL spectra for low-dimensional SnO_2 NPs. A rise of two obscured PL peaks in the blue emission region at 2.77, and 2.96 eV is observed in the presence of NH_3. Using this observation SnO_2 QDs detect up to 32 ppm of NH_3 very selectively even at room temperature. The critical role of cationic defects in selective ammonia detection is highlighted experimentally and theoretically. Additionally, PL induced waveguide characteristics of 1-D NSs are also demonstrated. Temperature-dependent PL, along with XAS experiments, is carried out for drawing a suitable band diagram for SnO_2 NSs.

Owing to the surplus surface to volume ratio, the presence of multiple oxidation states (Sn^{2+} and Sn^{4+}) SnO_2 QDs are utilized for electrochemical capacitance application. A gel mediated method is operated for the decoration of QDs on a carbon paper to be utilized as a working electrode. After a successful demonstration of the experiment, graphene oxide and SnO_2 (GO-SnO_2) composite is utilized as electrochemical capacitance by exploiting both electric double-layer capacitor (EDLC) form GO and pseudocapacitance from SnO_2. Along with this, the participation of a functional group of GO for pseudocapacitance adds extra value to the capacitance value. Similarly, for environmental remediation, UV-light driven catalysis study is inspected using SnO_2 NPs. A rapid degradation (< 3 min) of methylene blue by QDs is one the finest result till now using UV-light. While for utilizing the visible light for catalytical dye degradation, GO-SnO_2 composite is adopted. The purpose behind choosing such a composite is also explained, such as exploitation of the higher work function of GO to ensure proper electron transfer. Crucial role defects in improving conductivity are examined by electrochemical impedance spectroscopy (EIS).

Two different types of SnO_2 NPs with different defect distributions but with similar dimensions (~25 nm) are synthesized by annealing the as-prepared QDs in Air and Ar atmospheres. Detailed investigations using Raman spectroscopy and temperature-dependent photoluminescence (PL) measurements propose a strong presence of the in-plane oxygen vacancy in the Ar annealed SnO_2 sample. Despite the similarity in dimensions, Ar annealed sample shows ten times higher dielectric than the air annealed sample. Furthermore, the role of such defects is effectively utilized for near room temperature (50 ^{o}C) CH_4 sensors in a restive way. A detailed explanation for low-temperature performance is presented.